

DISS. ETH NO. 21817

# Dynamical evolution of young stellar clusters

A thesis submitted to attain the degree of  
DOCTOR OF SCIENCES of ETH ZURICH

(Dr. sc. ETH ZURICH)

Presented by

Michiel Cottaar

MSc, Utrecht University

born on 14.01.1987

citizen of the Netherlands

accepted on recommendation of

Prof. Dr. Michael R. Meyer, examiner

Prof. Dr. Mark Gieles, co-examiner

2014

Cover illustration:

Front cover – Image of the star-forming region R136 captured by the Wide Field Camera 3 on the Hubble Space Telescope.

Top on back cover – Image of the star-forming region IC 348 also captured by the Wide Field Camera 3 on the Hubble Space Telescope.

Bottom on back cover – Near-infrared JHKs image of the young, massive cluster Westerlund I. Figure taken from Brandner et al. (2008).



# Acknowledgments

I am thankful to all the great astrophysicists, I got to collaborate with, have scientific discussions with, and drink beers with. First of all I would like to thank my supervisor, Michael Meyer, for all his enthusiasm and for, despite always being busy, finding the time when it mattered the most (such as with the last-minute proofreading of this thesis). I also thank Kevin Covey, who kindly invited Michael and me to join as external collaborators in his and Jonathan Tan's IN-SYNC project and was always available for discussions on the data analysis pipeline and the science. Also a big thank you to Vincent Hénault-Brunet without whom I would never have attempted to analyze massive binaries, and whose hard work was more instrumental to our paper than the placement of second author suggests. Finally I would like to explicitly thank Richard Parker, Andrea Banzatti, Maddalena Reggiani, Justin Read, Sascha Quanz, Vincent Geers, Germano Sacco, and Rob Jeffries.

Of course I would also like to thank my family, especially my parents for always supporting me and patiently listening to the often convoluted explanations of my work. Hopefully this thesis can clarify things...

---

# Contents

<b>Acknowledgments</b>	<b>iii</b>
<b>Contents</b>	<b>v</b>
<b>List of Figures</b>	<b>xi</b>
<b>List of Tables</b>	<b>xiii</b>
<b>Abstract</b>	<b>xv</b>
<b>Kurzfassung</b>	<b>xvii</b>
<b>1 Introduction</b>	<b>1</b>
1.1 Star cluster formation and evolution . . . . .	3
1.1.1 Stars form in molecular clouds . . . . .	3
1.1.2 Early cluster evolution . . . . .	7
1.1.3 Long-term cluster evolution . . . . .	10
1.2 Tracers of dynamical evolution . . . . .	11
1.2.1 Mass segregation . . . . .	11
1.2.2 Spatial substructure . . . . .	12

## CONTENTS

---

1.2.3	Binary properties . . . . .	12
1.2.4	Virial equilibrium . . . . .	13
1.2.5	Collapse or expansion . . . . .	16
1.2.6	Cluster rotation . . . . .	16
<b>2</b>	<b>Correcting the radial velocity distribution for binary orbital motions</b>	<b>17</b>
2.1	Introduction . . . . .	18
2.2	Single-epoch radial velocities . . . . .	21
2.2.1	Method . . . . .	21
2.2.2	Solar-type binary properties . . . . .	25
2.2.3	Monte Carlo simulations . . . . .	26
2.2.4	NGC 188 . . . . .	33
2.2.5	Discussion . . . . .	37
2.3	Multi-epoch radial velocities . . . . .	38
2.3.1	Method . . . . .	38
2.3.2	OB binary properties . . . . .	41
2.3.3	Monte Carlo simulations . . . . .	45
2.3.4	R136 . . . . .	50
2.3.5	Discussion . . . . .	56
2.3.6	Effectiveness of multi-epoch radial velocities . . . . .	57
2.4	Conclusions . . . . .	60
<b>3</b>	<b>Westerlund I: stability of a young, massive cluster</b>	<b>65</b>
3.1	Introduction . . . . .	66
3.2	Observations & data reduction . . . . .	67
3.3	Results . . . . .	69
3.3.1	Radial velocity variations . . . . .	69

---

3.3.2	Radial velocity dispersion . . . . .	73
3.4	Discussion . . . . .	75
3.5	Conclusions . . . . .	77
3.A	Appendix: Velocity dispersion in ellipsoidal cluster . . . . .	78
<b>4</b>	<b>IC 348</b>	<b>81</b>
4.1	Introduction . . . . .	81
4.2	Observations . . . . .	82
4.2.1	Target selection . . . . .	82
4.2.2	APOGEE . . . . .	83
4.3	Spectral analysis . . . . .	85
4.3.1	Forward modeling . . . . .	86
4.3.2	Precision and accuracy . . . . .	89
4.4	Stellar luminosities and masses . . . . .	94
4.4.1	Extinction . . . . .	95
4.4.2	Stellar luminosities . . . . .	97
4.4.3	IC 348 cluster mass . . . . .	99
4.5	Results . . . . .	100
4.5.1	Global velocity dispersion . . . . .	101
4.5.2	Velocity gradient with extinction . . . . .	102
4.5.3	Spatial dependence of the velocity distribution . . . . .	103
4.5.4	Spatially correlated velocities . . . . .	105
4.6	Discussion . . . . .	107
4.6.1	Virial equilibrium . . . . .	107
4.6.2	Signature of collapse . . . . .	108
4.7	Conclusions . . . . .	109



## CONTENTS

---

<b>5</b>	<b>Conclusions</b>	<b>111</b>
5.1	Summary . . . . .	111
5.2	Are young massive stellar groups bound? . . . . .	112
5.3	Are low-mass young stellar groups bound? . . . . .	113
5.4	Outlook . . . . .	116
	<b>Bibliography</b>	<b>129</b>
	<b>Curriculum vitæ</b>	

# List of Figures

1.1	Star and gas distribution in several star-forming regions . . . . .	4
1.2	The effect of stellar feedback in 30 Doradus . . . . .	6
2.1	Effect on the observed velocity distribution due to binary orbital motions . . . . .	19
2.2	Spatial distribution of velocity offsets due to binary orbital motions assuming solar-type field star primaries . . . . .	25
2.3	How the precision in the measured mean velocity, velocity dispersion, and binary fraction depends on the velocity dispersion and sample size . . . . .	28
2.4	Systematic offset in the velocity dispersion when the assumed binary properties do not match the real ones . . . . .	30
2.5	Fits to single-epoch velocity distributions observed in NGC 188 . . . . .	34
2.6	Posterior probability distributions of the free parameters in the fit to the single-epoch NGC 188 velocities . . . . .	36
2.7	Orbital parameter distribution for OB stars from three recent literature sources and the resulting radial velocity offset distribution due to binary orbital motions . . . . .	42
2.8	Contribution of stars with different orbital periods to the distribution of radial velocity offsets . . . . .	44
2.9	Systematic offset in the best-fit velocity dispersion due to the uncertainties in the binary properties of OB-stars . . . . .	47
2.10	How the precision in the measured velocity dispersion depends on sample size . . . . .	48

## LIST OF FIGURES

---

2.11	How the reduction in systematic offset in the velocity dispersion for two-epoch data depends on the baseline and measurement uncertainty . . . . .	49
2.12	How the reduction in systematic offset in the velocity dispersion for two-epoch data depends on the ratio of baseline and measurement uncertainty . . . . .	51
2.13	Two-component fit to the surface brightness profile of R136 from Mackey & Gilmore (2003) and the velocity distribution for both components . . . . .	52
2.14	Example fit to a single-epoch velocity distribution in R136 . . . . .	53
2.15	Best-fit binary fraction, velocity dispersion, and mean velocity and the log-likelihood of the best fit for five single-epoch datasets and two two-epoch datasets in R136. . . . .	54
2.16	Histogram of binary orbital periods, radial velocity semi-amplitudes, and velocity gradients relative to the velocity offset caused by the binary . . . . .	58
3.1	Accuracy of velocity zero-point from several telluric lines . . . . .	69
3.2	Observed multi-epoch radial velocity variations in Westerlund I . . . . .	71
3.3	Part of the spectra of the three epochs of the M supergiant Wd1 237 . . . . .	72
3.4	The radial velocities of all epochs of the yellow hypergiants and the luminous blue variable relative to each other . . . . .	73
3.5	Probability distribution of the velocity dispersion observed in Westerlund I compared with several estimates of Virial equilibrium . . . . .	74
3.6	Correction factor for the spheroidal shape of the cluster against the cluster radius along the line of sight . . . . .	79
4.1	Completeness estimate of target catalogue in IC 348 . . . . .	84
4.2	Distribution of stars in target catalogue and observed stars in IC 348 . . . . .	85
4.3	Sample fits of APOGEE spectra of pre-main sequence stars in IC 348 at various effective temperatures . . . . .	87
4.4	The best-fit reduced $\chi^2$ distribution and the external over internal uncertainties for the radial velocity and the veiling . . . . .	90
4.5	Trend of the radial velocity zero-point with effective temperatures in several young star-forming regions . . . . .	91
4.6	Comparison of the effective temperatures measured from APOGEE spectra with literature values . . . . .	94

---

4.7	Distribution of spectroscopic effective temperatures and surface gravities for IC 348, NGC 1333, and the Pleiades . . . . .	95
4.8	The reddening in J-H with respect to the Pleiades as a function of effective temperature in IC 348 and the Pleiades. . . . .	96
4.9	Excess magnitudes in various bands in IC 348 with respect to the Pleiades after extinction-correction . . . . .	97
4.10	Temperature versus extinction-corrected absolute J-band magnitude in IC 348 . . . . .	98
4.11	Correlation between the J-band magnitude and surface gravity relative to other stars of the same temperature in IC 348 . . . . .	99
4.12	Enclosed stellar and gas mass in IC 348 as a function of distance from the cluster center . . . . .	100
4.13	Fit to the observed radial velocity distribution in IC 348 . . . . .	102
4.14	Trend of radial velocity with stellar extinction . . . . .	104
4.15	Lack of a trend of radial velocity with distance from the cluster center . . . . .	105
4.16	Fit to a possible velocity gradient in IC 348 . . . . .	106
4.17	Non-detection of spatially correlated velocities in IC 348 . . . . .	107
5.1	Fit to the velocity distribution in Chamaeleon I . . . . .	114
5.2	Fit to the velocity distribution in Gamma 2 Velorum . . . . .	115

## LIST OF FIGURES

---

# List of Tables

2.1	Constraints on the distribution of orbital parameters (period, mass ratio, eccentricity, and binary fraction) from three recent literature sources for OB stars . . . . .	63
3.1	Observed multi-epoch radial velocities in Westerlund I . . . . .	70

## LIST OF TABLES

---

# Abstract

Young stars form from the gravitationally-driven collapse of dense parts of molecular clouds. A single cloud can form one up to millions of young stars. These stars are initially bound together by the gravity of the molecular cloud in which they formed. After a few million years the cloud disperses and leaves a group of young stars behind which might or might not be bound by the gravity of the stars alone. Most (but not all) older stars are found spread throughout the galaxy, which implies they escaped the gravitational pull of the other stars in their birth environment. It is still debated what processes determine which young stars remain bound together to form an older star cluster and which young stars disperse into the field population.

The aim of this thesis is to investigate early dynamical evolution of these groups of young stars by measuring the dynamical state of the stars as they emerge from the molecular cloud. In particular we study the kinetic and gravitational potential energy of these stellar groups to determine if they are bound or unbound.

The kinetic energy of some stars will be severely overestimated, because they are in a close binary orbit around another star, which causes their measured velocity to be very different than the center-of-mass velocity of the binary system as a whole. I present a maximum-likelihood procedure, which explicitly includes the velocity offsets due to these binary orbital motions, which allows the width of a velocity distribution to be accurately measured using only a single velocity observations per star, instead of multiple velocities per star measured over a timespan of many years.

As part of the thesis I analyzed high-resolution spectra to retrieve line-of-sight velocities in the young massive stellar group Westerlund I and the young low-mass stellar group IC 348. Both have recently emerged from their natal molecular cloud. In Westerlund I we found an upper bound to the velocity dispersion of  $2.1^{+3.3}_{-2.1}$  km s<sup>-1</sup>, implying the cluster is bound. IC 348 has a velocity dispersion of  $0.75 \pm 0.05$  km s<sup>-1</sup>, which also implies that the



## LIST OF TABLES

---

cluster is bound, although the high kinetic energy suggest that it should expand slightly. However, IC 348 appears to be actually collapsing along the line of sight.

Combined with recent results from other groups for other young stellar groups, we consistently find that dense, stellar groups are bound. This implies that these stellar groups are unlikely progenitors of the low-density associations of young stars. It also supports a scenario where a stellar group is unlikely to become unbound due to the expulsion of the natal molecular cloud, when the stars have reached a sufficiently high density prior to the gas expulsion. Although smaller bound stellar clusters will still evaporate on a relatively short timescale due to two-body relaxation, more massive clusters ( $> 10^4$  solar masses) might remain bound for billions of years, if they do not get disrupted by tidal fields of passing molecular clouds or their host galaxy.

# Kurzfassung

Junge Sterne entstehen durch Gravitationskollaps dichter Teile von Molekülwolken. Eine einzige Wolke kann zwischen ein und Millionen von jungen Sterne bilden. Diese Sterne werden durch die Schwerkraft der Molekülwolke, in der sie gebildet werden zusammen gehalten. Nach ein paar Millionen Jahren löst sich die Wolke auf und hinterlässt eine Gruppe von jungen Sternen, denen entweder oder auch nicht von der Schwerkraft der Sterne allein gebunden sind. Die meisten (aber nicht alle) ältere Sterne sind über die ganzen Galaxie verteilt, was impliziert dass sie der Anziehungskraft der anderen Sterne in ihrer Geburts Umgebung entkommen sind. Es wird noch diskutiert, welche Prozesse bestimmen, welche junge Sterne miteinander verbunden bleiben um einen älteren Sternhaufen zu bilden und welche jungen Sterne sich über die Galaxie verteilen.

Das Ziel dieser Doktorarbeit ist es, die frühzeitige dynamische Entwicklung dieser Gruppen junger Sterne zu untersuchen indem der dynamische Zustand der Sterne im Moment gemessen in dem sie aus der Molekülwolke auftauchen. Insbesondere studieren wir die kinetische und potentielle Energie dieser Sterngruppe um festzustellen, ob sie entweder gebunden oder ungebunden sind.

Die kinetische Energie einiger Sterne wird stark überschätzt werden, weil sie sich in einen engen Umlaufbahn um einen anderen Stern bewegen, was bewirkt, dass die gemessene Geschwindigkeit sich von der Mittelpunktsgeschwindigkeit des ganzen Doppelstern stark unterscheid. Ich präsentiere eine Maximum-Likelihood-Methode, das explizit die Geschwindigkeitskorrekturen aufgrund dieser binären Kreisbewegungen umfasst, womit die Breite einer Geschwindigkeitsverteilung mit nur ein Geschwindigkeitsmessung pro Stern genau gemessen werden kann, anstelle von mehreren Geschwindigkeitsmessungen pro Stern über ein Zeitraum von vielen Jahren.

Im Rahmen der Doktorarbeit habe ich Spektren mit hoher Auflösung analysiert und die Geschwindigkeiten entlang der Sichtlinie in der jungen massereiche Sterngruppe Wester-

lund I und den jungen massearmen Sterngruppe IC-348 gemessen. Beide sind vor kurzem aus ihrer Geburtsmolekülwolke aufgetaucht. In Westerlund I fanden wir eine obere Grenze für die Geschwindigkeitsdispersion von  $2.1_{-2.1}^{+3.3}$  km s<sup>-1</sup>, was bedeutet, dass der Sternhaufen gebunden ist. IC 348 hat eine Geschwindigkeitsdispersion von  $0.75 \pm 0.05$  km s<sup>-1</sup>, was bedeutet, dass auch diesen Sternhaufen gebunden ist. Die hohe kinetische Energie lässt darauf schließen, dass IC 348 sich leicht erweitern soll. Im Gegenteil aber, scheint IC 348 entlang der Sichtlinie zu kollabieren.

In Kombination mit den jüngsten Ergebnissen aus anderen Gruppen für andere junge Sterngruppen, finden wir, dass dichte Sterngruppen konsequent gebunden sind. Dies bedeutet, dass diese Sterngruppen wahrscheinlich nicht Vorfahren der geringe dichte Bewegungshaufen junger Sterne sind. Dies unterstützt auch ein Szenario, in dem eine die Abstossung der Molekülwolke nicht die gravitationelle Bindung der Sterngruppe aufheben kann, wenn die Sterne vor der Gasabstossung eine ausreichende Dichte erreicht haben. Obwohl kleiner gebunden Sternhaufen immer noch in einem relativ kurzen Zeitraum durch Zwei-Körper-Entspannung verdunsten, können massivere Sternhaufen ( $> 10^4$  Sonnemasse) für Milliarden von Jahren gebunden bleiben, wenn sie nicht durch die Gezeitenfelder von anderen Molekülwolken oder der beherrschende Galaxie gestört werden.

# 1 | Introduction

Nearly all visible light in the Universe has been directly emitted from a star or from a galaxy containing billions of stars. Although their contribution to the total evolution of the Universe might be minor compared to the gravity of dark matter or the expansive force called dark energy, star light is still crucial to probe the effect of these forces. Many stars also host planets and provide the light and energy to make some of those planets habitable.

Despite their central importance to astronomy, many questions remain about how these stars actually form. Stars are known to form in diffuse, cold, molecular clouds of gas, which contract under gravity to form stars. Although some clouds appear to form only a single star (Alves et al. 2001), most star-forming clouds in the solar neighborhood form tens to thousands of stars (Lada & Lada 2003). Both the massive young clusters observed in starburst galaxies (Holtzman et al. 1992) and the globular clusters surrounding our own galaxy imply that sometimes stars form in groups of up to millions of stars. So to understand star formation, we do not only have to understand the formation of single stars, but also the formation of groups of stars.

Even though most stars in these molecular clouds form in groups, most older stars are spread throughout the galaxy like our own Sun, forming the so-called field population. Thus most of these groups of young stars have to disperse at some point to join the diffuse field population. Other groups of stars remain bound to form clusters. These bound clusters are important astronomical laboratories as they can be identified at large distances and contain a large number of stars with different masses, but the same origin and age. In this thesis I attempt to advance our understanding of which young stars are likely to remain together in bound clusters and which are likely to disperse into the field through a detailed study of the dynamics of these young stellar groups.

Many different definitions for stellar groups and star clusters are used in the literature. Here we will define a stellar group as any overdensity in the stellar distribution, that is not

caused by statistical fluctuations (and is not gravitationally dominated by dark matter to distinguish them from galaxies). Although most known stellar groups are found through their spatial overdensities, so-called moving groups have an overdensity in velocity space (i.e. they have more similar velocities than expected by chance). We split stellar groups in three categories, namely embedded clusters, clusters, and associations. In embedded clusters the stars are bound by the gravitational potential of the molecular cloud out of which the stars formed, in clusters the stars are bound by the gravitational potential of the stars themselves, while in associations the stars are unbound.

This definition and especially the distinction between clusters and associations requires a detailed knowledge of the dynamical state of the stellar group to determine whether it is bound. In practice for most groups we do not know the stellar velocities in most stellar groups, so an alternative classification scheme is required. Low density, diffuse stellar groups are often assumed to be unbound and are thus classified as association. In practice this fits the definition above, because even if the stars have such small relative motions to be formally bound, tidal forces from passing molecular clouds or from the host galaxy itself would cause these diffuse stellar groups to expand. Compact, high density stellar groups are often assumed to be bound and are hence classified as clusters. Gieles & Portegies Zwart (2011) argued that this was reasonable as long as the age of the stellar group is significantly longer than the dynamical time it would take for the cluster to fly apart, because they would not have survived for so long if they were unbound. These arguments allow us to classify diffuse clusters (i.e. larger than the galactic tidal radius) as associations and dense stellar groups that are older than the dispersal time as clusters. However, to determine whether a young, dense stellar group with an age comparable to or smaller than the dispersal time is bound we will actually have to measure the velocities of the stars.

Measuring the velocities in a stellar group allows us to do more than just predicting its future evolution by determining if it is bound by the gravitational potential<sup>1</sup>. It allows us to constrain the dynamical state in which stars form, which can help to clarify the process of how diffuse gas is converted into stars, which is a critical input to models of galaxy formation and evolution. Finally we want to understand the dynamics of the environment in which not only stars form, but also the planets orbiting those stars (Parker & Quanz 2011).

In this introduction I first describe a potential scenario for the formation and evolution of star clusters in section 1.1, with a description of star and embedded star cluster formation in section 1.1.1, a description of the early dynamical evolution of an embedded star cluster and its emergence from the natal molecular cloud in section 1.1.2, and a description of the longer-term evolution of bound clusters in section 1.1.3. In section 1.2 I discuss the various observables available to trace the dynamical evolution of a stellar group.

In chapter 2 we discuss how to correct an observed velocity distribution of a stellar

---

<sup>1</sup>The boundedness of a cluster does not tell us everything, because globally unbound systems might still form a bound core of stars (e.g. Baumgardt & Kroupa 2007) and bound systems will still continuously eject unbound stars.

group for the velocity offsets caused by the orbital motions of binary stars. In chapter 3 we use velocities observed for stars in the massive, young stellar group Westerlund I to show that it is a bound cluster. Then in chapter 4 we show the same for the much less massive, young stellar group IC 348. The velocities suggest that this cluster might actually be collapsing. We finally summarize our work in chapter 5, including an outlook to the huge observational progress that will be made in this field in the next few years with several large surveys.

## 1.1 Star cluster formation and evolution

### 1.1.1 Stars form in molecular clouds

Molecular clouds form when the interstellar atomic gas becomes dense enough to produce molecules (e.g.  $\text{H}_2$  and CO) faster than it is destroyed by the ionizing radiation permeating the Milky Way. These molecules then shield the molecular cloud from the ionizing interstellar radiation, which allows the gas to cool to  $\sim 10$  K (Larson 2005; Crapsi et al. 2007). Many scenarios have been proposed to explain the high densities needed to form these molecular clouds (see Dobbs et al. 2013, for a review). They might form through converging flows driven either by turbulence in the interstellar gas or supernova explosions. Alternatively they could form by the convergence caused by the spiral arms seen in many disk galaxies (such as our own Milky Way). Giant molecular clouds could also form due to Toomre Q or Parker instabilities in the interstellar medium. Finally giant molecular clouds could form out of mergers or collisions of previous molecular clouds.

Molecular emission lines observed in molecular clouds are often much broader than expected from the thermal linewidth, which implies the presence of supersonic turbulent motions over a wide range of spatial scales (Larson 1981; Heyer & Brunt 2004). The Herschel Space Telescope has recently found evidence for turbulence in the density structure of molecular clouds by observing dust emission in the sub-millimeter (André et al. 2010; Arzoumanian et al. 2011). Many local clouds were observed as part of the Herschel Gould Belt survey, all of which showed dense filaments surrounded by lower density gas. Although the detailed formation and evolution of filaments are still not understood (e.g. Arzoumanian et al. 2013), they show up in all hydrodynamical simulations with turbulence, suggesting they are a universal feature of the chaotic and often converging flows in such a medium (see review from André et al. 2013).

If the filaments are too dense, they become unstable, which leads to the formation of dense gas cores (Inutsuka & Miyama 1997), which are indeed often seen by Herschel along the filaments (Men'shchikov et al. 2010; Polychroni et al. 2013). The turbulence in many of these dense cores appears to be subsonic (e.g. Pineda et al. 2010). If these dense cores are gravitationally bound and lack an identifiable protostar, they are referred to as prestellar cores, because they are expected to collapse to form a single or a small number of stars as described by Masunaga et al. (1998) and Masunaga & Inutsuka (2000).

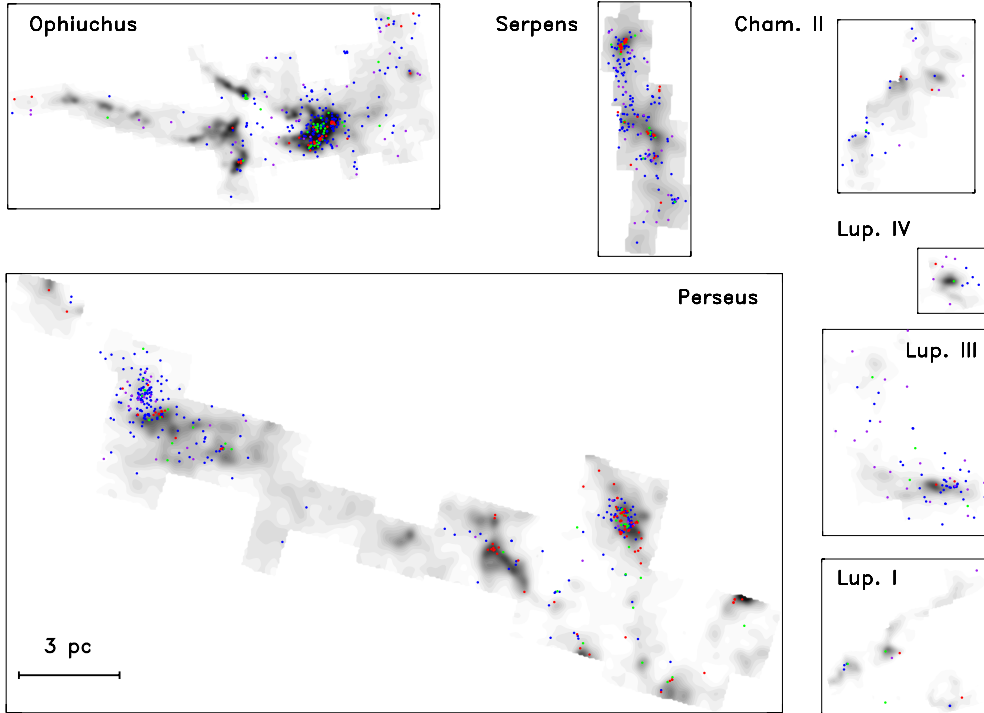


Fig. 1.1 — Greyscale image of the extinction for several young star-forming regions on the same spatial scale. All young stellar objects found with a combination of 2MASS (near-infrared) and Spitzer (mid- and far-infrared) photometry have been overplotted. These young stellar objects have been classified based on the excess emission observed by Spitzer in classes from class I (red), flat (green), class II (blue), and class III (purple). This represents a rough sequence in age from young to old. Figure taken from Evans et al. (2009)

The filamentary substructure observed in molecular clouds and the distribution of the prestellar cores along those filaments imply that stars do not form uniformly throughout the cloud, but rather in dense clumps (as indeed observed in many star-forming regions; e.g. Figure 1.1 Teixeira et al. 2006; Schmeja et al. 2008). These dense clumps can later merge to form a larger stellar group. For many stars this initial clump is the densest environment they will inhabit. So the likelihood of a star closely encountering another star might be set by the initial density in these clumps. This density depends strongly on whether every prestellar core only forms a single star or a binary star in which case the initial stellar density is set by the distance between the prestellar cores and hence the instability in the filaments (Inutsuka & Miyama 1997). On the other hand if the prestellar core is efficiently cooled during collapse, it can continue fragmenting into smaller pieces due to the Jean’s instability, leading to the formation of a (probably unstable) multiple star system (Sterzik & Durisen 1995; Reipurth & Clarke 2001). This fragmentation could continue until the gas becomes dense enough to become opaque to its own radiation, which corresponds to the formation of the so-called first hydrostatic core (Larson 1969), which is predicted to have a radius of about 5 AU (Masunaga et al. 1998). This implies that in

such a case stars could form within a few tens of AU from each other, ensuring many close encounters of these young protostars (Sterzik & Durisen 2003; Umbreit et al. 2005), as was seen in early hydrodynamical simulations which included only turbulence and gravity, but no stellar feedback or magnetic fields (Bate et al. 2003). Multiple systems with even closer separations could later form from fragmentation of the massive circumstellar discs observed to surround young stars.

As soon as the first stars form, feedback from the stars starts affecting the natal molecular cloud. This feedback is due to both radiation (either ionizing or non-ionizing) or outflows (either collimated jets or uncollimated stellar winds). The precise effect of this feedback depends strongly on the type of feedback and how well it couples to the gas (Krumholz & Thompson 2012), however the two main effects can be summarized as transferring momentum to the molecular cloud, which can potentially unbind the cloud, and heating of the surrounding gas (see review from Myers et al. 2014). This heating raises the thermal support against collapse, which increases the size scale on which fragmentation is important (Offner et al. 2009; Price & Bate 2009; Peters et al. 2010; Klassen et al. 2012). If the cloud contains many massive stars, the total feedback can completely disrupt the cloud as illustrated in Figure 1.2.

Although most of the gas is molecular, there are still enough ions around for the gas motions to be significantly affected by magnetic fields (see Crutcher 2012, for a review on the magnetic fields observed in molecular clouds). Observations of magnetic field strengths and their dependence on density show that while the motions in the atomic interstellar medium are parallel to the magnetic fields. In molecular clouds turbulence and/or gravity are able to overcome the magnetic pressure and tension, which allows motions perpendicular to the field lines (Crutcher et al. 2010). However, magnetic fields still play an essential role in supporting to cloud against collapse, especially the low-density material. This can lead to groups of star-formation being better separated, increasing the level of substructure on large scales (Myers et al. 2014). The extra support provided by magnetic fields can also reduce fragmentation on smaller scales and delay the onset of star formation (e.g. Price & Bate 2009; Myers et al. 2014).

These simulations suggest that stellar feedback and magnetic fields might be crucial in determining whether a prestellar core forms a single star, a binary system, or an unstable multiple system through fragmentation of the prestellar core. For nearby cloud fragmentation on these scales can be probed directly through sub-millimeter interferometry, e.g. with ALMA. Alternatively ejections from unstable multiple systems could be detected in the dynamical state of protostars in young embedded clusters, providing an indirect constraint on the importance of stellar feedback and magnetic fields on these small scales.

Besides the substructure, molecular cloud observations provide other important clues on the initial conditions of stars. Despite being embedded in a turbulent molecular cloud, many prestellar cores move with very similar velocities with core-to-core radial velocity dispersions of only 200 - 400 m s<sup>-1</sup> (e.g. in the Rho Ophiuchi molecular cloud André et al. 2007 and the Perseus molecular cloud Kirk et al. 2007). These dispersion are much



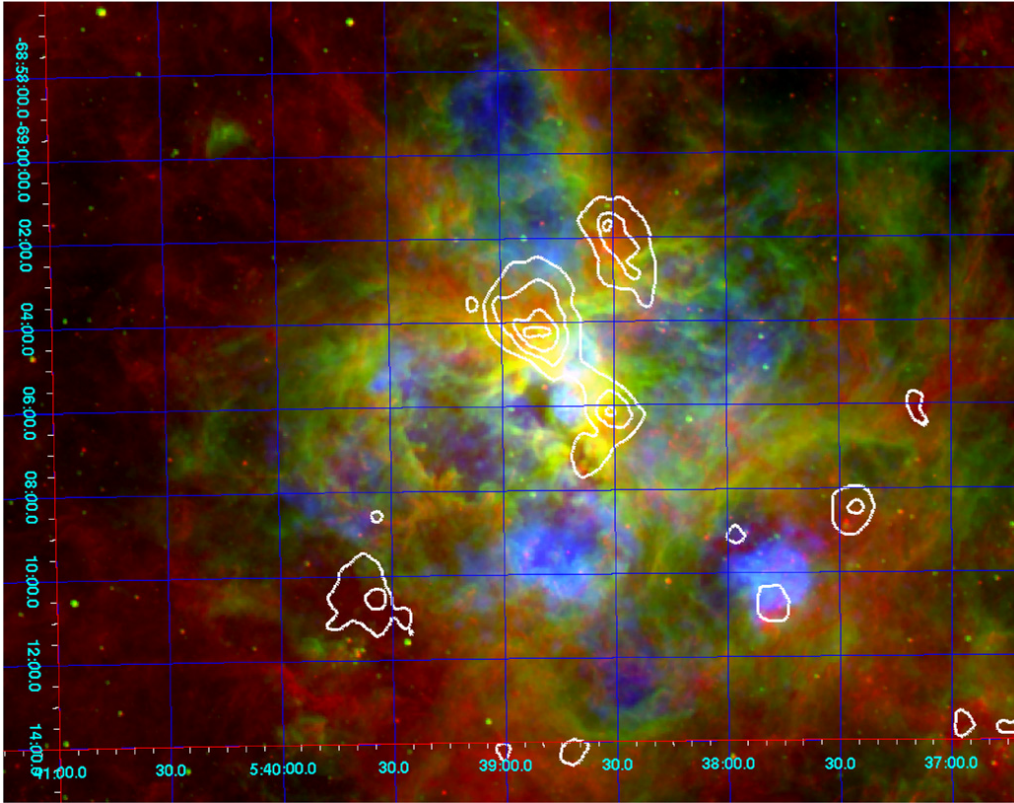


Fig. 1.2 — Three-color image of 30 Doradus, which contains the massive compact star cluster R136, which we will study in more detail in section 2.3.4. Red shows 8 micron thermal emission from gas heated by non-ionizing radiation, green shows  $H\alpha$  emission from gas ionized by high-energy radiation, and blue shows 0.5 - 8 keV X-ray emission from extremely hot ( $\sim 10^7$  K), adiabatically expanding gas produced by shocks in stellar winds. Finally the white contours show small pockets of remaining molecular gas as traced by  $^{12}\text{CO}$  emission. Figure taken from Lopez et al. (2011).

smaller than the turbulent motions in the molecular cloud, which is possibly caused by the formation of these dense cores in the converging flows that formed the host filaments. The stars forming from these prestellar cores inherit these velocities, implying a very low initial velocity dispersion for the stars (unless the velocity dispersion is immediately pumped up by ejections from unstable multiple systems within a prestellar core).

These slow-moving cores only contain a small fraction of the total gas mass in a molecular cloud. Even within a prestellar core the star-formation efficiency is on the order of 20-40% (assuming a prestellar core forms only a single star) (Alves et al. 2007). On larger scales of the whole molecular cloud the star-formation efficiency is even lower: 1.5 - 3% per million years (Myr) (Evans et al. 2009) and a typical duration of star-formation of only up to about 3 Myr (Hartmann 2001; Reggiani et al. 2011). This implies that the initial stellar dynamical evolution will be dominated by the global gravitational potential of the gas, instead of the other stars.

### 1.1.2 Early cluster evolution

As described above stars form as slow-moving, spatially substructured, and embedded in the potential well of the molecular gas. Initially all of the light emitted by the star is absorbed and then re-emitted in the infrared by a dense envelope of gas surrounding the young protostar. Many such objects have been recently detected and characterized in the mid-infrared by the space telescope Spitzer (Enoch et al. 2009). Counting the frequency of these objects suggests that the envelope dissipates in a few  $10^5$  years, although large uncertainties remain in relating the observed infrared fluxes with the physical properties of the envelope (Evans et al. 2009; Dunham et al. 2014).

Once the envelope dissipates it becomes possible to directly observe the light emitted by the stellar photosphere (if our line of sight is not blocked by the massive disks surrounding these young stars; van Kempen et al. 2009). At this point the stars are best observed in the near-infrared, as they are still deeply embedded within the molecular cloud, which absorbs and scatters the visible light. When the molecular cloud dissipates, the stars become revealed in the visible. Both in the visible and near-infrared high-resolution spectra allow the velocities of these young stars to be measured. Here we describe theoretical expectations on the dynamical evolution of these young stars, with observational constraints on these dynamics for two young stellar groups being discussed in chapters 3 and 4.

The small velocity dispersion observed for the prestellar cores suggest that newly-formed stars will initially fall into the potential well of the molecular cloud. The timescale for such a collapse is given by the free-fall time:

$$t_{\text{ff}} = \sqrt{\frac{2d}{g}} \approx \sqrt{\frac{3}{2\pi G\mu \langle n \rangle}} \quad (1.1)$$

where  $d$  is the distance from the star in question to the center of mass,  $g$  is the gravitational acceleration towards this center of mass,  $\mu \approx 2.3$  is the mean molecular weight (for solar composition) and  $\langle n \rangle$  is the number density of the cloud within a distance  $d$  from the center of mass, which with the (poor) assumption of spherical symmetry is all the mass we need to consider when computing the gravitational attraction. For a typical number density of  $390 \text{ cm}^{-3}$  for star-forming molecular clouds (Evans et al. 2009) this gives a free-fall time of 2 Myr, which is the time needed for stars formed all over the cloud to converge into the center of the cloud, where all the clumps formed in different filaments can merge into a single, dense stellar group (Goodwin & Whitworth 2004; Allison et al. 2010; Smith et al. 2011a; Parker et al. 2014). This free-fall time is also often referred to as the dynamical time.

During this collapse the kinetic energy increases as the stars travel into the potential well of the gas. This will continue until the random motions of the stars suffice to counteract the gravity. This equilibrium is referred to as the virial equilibrium and is reached when the kinetic energy  $T$  reaches half of the negative gravitational potential energy  $U$ :

$$T = -\frac{1}{2}U. \quad (1.2)$$

This holds both for a self-gravitating systems (like a star cluster without gas) or a system within an external potential field (like the embedded clusters discussed here). A cluster with a smaller kinetic energy is referred to as subvirial and will collapse in the free-fall time to *revirialize*. Similarly a cluster with a larger kinetic energy is supervirial and will expand to revirialize (unless  $T > -U$  in which case the cluster is unbound and can continue expanding without ever reaching a new equilibrium).

Rather than considering revirialization as a readjustment of the kinetic and potential energy, more about the process can be learned by considering the orbital motions of the stars. In a constant, non-changing potential stars will simply orbit the center of mass <sup>2</sup>. The low initial velocities of the stars imply that they start close to the outer edge of their orbit. After some orbits the stars will be at random phases within their orbits, which will be on average closer to the cluster center, so the cluster has collapsed. If the stars have very similar orbital periods <sup>3</sup>, as expected if they start out substructured with correlated positions and velocities, it will take more orbits for the phases of the stars to become effectively uncorrelated (i.e. the stars will for the first few orbits be at periastron and apastron at roughly the same time). This leads to clusters fluctuating between collapse (as the stars move to periastron) and expansion (as the stars move to apastron) over several orbital times, before they virialize. Indeed these fluctuations have been observed in N-body simulations that start with substructured initial conditions (e.g. Goodwin 2009).

In reality the background global gravitational potential is not fixed, but constantly changes due to both the stellar collapse described above and due to structural variations in the turbulent molecular cloud. This leads to the family of possible orbits constantly changing and hence the orbits of the stars themselves will constantly change, leading to a randomization of the stellar orbits, referred to as *violent relaxation* (Lynden-Bell 1967; Sylos Labini 2012). This will have the effect of changing some of the initially very elliptical orbits (due to the low initial velocities) into more circular orbits. Because stars with different masses are affected in the same way by the global potential, violent relaxation does not differentiate between massive and low-mass stars (unless the massive stars are on different orbits). This distinguishes it from the dynamical friction and relaxation discussed below.

The early dynamical evolution of an embedded cluster is not only affected by the global potential of the gas through the initial collapse and violent relaxation, but also by the local potential. Stars and stellar groups moving through a molecular cloud attract the surrounding gas, leading to a increased density behind the perturber. This increased density then attracts the perturber, causing it to slow down (Ostriker 1999). This effect is referred to as *dynamical friction* and can decelerate objects to the sound speed (Indulekha 2013). This deceleration can assist in the accumulation of stars and groups of stars at the center of the potential, if the molecular cloud is sufficiently dense (Indulekha 2013).

---

<sup>2</sup>In complex potentials the orbits do not have to be ellipses, but stars can follow paths that orbit the center of mass many times before returning to their original positions or velocities. Some orbits can even be chaotic, in which case no return to the original state is expected (Binney & Tremaine 2008).

<sup>3</sup>These orbital periods of the initially elliptical orbits will be twice the free-fall time (i.e. the time needed to fall into the cluster center plus the time needed to return to the original position)

The young stars do not stay embedded inside the molecular cloud. In fact very few embedded clusters are found older than a few Myr (Leisawitz et al. 1989; Lada & Lada 2003), suggesting that the molecular cloud disperses in the first few Myr of a cluster's lifetime. For massive clusters this *gas expulsion* is likely caused by the stellar radiation and outflows unbinding the molecular cloud (see Figure 1.2) (e.g. Dale et al. 2012, 2013). If these forces have not succeeded in unbinding the molecular cloud after a few Myr, the most massive stars will go supernova, driving away any remnants of the molecular cloud. For less massive clusters the dispersal mechanism is more uncertain, as the lack of massive stars in such clusters limits the effects of stellar feedback. Potentially these clouds unbind due to tidal interactions with other molecular clouds or they might have been globally unbound all along (which might help explain the small number of stars formed) (Bonnell et al. 2011; Dobbs et al. 2011).

This dispersal of the molecular cloud significantly reduces the depth of the gravitational potential well in which the stars reside. This change in the global potential might not only cause violent relaxation, but could also unbind the cluster depending on (i) the star-formation efficiency, (ii) whether the stars had already reached virial equilibrium before the gas expulsion, (iii) the timescale of the gas expulsion, and (iv) the relative distribution of the stars and the gas. Early analytical approximations (Hills 1980; Elmegreen 1983) and N-body simulations (Tutukov 1978; Lada et al. 1984; Goodwin & Bastian 2006; Baumgardt & Kroupa 2007) showed that a gas expulsion faster than the dynamical timescale needed to revitalize could unbind a cluster with star-formation efficiencies less than 50%, while clusters could survive with star-formation efficiencies of down to 30% if the gas expulsion was gradual. The actual star-formation efficiencies in molecular clouds are only on the order of a few percent, which suggests that star-forming regions will always unbind. However, these calculations made the simplifying assumptions that the stars were in virial equilibrium with the potential of the gas and that the gas and stars have the same density distribution (e.g. Chen & Ko 2009).

In reality the free-fall time of  $\sim 2$  Myr is on the same timescale as the gas removal time, suggesting that the stars might still be in collapse at the time the gas is removed (Goodwin 2009). This could increase the likelihood of a bound cluster forming afterwards. Furthermore due to the collapse and the dynamical friction described above the stars will typically be much more compact than the gas, which means the contribution of the gas at the scale of these young stars might be much less than the star-formation efficiency computed over the whole cloud suggests. This effect could be amplified, if the stars efficiently accrete the remaining gas in these embedded star clusters. This formation of a gas-poor, dense stellar group is also seen in recent smoothed-particle hydrodynamics (SPH) simulations (Moeckel & Bate 2010; Kruijssen et al. 2012).

From this analysis we might expect that bound clusters are most likely to be formed out of star-forming regions which efficiently undergo collapse before the gas is removed, either because of small initial velocities or due to dynamical friction. In such a condition the stars can reach a dense state, where locally the stellar potential overwhelms the gas potential, minimizing the effect of gas expulsion. This high star to gas mass ratio can be further enhanced by efficient accretion onto the stars. On the other hand associations

are more likely to form in star-forming regions where the global collapse is too slow to merge the small groups of stars or the collapse is prevented altogether due to large initial stellar velocities (possibly pumped up by ejections from unstable multiple systems formed in prestellar cores). When the gas is expelled, these clumps of stars will be unbound with respect to each other and move apart forming an association. Even if some clumps are internally bound (as observed for Gamma 2 Vel by Jeffries et al. 2014), they will quickly dissolve due to two-body relaxation (Moeckel et al. 2012).

### 1.1.3 Long-term cluster evolution

If the stellar group survives the gas expulsion and becomes a bound cluster, it will revitalize in a few dynamical times. The evolution of the cluster does not end at that point, but continues due to *relaxation*. Relaxation is similar to the violent relaxation discussed above in that it alters the orbits of the stars around the center of mass. However, the orbit now doesn't change due to changes in the global potential, but due to changes in the local potential, because the density distribution is not continuous, but discretized into individual stars. So at small scales the potential keeps changing as stars move around. In other words, if stars come too close to each other their orbits get deflected due to the gravitation of the other star. The timescale on which this effect is important (i.e. the relaxation timescale) can be estimated by multiplying the frequency of these interactions by the number of interactions needed to completely randomize the orientation of a stellar velocity, which gives (Binney & Tremaine 2008):

$$t_{\text{relax}} \approx \frac{0.1N}{\ln N} t_{\text{dyn}}, \quad (1.3)$$

where  $N$  is the number of particles and  $t_{\text{dyn}}$  is the dynamical time (i.e. the free-fall time). For stellar groups with few stars ( $N < 100$ ) the relaxation time is very comparable to the dynamical time (or gas dispersal time), making this an important effect to consider in the early dynamical evolution. For larger stellar groups relaxation will only become important for older clusters that remain bound.

Relaxation causes a net transfer of energy from the hot stars in the center to the cooler stars in the outskirts (Lynden-Bell & Eggleton 1980; Gieles et al. 2011). This transfer causes the central stars to collapse and form a dense core, while the cooler stars expand and form a halo. Despite the energy transfer to the halo the core only heats up as it revitalizes, so the transfer of energy only increases the kinetic energy difference between the core and the halo (i.e. the core has a negative heat capacity). Similarly the halo actually cools down, while energy is transferred to it from the core. This cooling is further increased by the escape of any fast-moving halo stars. These negative heat capacities cause the collapse of the core to continue, until a central energy source prevents further collapse. This energy is often assumed to come from star-binary interactions in which energy is transferred from the binary orbit to the star (e.g. Kim et al. 2002; Heggie et al. 2006; Converse & Stahler 2011), however for some clusters mass loss due to stellar evolution might provide sufficient energy (Applegate 1986; Gieles et al. 2010a). Alternative heating

sources have been proposed, such as the velocity kicks received by white dwarfs at formation (Heyl 2008) and interactions with an intermediate mass black-hole (e.g. Trenti et al. 2007). As the halo expands it will eventually reach the tidal radius beyond which the tidal field from the host galaxy can strip of the stars (see Heggie 2001, for a review on the resulting mass loss). An analytic approximation based on N-body simulations of the effect of this *evaporation* and the mass loss due to stellar evolution (i.e. stellar winds, supernovas, etc.) on the stellar content of the cluster is given by Lamers et al. (2005, 2013). Low-density clusters in the Galactic plane giant molecular clouds can also be disrupted by tidal interactions with molecular clouds on a disruption timescale, which depends on the density of the cluster and the environment of the cluster (Gieles et al. 2006).

These stellar encounters also have the net effect to transfer energy from massive stars to low-mass stars, so the massive stars sink to the center and are preferentially found in the core. This process is called *dynamical mass segregation*. Equipartition (where the kinetic energies of the massive and low-mass stars are equal) is never reached, because the highest-energy low-mass stars are consistently ejected from the cluster and the core of massive stars in the core develops a negative heat capacity, as discussed above.

## 1.2 Tracers of dynamical evolution

In section 1.1 we discussed how the dynamical evolution of a stellar group can be influenced by many processes: revirialization (with possibly fluctuations), violent relaxation, dynamical friction in the molecular cloud, the dispersal of the molecular cloud, and due to relaxation both evaporation and dynamical mass segregation. To determine the relative contribution of all of these processes we need observational constraints on the dynamical state and evolution of stellar groups. Here I will discuss several tracers that can be used to constrain this dynamical evolution.

### 1.2.1 Mass segregation

Mass segregation refers to the spatial separation of stars based on mass, with massive stars having sunk to the center of the cluster. Many young clusters, but not all, do show mass segregation (Schmeja et al. 2008; Parker et al. 2012). The advantage of mass segregation as a tool of studying the dynamical state of a cluster is that there appears to be no way to desegregate a cluster, so this implies that an unsegregated cluster has not yet undergone any of the processes required to get mass segregation.

However, if mass segregation is found, there are many scenarios to explain it. The mass segregation could have been primordial, due to a higher mass accretion rate in the center of the stellar cluster (e.g. Bonnell & Bate 2006). Alternatively dynamical friction has a larger effect on more massive objects, so it can cause more massive stars to sink to the

center of an embedded cluster (Pelupessy & Portegies Zwart 2012; Indulekha 2013). Finally an older cluster will undergo dynamical mass segregation on the relaxation timescale due to the transfer of energy from high-mass to low-mass stars. Because the relaxation time is much shorter in the small-N clumps in which stars form, these small-N clumps can undergo dynamical mass segregate before global collapse and this mass segregation is then conserved when these subclusters merge (McMillan et al. 2008; Allison et al. 2010). This wide variety of possible causes of mass segregation makes it difficult to interpret the origin of any observed mass segregation.

### 1.2.2 Spatial substructure

All local (relatively low-mass) molecular clouds show a large amount of substructure (André et al. 2013), which appears to imprint substructure on the spatial distribution of young stars (Evans et al. 2009). The level of substructure is often measured by the Q-parameter, which is given by the ratio of the mean distance between stars and the mean distance in a minimum spanning tree connecting all stars (Cartwright & Whitworth 2004, 2009). If the stars are organized in several clumps, the distance between these clumps will only enter once in the minimum spanning tree, but many times in distances between individual stars, so the mean distance between stars will increase much more than the mean distance in the minimum spanning tree.

As described above an initial collapse can cause these subclusters to merge, which leads to a wiping out of the substructure as measured by the Q-parameter on a dynamical timescale (Parker et al. 2014), so the retainment of substructure in stellar groups is a clear sign of the youth of the system (or at least of a very recent merger).

On the other hand expanding associations can retain their substructure for much longer (Parker et al. 2014), assuming the clumps did not merge before the expansions started. So any observed substructure in associations suggests that the star-forming region has started to expand (presumably due to gas expulsion) before the subclusters merged. This argument was used by Wright et al. (2014) to argue that the substructure they observed in the association Cygnus OB2 showed that the association had never gone through a dense phase.

### 1.2.3 Binary properties

Close stellar encounters can affect the orbits of binary stars and should leave their imprint on the binary star population. Analytical approximations and simulations of star-binary encounters suggest that wide binaries with orbital velocities less than the typical encounter velocities get preferentially destroyed, while for close binaries interactions preferentially decrease the separation (Hills 1975). To observationally separate these dynamical effects on the binary population from the initial distribution of orbital parameters, requires the

study of a wide variety of different stellar groups at various ages and densities (see review from Goodwin 2010). Recently Parker & Reggiani (2013) showed that the distribution of the secondary to primary mass ratios in binaries is not strongly affected by dynamics and could be used as a probe for the initial conditions of binary stars and hence to understand binary formation.

Unfortunately at present only the field stars in the solar neighborhood allow the orbital properties to be studied in great detail (Raghavan et al. 2010; Janson et al. 2012). These stars show a wide range of orbital separations over 6 orders of magnitude from a few stellar radii to 0.5 parsec (i.e. comparable to the size of a typical star cluster). This wide range of orbital separations means that a wide variety of different techniques are required to retrieve the full set of binary properties, from radial velocity surveys to find the orbital motions of the closest binaries, to high-resolution direct imaging to find visual binaries at intermediate separations, to common proper motion pairs to distinguish the widest binaries from random alignments with background stars. Even with all these different techniques, surveys of binaries will only be complete for the closest stars (and most massive secondary stars). Even for the closest clusters there is a gap in separation between stars observable through radial velocity surveys and those that can be detected through direct imaging. The current observational constraints for many different primary stellar masses and stellar environments is reviewed by Duchêne & Kraus (2013).

Over limited ranges in separation and mass ratio, binaries have been observed in star-forming regions. King et al. (2012b,a) collected the information on visual binaries in five local star-forming regions with a variety of stellar densities. They showed that over the separation ranges that the surveys had in common, there was no significant differences in the binary fraction with density, although the lowest-density star-forming region Taurus did show a somewhat higher binary fraction (King et al. 2012b). Some statistically significant differences were found in the separation distribution between stars in these young regions and the field population (King et al. 2012a). However, Parker & Goodwin (2012) caution that these statistically significant offset could be due to random fluctuations in the initial substructured conditions of these stellar groups, rather than signify a real physical difference between the origin of stars in the field and these star-forming regions.

#### 1.2.4 Virial equilibrium

So far, the discussed tracers have not required the measurement of the present dynamical state of the cluster. Although these indirect tracers can tell us a lot about the dynamical evolution of a stellar group, ideally the velocities of the stars are also measured to get the current dynamical state. Measuring these velocities and using them to constrain the dynamical state of stellar groups is the major focus on the thesis. The first goal is often to determine whether a cluster is in virial equilibrium in which the random motions of the stars are balanced by the gravitational attraction between them.

According to equation 1.2 this requires the calculations of both the potential and the



kinetic energy. For the potential energy we need a model of the density distribution in the stellar group, including both the star and any gas mass. Stellar masses are often computed from the stellar temperatures, which themselves are ideally derived from spectra, but are often derived from photometric colors instead. Stellar mass are poorly constrained with only the masses for our own Sun and double-lined, eclipsing binaries known from first principles (e.g. Feiden & Chaboyer 2012; Torres et al. 2013). For young, still contracting stars observed in these young stellar groups, the masses are even more uncertain with very few eclipsing binaries available at these young ages (see Morales-Calderón et al. 2012, and references therein). So stellar masses often are computed from stellar evolution models, which can be calibrated to the eclipsing binary masses (Hillenbrand & White 2004). The uncertainties in the gas mass are also large, because the dominant component in mass, molecular hydrogen, can not be observed directly. Instead alternative tracers (i.e. molecular lines, dust continuum emission, interstellar reddening) are measured, which then are extrapolated to a total mass based on assumptions about the interstellar medium.

Further uncertainties in the potential energy are added because we see a two-dimensional projection of a three-dimensional density distribution. As long as the observed density distribution is circularly symmetric, assuming spherical symmetry seems reasonable. The expected velocity dispersion has been computed for many commonly observed circularly symmetric density distributions (e.g. Portegies Zwart et al. 2010), leading to a more observationally accessible form for computing virial equilibrium:

$$\alpha = \eta \frac{\sigma^2 r_{\text{hm}}}{GM}, \quad (1.4)$$

where  $\alpha$  is the virial ratio, which is one in virial equilibrium,  $\eta$  is a constant depending on the observed circular density distribution,  $\sigma$  is the one-dimensional velocity dispersion,  $r_{\text{hm}}$  is the half-mass radius (i.e. the radius containing half of the mass),  $G$  is the gravitational constant, and  $M$  is the total mass of the region. However, in a substructured density distribution, any deprojection becomes extremely arbitrary, prohibiting the computation of an accurate gravitational potential. Similarly if the gas mass is significant, assumptions have to be made about the distributions of this gas with respect to the stars. Although it might be possible to base the assumed distribution along the line of sight on the spatial distribution on the plane of the sky, this can still cause large systematic uncertainties, especially considering recent suggestions that most of the observed gas might be surrounding relative gas-poor stellar groups (Kruijssen et al. 2012).

Given a mass and density distribution, the last parameter needed to measure the virial ratio is the velocity dispersion. This requires either measuring the velocity along the line of sight through Doppler shifts in high-resolution spectra (i.e. radial or line-of-sight velocities) or measuring the velocities along the plane of the sky due to astrometric shifts with respect to the background stars (i.e. proper motions). Radial velocities can be obtained for any target, as long as it is bright enough to get high-resolution spectra. However the radial velocity distribution might be greatly affected by binary orbital motions (see chapter 2). On the other hand, proper motions require the stars to be close enough (or fast enough) to shift a detectable amount over the available observational baseline <sup>4</sup>

---

<sup>4</sup>For a precision of  $1 \text{ km s}^{-1}$  a shift in the stellar position of about 0.2 AU over 1 year has to be

In general the velocity dispersion will only be measured for a subset of stars in a stellar group and these stars might not be representative of the whole population. A very common bias is to only observe the brightest (i.e. most massive) stars in a stellar group. If these stars are on similar orbits as the lower-mass stars this will not affect the measured velocity dispersion. However if the stellar group is mass segregated, the massive stars are not representative of the full population of stars. In that case the observed velocity dispersion will have to be compared with the gravitational energy for the population of more massive stars, rather than the gravitational energy of the whole stellar group (see chapter 3 for an example).

Another common bias is to observe a higher fraction of stars in the denser center of the stellar group than in the low-density outskirts. This could be, because the outskirts are outside of the field of view of the telescope, or that confusion with the background populations makes memberships more difficult to determine in the low-density regions. Such a bias can lead to an overestimate of the velocity dispersion of a cluster (because the velocity dispersion is higher in the center), leading to an erroneous conclusion on the virial ratio. This bias can also be understood by considering that virial equilibrium is reached, when all stars are in a random position in their orbits. If only the stars in the center are observed, this will lead the observer to conclude that stars are preferentially located in the inner parts of their orbit, leading to the conclusion that the cluster will expand. This bias can be resolved by computing the radial dependence of the velocity dispersion and fit this to the observed velocities. For a spherical cluster in virial equilibrium this velocity dispersion can be found with the Jeans equation (Binney & Tremaine 2008):

$$\frac{d(n\sigma_r^2)}{dr} + 2\frac{\beta}{r}n\sigma_r^2 = -n\frac{d\Phi}{dr}, \quad (1.5)$$

where  $n$  is the density of tracer particles,  $r$  is the distance from the cluster center,  $\sigma_r$  is the velocity dispersion along  $r$ ,  $\beta$  is the ratio of the velocity dispersion perpendicular and the velocity dispersion parallel to  $r$ , and  $\Phi$  is the gravitational potential. Solving the Jean's equation requires knowledge of the gravitational potential, just as when computing the virial equilibrium from the total energetics. However, the Jean's equation depends on an additional variable, namely the anisotropy ratio  $\beta$ . In the same potential well tangential velocities (i.e. circular orbits) will contribute more the line-of-sight velocity dispersion at large projected radii, while a cluster with more radial velocities (i.e. elliptical orbits) will have a more centrally concentrated velocity dispersion profile. Clusters are often assumed to be transiting from an isotropic in the center to tangentially anisotropic at the outskirts (e.g. Michie & Bodenheimer 1963; van de Ven et al. 2006; Breddels & Helmi 2013), which leads to a flatter velocity dispersion profile with projected radius than expected for a cluster with a purely isotropic velocity distribution.

---

observed. For a distance  $d$  this corresponds to a proper motion of  $0.2 \left(\frac{\text{kpc}}{d}\right)$  milli-arcseconds per year. Gaia (<http://sci.esa.int/gaia/>) will reach a precision of several micro-arcseconds per year.

### 1.2.5 Collapse or expansion

Although the virial ratio does give a prediction of whether a stellar group will expand or collapse, it does not give any information of whether the cluster is already expanding or collapsing. Furthermore, there are often large systematic uncertainties in the computation of the virial ratio, as discussed in section 1.2.4. So, ideally one would want to have a more direct tracer of the collapse or expansion of a stellar group.

Detecting collapse or expansion directly requires measuring the velocities and spatial positions along the same dimension. This is easy with proper motions, where one can check for a preferential orientation of the proper motions towards or away from the center of the stellar group. With radial velocities a proxy has to be used for distance along the line of sight. For embedded clusters one possibility is to use the interstellar extinction, which increases with column depth into the cloud (see chapter 4).

### 1.2.6 Cluster rotation

Measuring the velocities in a cluster can also tell us whether a cluster as a whole is rotating. Because angular momentum is conserved, this quantity should be roughly conserved over the lifetime of a cluster, except for angular momentum carried away by stellar ejections. Even if a large fraction of the total mass and angular momentum of a cluster is lost, the specific angular momentum (i.e. angular momentum per unit of mass) might be reasonably conserved, as long as ejected stars have a similar angular momentum as the bound stars. In embedded clusters the specific angular momentum could change significantly due to angular momentum exchange with the gas, but the specific angular momentum measured for older clusters should often be representative of the specific angular momentum at the time the cluster emerged from the molecular cloud.

Unfortunately, velocity gradients observed in young stellar groups do not necessarily indicate rotation. For example, the velocity gradient might just reflect a shear in the velocities, rather than a circular motion, as Fűrész et al. (2006) suggested for the velocity gradient they observed in Orion. Alternatively this gradient can be caused by non-spherical collapse or expansion (Proszkow et al. 2009; Tobin et al. 2009). Proper motions should be able to distinguish these scenarios, allowing the specific angular momentum of young stellar systems to be determined. Both shearing and aspherical collapse or expansion should not affect older clusters, so these can also be used to determine the specific angular momentum distribution with which they leave their natal molecular cloud.

## 2 | Correcting the radial velocity distribution for binary orbital motions

### Abstract

Radial velocity measurements can be used to constrain the dynamical state of a stellar group. However, for stellar groups with a velocity dispersion smaller than a few  $\text{km s}^{-1}$  the observed radial velocity distribution is broadened by the orbital motions of binary stars, which can lead to erroneous conclusions about the dynamical state of a system. Here I present a procedure to characterize the intrinsic velocity distribution of a cluster from either single or multi-epoch radial velocities even for a velocity dispersion of a fraction of a  $\text{km s}^{-1}$ . I investigate a maximum likelihood procedure, which was pioneered separately by Odenkirchen et al. (2002), Kleyna et al. (2002), and Martinez et al. (2011). Assuming a period, mass ratio, and eccentricity distribution for the binaries in the observed cluster this procedure fits a dynamical model describing the velocity distribution for the single stars and center of masses of the binaries, simultaneously with the radial velocities caused by binary orbital motions, using all the information available in the observed velocity distribution. I test the capability of this procedure to reproduce the velocity dispersion of an observed stellar group, using single-epoch radial velocity data of an open cluster NGC 188, both single- and multi-epoch data for a young massive cluster R136, and Monte Carlo simulations.

We find that if the binary properties are well characterized as for solar-type stars, the procedure can successfully reproduce a velocity dispersion of only  $0.5 \text{ km s}^{-1}$  observed in NGC 188 with a single epoch of radial velocity data. However, if the binary properties are less well known like for OB stars, the method can only just distinguish between an unbound stellar group and a group in virial equilibrium for typical velocity dispersions of young massive stellar groups ( $\gtrsim 4 \text{ km s}^{-1}$ ). By extending the maximum-likelihood method to multi-epoch data, we show that the systematic uncertainties on the fitted velocity dis-

person can be improved to only a few percent by using only two epochs of radial velocities. This procedure offers a promising method to reproduce the width of a velocity distribution corrected for the binary orbital motions.

The results (and most of the text and figures) presented here have already been published in Cottaar et al. (2012b) and Cottaar & Hénault-Brunet (2014).

## 2.1 Introduction

A crucial part of determining the virial state of a stellar group (i.e. whether it is in virial equilibrium or will expand or collapse) is to measure its velocity dispersion (see section 1.2.4). If the radial velocities of a large number of stars is available a more sophisticated dynamical model based on the potential energy and density profile of the stellar group can be tested. In such a model the velocity distribution is not characterized by a single velocity dispersion, but by a velocity distribution which varies with mass and/or distance from the center and this velocity distribution could be non-Gaussian. In the old, massive globular clusters, measurements of the radial dependence of the velocity dispersion have been used to for example show consistency of the stellar dynamics with the King (1965) thermal equilibrium model (Gunn & Griffin 1979), to constrain the anisotropy of the cluster (e.g. van de Ven et al. 2006; Sollima et al. 2012) and even to check for deviations from Newtonian gravity (e.g. Baumgardt et al. 2005; Sollima et al. 2012). These studies were aided by the relatively high velocity dispersions and the relatively low binary fractions (e.g. Gunn & Griffin 1979; Davis et al. 2008) of most globular clusters.

These studies can not be simply extended to lower mass stellar groups because these tend to have smaller velocity dispersions. For small velocity dispersion (i.e. less than a few  $\text{km s}^{-1}$ ) the radial velocities from binary orbital motions can inflate the measured velocity dispersion of a stellar group by many  $\text{km s}^{-1}$  (e.g. Kouwenhoven & de Grijs 2008, 2009; Gieles et al. 2010b; McConnachie & Côté 2010). The importance of these binary orbital motions depends on the original velocity dispersion, the binary fraction and the period, mass ratio, and eccentricity distributions of the binaries in the stellar group. These velocities induced by binary orbital motions completely mask the very small velocity dispersions ( $< 1 \text{ km s}^{-1}$ ) expected in open clusters (e.g. Geller et al. 2008, 2010) and possibly in ultra-faint dwarf spheroidals (e.g. McConnachie & Côté 2010). Even the larger velocity dispersions of young massive clusters (e.g. Bosch et al. 2009; Gieles et al. 2010b; Cottaar et al. 2012a; Hénault-Brunet et al. 2012a), local star-forming regions (e.g. Tobin et al. 2009), and some low-mass globular clusters (e.g. Odenkirchen et al. 2002; Blecha et al. 2004; Sollima et al. 2012) can be inflated by binaries.

In Figure 2.1 we have illustrated the effect of binary orbital motions on the probability density function and cumulative distribution of a single epoch of radial velocity data. The dotted line traces a Gaussian with a width of  $1 \text{ km s}^{-1}$ , representing the velocity distribution of single stars and the center of masses of binaries in the observed cluster. The dashed line

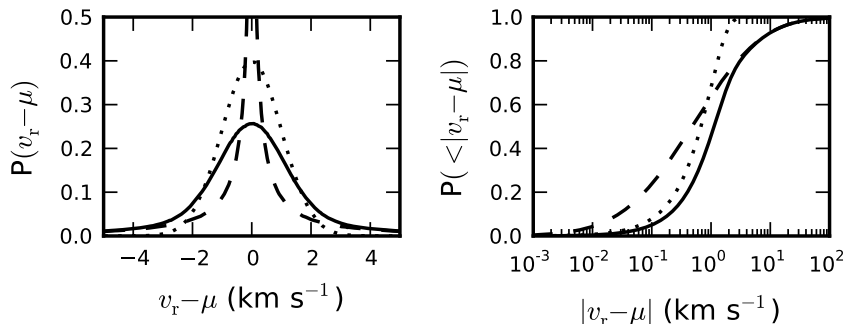


Fig. 2.1 — Probability distribution function (left) and cumulative distribution function (right) for radial velocity offsets from the mean velocity for velocities drawn from a Gaussian distribution with a dispersion of  $1 \text{ km s}^{-1}$  (dotted, equation 2.2), the velocity offsets expected due to binary orbital motions (dashed, equations 2.3 and 2.4), and the velocity distribution for a cluster with a velocity dispersion of  $1 \text{ km s}^{-1}$  and a 100% binary fraction (solid), which is the convolution of the dotted and dashed distribution (equation 2.1). Note that the binary orbital motions have a significant probability of giving a velocity offset on the order of tens of  $\text{m s}^{-1}$ , leading to a very high central peak in the probability density function, which has been cut off in the left panel.

shows the probability distribution of radial velocity offsets induced by binary orbits under several assumptions about the binary properties discussed in 2.2.2. The solid line finally shows the convolution of these distributions, representing the distribution from which the observed radial velocities will be drawn, assuming a binary fraction of 100%. The binary orbital motions both broaden the Gaussian distribution and add a high-velocity tail to the distribution. The goal in this chapter is to present a procedure which can be used after measuring a single epoch of radial velocities (having a distribution similar to the solid line) to characterize the intrinsic velocity distribution (dotted), assuming the binary period, mass ratio, and eccentricity distributions, which corresponds to fixing the shape of the dashed line. This fitting can accurately reproduce the intrinsic velocity distribution, because the velocities added due to binary orbital motions will generally have a very different velocity distribution from the intrinsic velocity distribution.

An often used method to deal with the binary contamination is to obtain multi-epoch observations, which can be used to distinguish between single and binary stars (e.g. Geller et al. 2008; Tobin et al. 2009; Geller et al. 2010; Cottaar et al. 2012a). The single stars (in this context generally defined as stars for which no significant radial velocity variations were found) as well as any binaries for which the velocity of the center of mass has been measured, can then be used to determine the velocity distribution of the cluster. However even after a large number of observations, there might still be undetected binaries, which broaden the measured velocity distribution. For example a circular solar equal-mass binary with a period of a 1000 years, still has a velocity amplitude of  $2 \text{ km s}^{-1}$ .

In absence of multi-epoch data or to correct for any remaining undetected binaries Monte Carlo simulations can be used to estimate for which velocity dispersion the broadening due to an assumed binary population would lead to the observed width of the distribution (e.g. Gieles et al. 2010b; McConnachie & Côté 2010; Sollima et al. 2012). These methods tend to focus on reproducing only the width of the distribution, rather than the full velocity distribution observed.

We investigate here an alternative strategy, which was used separately by Odenkirchen et al. (2002), Kleyana et al. (2002), and Martinez et al. (2011). If the binary period, mass ratio, and eccentricity distributions are roughly known for the type of cluster being studied, this can be used to simultaneously fit the intrinsic velocity distribution and the fraction of binaries. The high-velocity tail caused by the orbital motions of close binaries can be used to determine the binary fraction in the observed cluster, with the distribution of velocities in the tail acting as a test on the assumed binary properties. From the high-velocity tail the effect of these binaries can then be extrapolated to lower velocities to quantify the degree with which the velocity distribution has been broadened by binaries.

It is not obvious that the same method can be applied to successfully recover the intrinsic velocity dispersion of young massive clusters because (1) the OB stars dominating the light of these systems have a high spectroscopic binary fraction (e.g. Sana et al. 2012, and references therein), (2) the distributions of orbital parameters of massive binaries are relatively loosely constrained compared to solar-type stars, (3) higher masses imply more contaminations to the velocity dispersion because the orbital velocity scales with the mass of the primary as  $v_{\text{orb}} \propto M^{1/3}$ , (4) the period distribution of massive binaries generally appears skewed towards shorter periods (see section 2.3.2), which also implies more contaminations, and (5) the accuracy of radial velocity measurements is generally lower for OB stars (typically a few  $\text{km s}^{-1}$  or more) due to rotational broadening of their spectral lines. Dedicated tests of the method using tailored Monte Carlo experiments are therefore needed. It is also desirable to perform tests on a young massive cluster for which the intrinsic velocity dispersion was measured from an intensive dataset of multi-epoch radial velocities (i.e. after selecting out spectroscopic binaries).

In section 2.2 we discuss the proposed method for single-epoch data and test the method by using Monte Carlo simulations as well as by showing that it can reproduce the velocity dispersion of  $0.5 \text{ km s}^{-1}$  observed in the old, open cluster NGC 188 over a 13-year baseline by Geller et al. (2008). This section is based on Cottaar et al. (2012b). Then we will discuss in section 2.3 (published in Cottaar & Hénault-Brunet 2014) an extension to include multiple epochs and how this helps to get accurate velocity dispersion for regions, where the binary properties are poorly constrained. Here we take advantage of the unique dataset provided by the VLT-FLAMES Tarantula Survey (VFTS; Evans et al. 2011). From multi-epoch spectroscopic data of massive stars in the 30 Doradus region of the Large Magellanic Cloud, Hénault-Brunet et al. (2012a) measured the intrinsic velocity dispersion of the young massive cluster R136 ( $M \sim 10^5 M_{\odot}$  - e.g. Andersen et al. 2009; age  $\sim 2 \text{ Myr}$  - e.g. Crowther et al. 2010, de Koter et al. 1998), corrected for the orbital motions of binaries. Sana et al. (2013) studied the spectroscopic binary fraction and distributions of orbital parameters (period and mass ratio) of the O-type stars in the broader 30 Doradus region.

We will use Monte Carlo simulations and the R136 dataset to illustrate the accuracy of the procedure, even when binary properties are poorly constrained. We also provide the necessary python code <sup>1</sup> for calculating the likelihood to reproduce the observed radial velocities given an intrinsic velocity distribution, measurement uncertainties, and a set of binary orbital parameter distributions for both single- and multi-epoch datasets.

## 2.2 Single-epoch radial velocities

In section 2.2.1 we describe the maximum-likelihood analysis we use to fit the intrinsic velocity distribution and the binary orbital velocity distribution. The adopted binary properties based on solar-type field stars are discussed in section 2.2.2. In section 2.2.3 we use Monte Carlo simulations to explore the accuracy of the method, computing the statistical uncertainty as a function of the velocity dispersion, binary fraction, and number of observed stars, as well as the systematic offsets that can be introduced by differences between the assumed and true binary properties. Here we will also provide a tool to estimate the sample size needed to measure the dynamical state or binary fraction of a cluster with a desired precision prior to the observations. We test our model on the old open cluster NGC 188 in section 2.2.4. Geller et al. (2008, 2009); Geller & Mathieu (2011) present multi-epoch radial velocity data for a large number of stars in this cluster and found that the single stars in their data set had a velocity dispersion of  $0.49^{+0.07}_{-0.08}$  km s<sup>-1</sup>. We show that we can reproduce their measured velocity dispersion using only a single epoch of their data. We discuss the limitations of the method in section 2.2.5.

### 2.2.1 Method

We consider a single epoch of  $N_{\text{obs}}$  radial velocity observations  $v_{\text{obs}, i}$  with measurement uncertainties of  $\sigma_{\text{obs}, i}$  of stars with mass estimates  $m_i$ . Our goal is to fit a dynamical model to the binary-corrected velocity distribution of the stars in the cluster for a set of assumptions about the binary period, mass ratio, and eccentricity distributions. As free parameters in this fit we will use the binary fraction in the cluster as well as any parameters used in the dynamical model (e.g. mean velocity, velocity dispersion).

First we calculate the likelihood function, which gives the likelihood of reproducing the observations given the parameters. This likelihood function is unique for every star, as it depends on the measurement error, the mass estimate of the star, and possibly other stellar properties taken into account in the dynamical model (section 2.2.1.1). Then we use the maximum likelihood estimator to convert the likelihood to reproduce the observations as a function of the parameters into a probability distribution of the parameters given the observed radial velocities (section 2.2.1.2).

---

<sup>1</sup><https://github.com/MichielCottaar/velbin>



### 2.2.1.1 Incorporating binaries

The observed velocities can be seen as randomly drawn from the dynamical model ( $v_{\text{dyn}}$ ) describing the intrinsic velocity distribution. We will take the measurement uncertainty into account directly in this dynamical model. So for the single stars this velocity will match the observed velocity. For a random subset of stars (the binaries) we add an additional velocity due to binary orbital motions ( $v_{\text{bin}}$ ). The probability for each star to be a binary depends on the binary fraction of the cluster and the distribution of the added velocities depends on the assumed period, mass ratio, and eccentricity distribution as well as the mass of the star. To calculate the probability of observing a certain velocity ( $v_{\text{obs}}$ ) for a star in a binary, we have to integrate over the probability of any combination of  $v_{\text{dyn}}$  and  $v_{\text{bin}}$ , for which  $v_{\text{dyn}} = v_{\text{obs}} - v_{\text{bin}}$ . This corresponds to taking the convolution of the distributions of  $v_{\text{dyn}}$  and  $v_{\text{bin}}$ . The full velocity distribution is given by the sum of the distributions for single and binary stars:

$$\begin{aligned} \mathcal{L}_i(v_{\text{obs}, i}) &= (1 - f_{\text{bin}})\mathcal{L}_{\text{dyn}, i}(v_{\text{obs}, i}) + \\ &f_{\text{bin}} \int_{-\infty}^{+\infty} \mathcal{L}_{\text{dyn}, i}(v_{\text{obs}, i} - v_{\text{bin}}) \cdot \mathcal{L}_{\text{bin}, i}(v_{\text{bin}}) dv_{\text{bin}}, \end{aligned} \quad (2.1)$$

which gives the likelihood of measuring a velocity  $v_{\text{obs}, i}$  as a function of the binary fraction ( $f_{\text{bin}}$ ) and any other free parameters in the dynamical model. The subscript  $i$  is added to the likelihood function ( $\mathcal{L}_i$ ) to emphasize that this likelihood function is different for every star due to its dependence on the measurement error and the mass of the star. We note that in the derivation of equation 2.1 we assumed that the single stars and the center of masses of the binaries have the same dynamical distribution. Mathematically this assumption is unnecessary and for some dynamical models it might be useful to drop this assumption (e.g. dynamical models that include mass segregation, where the velocity distribution depends on the total mass of a binary).

In equation 2.1 we have not taken any triple or higher-order systems into account. For solar mass these higher-order systems are rare (Raghavan et al. 2010). However, for more massive primaries the fraction of triple and higher-order system is higher (Zinnecker & Yorke 2007; Raghavan et al. 2010). For the system to be stable the radial velocity of any star will still be dominated by a single (generally the closest) companion, which could be either a single star or a multiple system with a much smaller semi-major axis. This implies that the radial velocity offsets expected for a star in triple and higher-order systems can to first order still be approximated by that of a binary.

In this chapter we will focus on measuring the velocity dispersion of a cluster. Using the maximum likelihood estimator the standard deviation and mean of a set of observed velocities can be derived by maximizing the likelihood that the observations were drawn from a Gaussian distribution (Pryor & Meylan 1993). So in order to measure the mean velocity and velocity dispersion corrected for orbital motions of the stars in a cluster, we

will use a Gaussian model to fit the intrinsic velocity dispersion

$$\mathcal{L}_{\text{dyn, i}}(v_{\text{dyn}}) = \frac{1}{\sqrt{2\pi(\sigma_i^2 + \sigma_c^2)}} \exp\left(-\frac{(v_{\text{dyn}} - \mu_c)^2}{2(\sigma_i^2 + \sigma_c^2)}\right), \quad (2.2)$$

which gives the likelihood for a velocity  $v_{\text{dyn}}$  given a measurement error  $\sigma_i$  and the mean velocity  $\mu_c$  and velocity dispersion  $\sigma_c$  of the cluster.

If the observed stars have not been drawn randomly from the cluster, the velocity dispersion of the observed stars is no longer representative for the velocity dispersion of the whole cluster. As most spectroscopic observations will focus on the brightest stars, there will generally be a deviation between the observed velocity dispersion of these stars and the velocity dispersion of the cluster, if the cluster is mass segregated. When the observed stars are not representative of the whole population, a more realistic model could still be fitted. In this case the velocity dispersion ( $\sigma_c$ ) should no longer be taken to be a constant for all stars, but the dependence of the velocity dispersion on the distance from the cluster center or the mass of the star should be modeled. Another possible extension would be to model rotation, by allowing  $\mu_c$  to vary across the cluster. In our efforts to calculate the accuracy with which the intrinsic velocity distribution can be retrieved (section 2.2.3) we will focus on the simple case with only a Gaussian intrinsic velocity distribution and hence on the accuracy with which we can measure a single velocity dispersion. In section 2.2.4 we will have to adjust the model for the intrinsic velocity distribution when fitting the radial velocity data from NGC 188 to take into account the contamination of foreground and background stars in the observed sample.

Given a set of assumptions about the binary period, mass ratio, and eccentricity distributions, we numerically calculate the distribution of radial velocity offsets due to binary orbital motions. We start by randomly drawing a large number ( $\sim 10^5$ ) of binaries with period  $P_j$ , mass ratio  $q_j$  and eccentricity  $e_j$  from the assumed distributions. In addition to these we draw for every binary a random time  $t_j$  since the last passing of periastron. To minimize the time of the computation, we have pre-computed a dense two-dimensional grid giving the relative velocity between the binary components for various eccentricities ( $0 \leq e_j < 1$ ) and phases ( $0 \leq t_j/P_j < 1$ ) for a period of 1 year and a semi-major axis of 1 AU. The velocity taken from this grid can be used to calculate the velocity of the observed star through

$$v_j = \left(\frac{m_i}{M_\odot}\right)^{\frac{1}{3}} \left(\frac{\text{yr}}{P_j}\right)^{\frac{1}{3}} \frac{q_j}{(1+q_j)^{\frac{2}{3}}} v_{\text{grid}}(e_j, t_j/P_j), \quad (2.3)$$

where  $m_i$  is the mass of the observed star, and  $v_{\text{grid}}$  is the velocity calculated for the closest match in eccentricity and phase from the table.

In order to calculate the distribution of velocity offsets, we still have to take into account the projection of the binary motions along the line of sight. Such a projection for a star with an absolute velocity offset  $v_j$  in three dimensions will give a uniform probability between  $-v_j$  and  $+v_j$  to get a certain velocity offset along the line of sight. This flat distribution implies that in the calculation of the total probability to have a velocity offset due to binary

motions of  $v_{\text{bin}}$ , the contribution of all binaries with  $v_j < |v_{\text{bin}}|$  is zero, while all binaries with  $v_j > |v_{\text{bin}}|$  contribute a probability of  $\frac{1}{2v_j}$ . For the list of primary velocities obtained (eq. 2.3) this gives for the likelihood of binary-induced motions to produce a radial velocity offset  $v_{\text{bin}}$

$$\mathcal{L}_{\text{bin, i}}(v_{\text{bin}}) = \sum_{j; v_j > |v_{\text{bin}}|} \frac{1}{2v_j}, \quad (2.4)$$

where we sum the  $\frac{1}{2v_j}$  for all  $v_j > |v_{\text{bin}}|$ . The velocity distribution obtained using equations 2.3 and 2.4 for the solar-type field star binary property distributions discussed above has been shown in Figure 2.1 as a dashed line for a primary mass of  $1 M_{\odot}$ .

In practice we calculate the likelihood velocity distribution for binary-induced motions only for a single primary mass for a dense grid of possible radial velocity offsets. If the mass of an observed star is known, the likelihood distribution can be easily converted to this new primary mass by multiplying the grid of radial velocity offsets with  $\left(\frac{m_1}{M_{\odot}}\right)^{\frac{1}{3}}$  and dividing the computed probabilities by the same amount (keeping the normalization intact). If the period, mass ratio, or eccentricity distribution are known to change as a function of mass or some other observable (e.g. distance from the cluster center), we have to recalculate the likelihood function for binary orbital motions (equations 2.3 and 2.4) for every observed star.

### 2.2.1.2 Fitting parameters

Using equation 2.1 we can combine the intrinsic velocity distribution predicted by the dynamical model (e.g. equation 2.2) with the distribution of velocities due to binary orbital motions (equation 2.3 and 2.4) to calculate the likelihood of observing a given velocity as a function of the binary fraction and any parameters describing the dynamical model of the intrinsic velocity distribution. In its most general form this can be written as  $\mathcal{L}_i(v_i|\mathbf{x})$ , where  $v_i$  is the observed velocity,  $\mathbf{x}$  is the set of free parameters, and  $\mathcal{L}_i$  is the likelihood function, which will be different for every star, because it depends on the measurement error of the observation, the mass of the star, and any other observables included in the dynamical model. The total likelihood of reproducing all observed velocities is then given by  $\mathcal{L}(\mathbf{v}|\mathbf{x}) = \prod_i \mathcal{L}_i(v_i|\mathbf{x})$ . For a large number of observed stars this number will generally get too small for computers to compute (even for a well fitting model), so in practice we calculate the logarithm of the likelihood given by  $\ln(\mathcal{L}(\mathbf{v}|\mathbf{x})) = \sum_i \ln(\mathcal{L}_i(v_i|\mathbf{x}))$ .

The likelihood distribution of reproducing the observation given the parameters ( $\mathcal{L}(\mathbf{v}|\mathbf{x})$ ), which has been computed above, has to be converted to the probability distribution of the free parameters given the observations ( $P(\mathbf{x}|\mathbf{v})$ ). Without any prior information on the probability distribution of the parameters, Bayesian inference states that  $\mathcal{L}(\mathbf{v}|\mathbf{x})$  and  $P(\mathbf{x}|\mathbf{v})$  have the same distribution, with the only difference being is that  $P(\mathbf{x}|\mathbf{v})$  has been normalized

$$P(\mathbf{x}|\mathbf{v}) = \frac{\mathcal{L}(\mathbf{v}|\mathbf{x})}{\int_{\mathbf{x}} \mathcal{L}(\mathbf{v}|\mathbf{x}) d\mathbf{x}}. \quad (2.5)$$

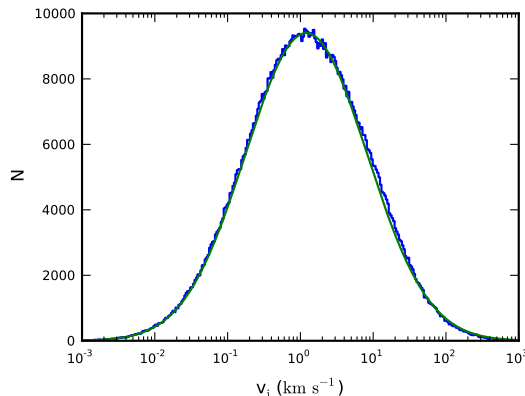


Fig. 2.2 — The distribution of absolute velocities (i.e. not projected along the line of sight) due to binary orbital motions calculated for the period, mass ratio, and eccentricity distributions of the solar-type field stars (see text; Raghavan et al. 2010; Reggiani & Meyer 2011) calculated from equation 2.3 in blue and the best-fit log-normal in green. The log-normal has a width of  $0.84 \log_{10}(\text{km s}^{-1})$  and a mean of  $0.08 \log_{10}(\text{km s}^{-1})$ .

Because the two distributions have the same shape, the set of parameters which maximize the likelihood of reproducing the observations will be the best-fit parameters.

As the number of fitted parameters increases, calculating the normalization in equation 2.5 becomes increasingly computationally expensive. An efficient way to explore the probability distribution of the parameters is through a Markov Chain Monte Carlo simulation. This procedure will take a constrained random walk through the parameter space, producing a chain of parameters, whose distribution follows the probability distribution. So the distribution of the values of a single parameter in this chain, will provide the probability distribution for this parameter, which will be automatically properly marginalized over all the other free parameters.

## 2.2.2 Solar-type binary properties

Because there is a degeneracy between the effects of the period distribution, mass ratio distribution, eccentricity distribution and binary fraction on the observed single-epoch velocity distribution, it is not possible to fully constrain the binary properties using only a single epoch of radial velocity data. So a set of assumptions about these properties will have to be made to model the velocity distribution due to the orbital motions as described in section 2.2.3. Because the binary properties have been shown to significantly change with mass (Burgasser et al. 2007; Raghavan et al. 2010; Chini et al. 2012), the choice of a period, mass ratio, and eccentricity distribution will generally depend on the mass range of the observed stars.

In many clusters the observed stars will tend to be solar-type due to either the evolution of the more massive stars in dwarf spheroidals or low-mass globular clusters or due to the lack of massive stars in low-mass local star-forming regions. So throughout this chapter we will use the well observed binary properties for the solar-type field stars. For the period distribution we use the log-normal distribution with a mean period of 5.03 and a dispersion of 2.28 in  $\log_{10}$  days, which was found by Raghavan et al. (2010). For the secondary to primary mass ratio ( $q$ ) we use the power-law from Reggiani & Meyer (2011) of  $\frac{dN}{dq} \sim q^{-0.5}$  for  $0.1 < q < 1$ . By setting the maximum  $q$  to one we make the assumption that the observed (brightest) star in a binary will always be the most massive one. Raghavan et al. (2010) found a lack of high eccentricities for binaries with low periods. We take this into account by drawing the eccentricities from a flat probability distribution between 0 and  $e_{\max}$  with

$$e_{\max} = \frac{1}{2} \left[ 0.95 + \tanh \left( 0.6 \log_{10} \frac{P}{\text{days}} - 1.7 \right) \right], \quad (2.6)$$

as proposed in Parker & Goodwin (2009). For these binary properties the distribution of the sizes of the three-dimensional velocity differences between the primary star and the center of mass of the binaries (calculated with eq. 2.3) can be very well approximated by a log-normal with a mean of  $0.08 \log_{10} \text{ km s}^{-1}$  and a dispersion of  $0.84 \log_{10} \text{ km s}^{-1}$  (see Figure 2.2).

An important caveat with using the binary properties of the field population is that the solar-type binary properties might not be universal. The field star binary population might simply be a superposition of the binary properties in a large range of different star-forming regions with different binary properties. Furthermore we expect dynamical evolution to have altered the initial binary properties in older clusters (e.g. Marks et al. 2011).

Despite these caveats we show in section 2.2.4 that we can accurately describe the single-epoch velocity distribution of the dynamically old open cluster NGC 188 using the binary properties of the solar-type field stars. In section 2.2.3.2 we will discuss the systematic offsets in the measured velocity dispersion and binary fraction induced, when the binary properties in the observed cluster do not match these assumptions.

### 2.2.3 Monte Carlo simulations

Besides the statistical (random) uncertainty, which can be calculated through the Markov Chain Monte Carlo simulations, there might be an additional systematic error in the best-fit intrinsic velocity distribution if the assumed binary properties do not accurately describe the binaries in the cluster. Here we study the behavior of both the statistical and systematic uncertainty through a large suite of Monte Carlo simulations, where we create fake sets of radial velocity data and fit these with the procedure described in section 2.2.1.

In the Monte Carlo simulations described in section 2.2.3.1 we ensure that there is no systematic error by using the same binary properties to create the radial velocity data sets as we use to fit them, so we can focus purely on the statistical uncertainty and its

dependence on the binary fraction, velocity dispersion, and number of observed stars. In section 2.2.3.2 on the other hand we greatly increase the number of observed stars to minimize the statistical uncertainty, so that we can focus on the effect on the measured velocity dispersion if we use different binary properties to create the data sets as we use to fit them.

Throughout this section we will ignore the effect of the measurement errors of the observed radial velocities. For a normally distributed measurement error and a Gaussian intrinsic velocity distribution, the measurement error and the velocity dispersion are effectively indistinguishable (equation 2.2). As long as the measurement error is sufficiently small that  $\sigma_c^2 \approx \sigma_c^2 + \sigma_i^2$ , the effect of the measurement error on the observed velocity distribution is indeed negligible. For a larger measurement error we can still use the results from this section, however the velocity dispersion should be replaced with the quadratic sum of the velocity dispersion and the measurement error. In this case the measurement error will have to be well quantified in order to retrieve the velocity dispersion.

### 2.2.3.1 Statistical uncertainties

After the velocities have been measured the statistical uncertainty can always be calculated through Markov Chain Monte Carlo simulations. When preparing for observations it is often useful to have an estimate of the accuracies that can be reached based only on the number of stars that will be observed and the expected properties of the cluster prior to any radial velocity measurements.

With this goal in mind we ran Monte Carlo simulations on a large number of fake sets of radial velocities with solar type binary properties (section 2.2.2) with varying binary fractions, velocity dispersions, and sample sizes. These data sets were created for stars with random primary masses between 0.1 and 1  $M_\odot$  following the Chabrier (2005) IMF, which is an update of the IMF presented in Chabrier (2003). For every star we calculated a random radial velocity from a normal distribution with the chosen velocity dispersion (equation 2.2). Every star has a probability set by the binary fraction to be part of a binary system, in which case an additional velocity due to the binary orbital motion is added. The binary properties are randomly chosen from the period, mass ratio, eccentricity and phase distributions and the binary is randomly orientated with respect to the line of sight. The radial velocity dataset created in this way is then fitted using the procedure described in section 2.2.1. Because we used the same assumptions about the intrinsic velocity distribution and the binary properties to create and to fit the radial velocities, there are no systematic offsets in the measured velocity dispersion, mean velocity, and binary fraction with respect to the input velocity dispersion, mean velocity, and binary fraction. For every simulation the uncertainties on the best-fit parameters were calculated through Markov Chain Monte Carlo simulations.

To first order (i.e. ignoring binaries) the uncertainty in the mean velocity is given by the standard deviation of the mean  $\delta\mu_c = \frac{\sigma_c}{\sqrt{N_{\text{obs}}}}$ , where  $\sigma_c$  is the velocity dispersion and

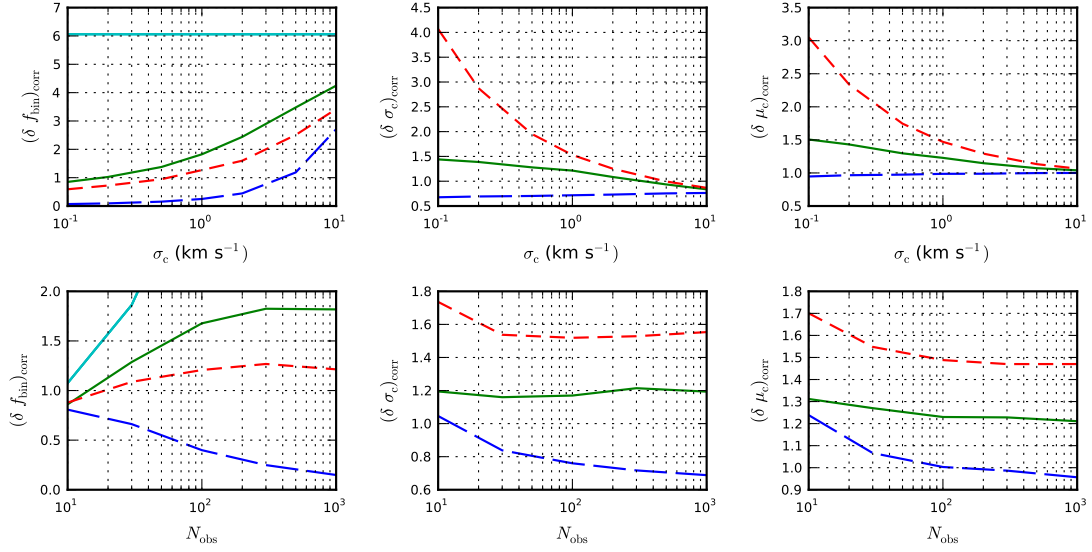


Fig. 2.3 — From left to right the second-order corrections of the uncertainties of the binary fraction  $(\delta f_{\text{bin}})_{\text{corr}}$ , the velocity dispersion  $(\delta \sigma_c)_{\text{corr}}$ , and the mean velocity  $(\delta \mu_c)_{\text{corr}}$ . The top panels show the dependency of these corrections on the velocity dispersion of the cluster ( $\sigma_c$ ) and the lower panels show their dependency the sample size ( $N_{\text{obs}}$ ). These corrections have been computed for the a binary fraction of 0% (blue), 50% (green), and 100% (red). They can be used to calculate the one-sigma uncertainties using equations 2.7a - 2.7c. This allows for the estimation of the accuracy with which the intrinsic velocity distribution can be measured before any radial velocity data has been taken, as long as an estimate for the velocity dispersion and binary fraction are available. The cyan lines in the left panels show the lines with  $\delta f_{\text{bin}} = 0.34$ , which is the expected uncertainty if the binary fraction is unconstrained (i.e. a flat probability distribution between 0 and 1).

$N_{\text{obs}}$  is the sample size. Similarly we expect the velocity dispersion to go as  $\delta \sigma_c \sim \frac{\sigma_c}{\sqrt{N_{\text{obs}}}}$  and finally the uncertainty in the binary fraction to go with  $\delta f_{\text{bin}} \sim \frac{1}{\sqrt{N_{\text{obs}}}}$ .

Using these first-order effects we can write the uncertainty in the binary fraction, velocity dispersion, and mean velocity as

$$\delta f_{\text{bin}} = \frac{(\delta f_{\text{bin}})_{\text{corr}}}{\sqrt{N_{\text{obs}}}}, \quad (2.7a)$$

$$\delta \sigma_c = \frac{(\delta \sigma_c)_{\text{corr}} \sigma_c}{\sqrt{N_{\text{obs}}}}, \quad (2.7b)$$

$$\delta \mu_c = \frac{(\delta \mu_c)_{\text{corr}} \sigma_c}{\sqrt{N_{\text{obs}}}}, \quad (2.7c)$$

where the corrections for the second-order effects due to binaries are given by  $(\delta f_{\text{bin}})_{\text{corr}}$ ,  $(\delta \sigma_c)_{\text{corr}}$ , and  $(\delta \mu_c)_{\text{corr}}$ . Figure 2.3 shows the dependence of these quantities on the velocity

dispersion of the cluster (for  $N_{\text{obs}} = 300$ ) and the number of observed stars (for  $\sigma_c = 1 \text{ km s}^{-1}$ ) for a binary fraction of 0% (blue, long dashes), 50% (green, solid line), and 100% (red, short dashes).

The bottom panels in Figure 2.3 show on the number of observed stars ( $N_{\text{obs}}$ ) for a fixed velocity dispersion of  $1 \text{ km s}^{-1}$ . We find that the second-order corrections on the velocity dispersion and mean velocity becomes independent of  $N_{\text{obs}}$  for  $N_{\text{obs}} > 50$ . This means that the accuracy of the velocity dispersion and mean velocity can be well approximated to go with  $1/\sqrt{N_{\text{obs}}}$ . This dependence becomes unreliable for  $N_{\text{obs}} < 50$ , because the measurement errors themselves vary greatly for small  $N_{\text{obs}}$  and the uncertainty in the velocity dispersion becomes strongly non-Gaussian.

The uncertainty in the binary fraction (bottom left panel) shows a similar behavior, as long as the binary fraction is not too low. For a binary fraction of 50% (green) and velocity dispersion of  $1 \text{ km s}^{-1}$  the binary fraction becomes effectively unconstrained between 0 and 100% for  $N_{\text{obs}} < 100$ . For a binary fraction of 0% we find that  $(\delta f_{\text{bin}})_{\text{corr}}$  declines as the sample size increases, implying that the measurement error in the best-fit binary fraction decrease more steeply than  $1/\sqrt{N_{\text{obs}}}$  over the full range of tested  $N_{\text{obs}}$ .

Because the second-order corrections  $(\delta f_{\text{bin}})_{\text{corr}}$ ,  $(\delta \sigma_c)_{\text{corr}}$ , and  $(\delta \mu_c)_{\text{corr}}$  are constant over a broad range of  $N_{\text{obs}}$  it is possible to calculate the accuracy expected for future measurements from the top panels in Figure 2.3 using equations 2.7a - 2.7c not only for  $N_{\text{obs}} = 300$  for which the figure was calculated, but for any  $N_{\text{obs}} > 50$  given a prior estimate of the velocity dispersion and binary fraction. To fit more complicated dynamical models with more free parameters more stars will of course need to be observed to reach the same accuracy.

For smaller sample sizes these estimates should be taken with caution. For small  $N_{\text{obs}}$  the uncertainties themselves become statistical quantities, which might randomly be much larger (or smaller) than expected. Furthermore the probability distribution of the parameters become non-Gaussian for small sample sizes.

Keeping in mind these caveats equations 2.7a - 2.7c and the top panels in Figure 2.3 can be used to estimate the sample size needed to reach a certain accuracy on the observed velocity dispersion. For example if we consider a local star-forming regions with an expected velocity dispersion of about  $2 \text{ km s}^{-1}$  and solar-type field star binary properties with a binary fraction of roughly 50%, we find from the upper center panel in Figure 2.3  $(\delta \sigma_c)_{\text{corr}} = 1.1$ . To reach an accuracy of 10% on the velocity dispersion (i.e.  $\frac{\delta \sigma_c}{\sigma_c} = 0.1$ ), we find from equation 2.7b that  $N_{\text{obs}} = \left(\frac{1.1}{0.1}\right)^2 = 121$  stars would need to be observed to reach the desired accuracy.

The calculations above were done assuming that the measurement uncertainty is significantly smaller than the velocity dispersion, so that the measurement uncertainty has a negligible effect on the observed velocity dispersion (effectively replacing  $\sigma_c^2 + \sigma_i^2 \approx \sigma_c^2$  in equation 2.2). Actual observations will sometimes include stars for which the measurement



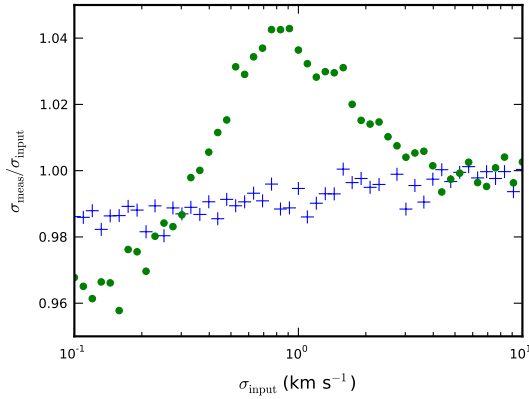


Fig. 2.4 — The ratio between the measured and input velocity dispersion resulting from fits of artificial datasets with varying input velocity dispersions. These datasets were fitted assuming the binary properties of solar-type field star, but were created using different binary period and mass ratio distributions. For the blue '+'-signs the binary population used to create the velocity distribution follows the same field solar-type binary properties used to fit the distribution, except that the mass ratio distribution is flat rather than falling. For the green dots the massive stars follow the solar-type binary properties, while the binary properties of the low mass stars are set by the most likely binary fraction, period distribution, and mass ratio distribution observed for very low mass binaries from Burgasser et al. (2007).

uncertainty is comparable or even larger than the velocity dispersion. These velocities will have a broader likelihood function with the width set by the quadratic sum of the measurement uncertainty and the velocity dispersion (equation 2.2). As seen in Figure 2.3 and equations 2.7a - 2.7c the uncertainty in observed parameters increases for broader distributions, so these measurements will contribute less to the accuracy with which the intrinsic velocity dispersion and binary fraction are measured. However, as the measurement uncertainties are included in the model, these observations can be safely kept in the dataset as long as the measurement uncertainty is well measured. If the measurement uncertainty is only a rough estimate it might be better to remove the observations with the largest measurement uncertainties from the dataset, as an overestimate of the measurement error might cause the velocity dispersion to be systematically underestimated and vice versa.

### 2.2.3.2 Systematic uncertainties

To fit an observed velocity distribution, we have to model the binary orbital motions. This requires assumptions for the binary period, mass ratio, and eccentricity distributions. If our assumed distributions do not match the actual binary properties in the observed cluster, there will be a systematic error in the measured velocity dispersion.

Here we investigate the size of this systematic error by running a set of Monte Carlo simulations. In these simulations we create artificial radial velocity datasets for a given input velocity dispersion and a set of binary properties, which are different than those described for the solar-type field stars discussed in section 2.2.2. We fit these artificial radial velocity data sets assuming the binary period, mass ratio, and eccentricity distribution from the solar-type field stars discussed in section 2.2.2. We then compare the measured velocity dispersion with the input velocity dispersion used to build the artificial dataset and check for a systematic offset between the two.

The measured velocity dispersion will differ from the input velocity dispersion with a random offset due to the statistical noise discussed above as well as a systematic offset due to the discrepancy between the binary properties used to create the artificial dataset and the binary properties used to fit the dataset. Because we are interested here in studying the systematic offset, we minimize the statistical noise by building a very large dataset of  $10^5$  radial velocities. Even with  $10^5$  observed stars there will still be some random scatter in the measured velocity dispersion and binary fraction.

The procedure to build the artificial dataset is the same as for the statistical uncertainties. We briefly summarize it again. We draw the masses of the ‘observed’ stars following the Chabrier (2005) IMF between 0.1 and  $1 M_{\odot}$ . For every star a radial velocity is then drawn from a Gaussian distribution with a given input velocity dispersion. For the randomly assigned binaries a velocity offset due to the binary orbital motions is added.

**2.2.3.2.1 Flat mass ratio distribution** To characterize the distribution of binary orbital motions we assumed a mass ratio distribution of  $\frac{dN}{dq} \sim q^{-0.5}$  (Reggiani & Meyer 2011). However, Reggiani & Meyer (2011) found an uncertainty on this power-law slope of  $\frac{dN}{dq} \sim q^{-0.5 \pm 0.29}$ . This implies that the observed mass ratio distribution is still consistent with being flat at the two sigma level. If the mass ratio distribution were in fact flat, this would cause a systematic offset in the measured velocity dispersion given our assumption of a power-law mass ratio distribution.

To explore this effect we ran a set of Monte Carlo simulations, where we create an artificial ‘observed’ radial velocity dataset assuming a flat mass ratio distributions between  $q = 0.1$  and  $q = 1$  for several input velocity dispersions ranging from 0.1 to  $10 \text{ km s}^{-1}$ . To create these datasets we use the period and eccentricity distributions of the solar-type field stars and fix the binary fraction to the solar-type field star binary fraction (46%: Raghavan et al. 2010). These artificial datasets are then fitted assuming the (correct) solar-type field star period and eccentricity distributions, but with the (here incorrect) power-law slope for the mass ratio distribution. The velocity dispersion measured in this way have been plotted as blue ‘+’-signs in Figure 2.4 for values of the input velocity dispersion between 0.1 and  $10 \text{ km s}^{-1}$ .

The flat mass ratio distribution has a higher fraction of near equal-mass binaries, so every individual binary has a larger probability of creating a significant velocity offset than

for the power law mass ratio distribution. So to reproduce the number of high velocity outliers in the artificial data set created with the flat mass ratio distribution, the fitted binary fraction will be higher than 46% for the power-law mass ratio distribution. We find that the best-fit binary fraction is indeed higher than 46% and increases from 48% for an input velocity dispersion of  $0.1 \text{ km s}^{-1}$  to 55% for an input velocity dispersion of  $10 \text{ km s}^{-1}$ .

The effect of the flat mass ratio distribution is much smaller on the measured velocity dispersion than on the binary fraction. Figure 2.4 shows the ratio of the measured and input velocity dispersion as blue ‘+’-signs. If the assumed binary properties would perfectly match those of the observed cluster this would always be one (except for some random scatter due to the statistical uncertainty discussed in section 2.2.3.1). We see that the difference between the flat and power-law slope for the mass ratio distribution causes an offset of  $< 1\%$  to almost  $2\%$ . This offset increases for lower input velocity dispersion, because the effect of binary orbital motions become more important for narrower velocity distributions.

**2.2.3.2.2 Mass-dependent binary properties** We also consider the case, where the low-mass binaries (primary mass between  $0.1$  and  $0.2 M_{\odot}$ ) in our artificial cluster do not have the same properties as the solar-type field stars, but rather the period distribution, mass ratio distribution, and binary fraction found by Burgasser et al. (2007) for very low mass binaries. The binary properties for these stars are still highly uncertain, but Burgasser et al. (2007) found that the observed binary properties for binaries with primary masses lower than  $0.1 M_{\odot}$  could be fitted by a log-normal period distribution with a mean at  $7 \text{ AU}$  and a width of  $0.24 \log(\text{AU})$ , a power-law mass ratio distribution with  $\frac{dN}{dq} \sim q^{4.8}$  (for  $q < 0.6$ ) and a binary fraction of  $22\%$ . This binary fraction is much lower than that observed for solar-type stars in the field, although the effect per binary on the velocity distribution is much larger, because they tend to be on closer orbits and tend to be equal-mass.

In our simulations the masses range from  $0.1$  to  $1 M_{\odot}$ . Although recent results (Janson et al. 2012) suggest a smooth transition between the binary properties of the very low mass and solar-type stars, we will use a sharp transition between these regimes for this numerical test. For the low mass stars ( $< 0.2 M_{\odot}$ ,  $\sim 34\%$  of all stars) we use the semi-major axis log-normal distribution, the mass ratio power-law distribution (for  $q$  between  $0.1$  and  $1$ ), and the binary fraction found by Burgasser et al. (2007). For the higher mass stars we use the binary properties observed for the solar-type field stars (section 2.2.2) with a binary fraction of  $46\%$ . We once again fit these radial velocities under the (inaccurate) assumption that all stars still have the same binary fraction and follow the solar-type field binary period, mass ratio, and eccentricity distributions. These simulations are repeated for a broad range of input velocity dispersions.

The measured velocity dispersion is shown in Figure 2.4 as green dots. Although the assumed solar-type field binary properties are inaccurate for a third of the ‘observed’ stars, the offset between the measured and input velocity dispersion is still at most  $4\%$ .

These two examples (i.e. sections 2.2.3.2.1 and 2.2.3.2.2) are meant to illustrate the effect of incorrect binary assumptions on the measured intrinsic velocity distribution. For reasonable differences between the true and assumed binary properties, the effect on the intrinsic velocity dispersion turns out to be fairly small. For the cases discussed above only a few percent. It would require observations of thousands of stars, before this systematic offset becomes significant compared to the statistical error. However, if the binary properties are very uncertain, it might still be useful to check how much the intrinsic velocity distribution might vary for several reasonable assumptions about the binary properties (Odenkirchen et al. 2002).

## 2.2.4 NGC 188

As a test for the procedure described above, we will here consider the case of the old ( $7 \pm 0.5$  Gyr; Sarajedini et al. 1999) open cluster NGC 188. The dynamical state of the cluster was extensively studied by Geller et al. (2008, 2009) and Geller & Mathieu (2011). Based on 9166 radial velocity measurements of 1108 stars in the direction of this cluster, Geller et al. (2008) identified a large number of stars with significant radial velocity variations. Based on the remaining (seemingly single) 640 stars, they derive a velocity dispersion of  $0.64 \pm 0.04 \text{ km s}^{-1}$ . This value is still inflated by unidentified binaries. Geller & Mathieu (2011) found that these unidentified binaries would inflate an intrinsic velocity dispersion of  $0.49^{+0.07}_{-0.08} \text{ km s}^{-1}$  to the observed  $0.64 \pm 0.04 \text{ km s}^{-1}$ . In this section we will show that we can reproduce their intrinsic radial velocity distribution using only a single epoch of their data.

We estimate the masses of the observed stars to be given by the closest point on the 7 Gyr Padova isochrone (Marigo et al. 2008) with  $E(B - V) = 0.09$  and  $DM = 11.44$  (following the photometric fit of Sarajedini et al. 1999). The masses of the observed stars estimated in this manner vary between  $0.8$  and  $1.1 M_{\odot}$ . The sample of observed stars contains a significant contamination from fore- and background stars. For these stars we do not expect the computed masses to be accurate. Fortunately in our model the masses only affect the binary orbital motions, which have a negligible effect on the very broad velocity distribution of the fore- and background stars.

These fore- and background stars will affect the intrinsic velocity distribution. Following Geller et al. (2008) we model the radial velocity distribution of the field star population with a Gaussian. Choosing the same distribution to fit the field stars allows us to make direct comparison with the results from Geller et al. (2008). We can add this Gaussian to the model for the intrinsic velocity distribution (equation 2.2) to get

$$\mathcal{L}_{\text{dyn, i}}(v_{\text{dyn}}) = f_c \frac{1}{\sqrt{2\pi(\sigma_i^2 + \sigma_c^2)}} \exp\left(-\frac{(v_{\text{dyn}} - \mu_c)^2}{2(\sigma_i^2 + \sigma_c^2)}\right) + (1 - f_c) \frac{1}{\sqrt{2\pi(\sigma_i^2 + \sigma_f^2)}} \exp\left(-\frac{(v_{\text{dyn}} - \mu_f)^2}{2(\sigma_i^2 + \sigma_f^2)}\right), \quad (2.8)$$

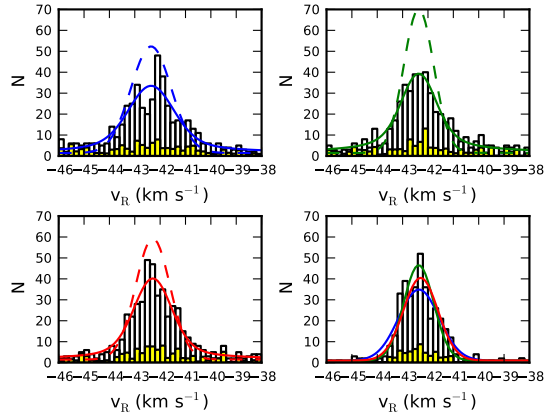


Fig. 2.5 — Histograms of the three single-epoch radial velocity distribution from NGC 188 we consider in the top left, top right and bottom left panels, with the probability distribution of the best fitting model overplotted as the solid line for a star of  $1 M_{\odot}$  and a measurement error of  $0.4 \text{ km s}^{-1}$ . The intrinsic velocity distributions (equation 2.8) are plotted as dashed lines. In the bottom right the histogram of the velocities of the single stars identified in Geller et al. (2008) is plotted. The intrinsic velocity distributions (renormalized to the smaller population) computed from the three data sets have been overplotted. All three of these intrinsic velocity distributions are consistent with the velocity distribution of the single stars from Geller et al. (2008) according to a KS-test (see text). In all panels the fraction of every bin expected to consist of non-members (Platais et al. 2003) have been made yellow. The color coding of the lines corresponds to the data set used to fit the model. The first observed epoch has been shown in blue, the second epoch in green, and the last epoch in red.

where  $f_c$  is the probability of an observed stars to be a cluster member (i.e. the fraction of cluster members) and  $\sigma_f$  and  $\mu_f$  are respectively the velocity dispersion and mean velocity of the non-members. These three parameters will be fitted in addition to the binary fraction ( $f_{\text{bin}}$ ), the cluster velocity dispersion ( $\sigma_c$ ), and the mean velocity ( $\mu_c$ ) of the cluster.

Because multiple epochs of data are available for nearly all of the 1108 stars we are able to run the procedure on three single-epoch radial velocity data sets with only minimal duplication between the data sets. The radial velocities and measurement errors were taken from Geller et al. (2009).

The first three panels in Figure 2.5 show the histograms of the radial velocities in these three data sets with the velocity distribution for the best-fit model overplotted as solid lines. In principle there is no single best-fit distribution, because the velocity distribution depends on the mass of the star and the measurement error. The distributions plotted in Figure 2.5 are for a star of  $1 M_{\odot}$  and a measurement error of  $0.4 \text{ km s}^{-1}$ , which is typical for the vast majority of observed stars. We note that the model has been fitted to the individual observed velocities and is independent of the bin size chosen in Figure 2.5.

The velocity distribution of single stars identified in the multi-epoch data by Geller et al. (2008) is shown in the bottom right panel in Figure 2.5, where we have overplotted the intrinsic velocity distributions found for the first data set (blue), the second data set (green), and the third data set (red). We check whether the observed radial velocity distribution of the single stars is consistent with being drawn from the predicted intrinsic velocity distributions from the single epoch datasets using the Kolmogorov-Smirnov test. The KS test computes the largest deviation between the measured and predicted cumulative distributions and calculates the probability that this deviation or a larger one can be created by chance when drawing random samples from the predicted distribution. If this probability is small, the hypothesis that the measured and predicted distributions are the same can be rejected.

Before we can compare the observed single star velocity distribution with the intrinsic velocity distribution predicted from the single-epoch data, we have to correct for a selection effect. Because priority was given during the observations to proper motion members, the fraction of cluster members in the subset of observed stars with at least three epoch of observations over a baseline of one year is higher than in all observed stars. Because Geller et al. (2008) require stars to have been observed for at least three epochs over at least one year before classifying them as single stars, the fraction of members among the stars identified as single is also higher. Based on the proper motions membership probabilities (Platais et al. 2003) we find the fraction of members among stars classified as single to be 53%, significantly higher than the 44% among all stars.

After correcting for this selection effect by increasing  $f_c$  to 53% the KS test finds that the observed velocity distribution of the seemingly single stars is consistent with being drawn from the predicted intrinsic velocity distribution. The probabilities of drawing a distribution with at least the same offset in the cumulative distribution by chance is 17% for the first data set, 29% for the second data set, and 2% for the last data set. We note that even in the unlikely case that the assumptions going into the model (i.e. Gaussian distribution, field solar-like binary properties) are perfect descriptions of NGC 188, the distributions are still expected to be slightly different, because the observed distribution of stars identified as single might still be inflated by unidentified binaries.

In Figure 2.6 we show the probability distributions for the six parameters we fit in our model. For comparison the literature values for these parameters from Platais et al. (2003); Geller et al. (2008); Geller & Mathieu (2011) have been overplotted. Taking the average of all membership probabilities for all observed stars (Platais et al. 2003), we find that 44% of observed stars should be members. This is fully consistent with the results we find for the three individual data sets (top left panel of Figure 2.6).

For all three datasets we find a binary fraction consistent with being 100% (Fig. 2.6). This high binary fraction should be interpreted with great caution, as we are only sensitive to the close binaries in NGC 188, which affect the observed velocity distribution. If a larger fraction of all binaries in NGC 188 is close compared to the solar-type field binaries, the total binary fraction might be significantly lower. Such a deviation from the binary

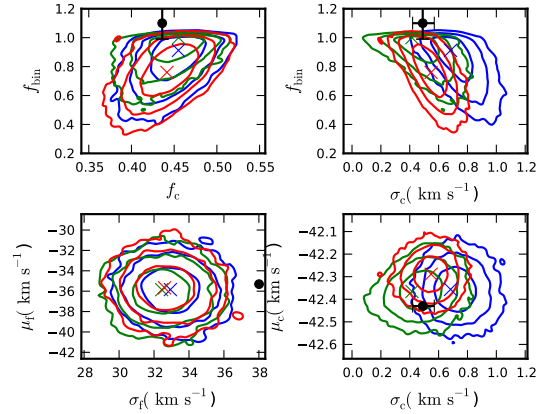


Fig. 2.6 — Posterior probability distributions of the free parameters in the model, enclosing 68.2%, 95.4%, and 99.7% (i.e. 1, 2, and 3  $\sigma$ ) of the total probability. The six free parameters are the binary fraction ( $f_{\text{bin}}$ ), the fraction of cluster members ( $f_c$ ), the cluster velocity dispersion ( $\sigma_c$ ), the cluster mean velocity ( $\mu_c$ ), the field velocity dispersion ( $\sigma_f$ ) and the field mean velocity ( $\mu_f$ ). The different colors refer to the three different single-epoch radial velocity distributions with the same color coding as in Figure 2.5. The literature values for these parameters, derived from a proper motion analysis (Platais et al. 2003) and the multi-epoch radial velocity data (Geller et al. 2008; Geller & Mathieu 2011) have been plotted as black dots. If the error bars are given, they have been plotted.

properties of the solar-type field stars might be caused by dynamical evolution, which decreases the period of the hard binaries ( $P < 10^6$  days in the case of NGC 188, Geller & Mathieu 2011). Evidence for significant dynamical evolution in NGC 188 was found by von Hippel & Sarajedini (1998) and Bonatto et al. (2005).

Irrespective of whether there are wide orbit counterparts to the identified spectroscopic binaries, we can compare the binary fraction found to the spectroscopic binary fraction from the multi-epoch data. Geller & Mathieu (2011) found that  $29 \pm 3\%$  of observed stars in NGC 188 are binaries with periods smaller than  $10^4$  days and  $q > 0.2$ , which makes these type of binaries  $2.4 \pm 0.2$  times as frequent in NGC 188 as in the field. Under our assumptions that the binaries in NGC 188 have the same properties as those in the field, the total binary fraction would then also be  $2.4 \pm 0.2$  times as high. This would lead to the unphysical conclusion that  $110 \pm 10\%$  of stars in NGC 188 are binaries, which is consistent with the very high binary fractions found from the single-epoch data. The estimate of a total binary fraction above the 100% implies that the ratio of spectroscopic binaries to wider binaries is higher in NGC 188 than in the field.

We finally compare the results of our Gaussian fits. Geller et al. (2008) measured a mean velocity of  $-35.31 \text{ km s}^{-1}$  and a dispersion of  $38.01 \text{ km s}^{-1}$  for the non-members. The cluster members have a mean velocity of  $-42.43 \text{ km s}^{-1}$  (Geller et al. 2008) and a velocity dispersion of  $0.49_{-0.08}^{+0.07} \text{ km s}^{-1}$  (Geller & Mathieu 2011). All of the mean velocities

and velocity dispersions measured for our three single-epoch datasets, except possibly the velocity dispersion of the field population for which Geller et al. (2008) do not give an uncertainty, are consistent with the literature values within one to two sigma.

### 2.2.5 Discussion

Above we have shown that the presented likelihood procedure can accurately describe the intrinsic velocity distribution of NGC 188 and find an intrinsic velocity dispersion consistent with that the  $0.49^{+0.07}_{-0.08}$  km s<sup>-1</sup> from multi-epoch data (Geller & Mathieu 2011). This dispersion is accurately found, even though NGC 188 has a large spectroscopic binary fraction and there is a large contamination of fore- and background stars.

In our analysis of NGC 188 we have attempted to use as little prior information about the cluster as possible in order to illustrate the accuracy of the procedure based only on the observed single-epoch radial velocity and the mass estimated of the stars. The accuracy of the procedure could of course be improved by taking constraints from other sources into account. For example one could use the spectroscopic binary properties which Geller & Mathieu (2011) found for NGC 188 instead of the solar-type field binary properties. Furthermore one could set the probability for a star to be a cluster member  $f_c$  to the membership probabilities derived from the proper motion analysis of Platais et al. (2003). Finally one could use a model for the Milky Way (e.g. Robin et al. 2003) to predict the velocity distribution of the fore- and background star instead of fitting a Gaussian to this distribution.

Although we have tested the procedure here on an open cluster, it should be applicable to a broad range of stellar systems where the velocity distribution is significantly inflated due binary orbital motions, such as faint Milky Way companion dwarf galaxies, young massive clusters, local star-forming regions, and some low-mass globular clusters. As long as there is a dynamical model for the velocity distribution of single stars and the center of masses of binaries and a rough approximation of the binary properties, a single epoch of radial velocity data can be used to constrain the dynamical state of the cluster. If enough velocity data is available it can serve as a test on the assumed binary properties for the observed cluster.

#### 2.2.5.1 Limitations

The power of this procedure lies in the difference between the Gaussian intrinsic velocity distribution assumed and the high velocity outliers caused by the binary orbital motions. This implies that if a dynamical model is fitted, where the intrinsic velocity distribution is more similar to the distribution caused by binary orbital motions (i.e. has stronger wings), the accuracy of the procedure would decrease. An example would be a model, which includes the possibility of stars ejected at a high velocity. To distinguish these ejected



stars from velocity outliers caused by binary orbital motions, multiple epochs of radial velocity data will still be required.

We have a similar problem in our analysis of the radial velocity data of NGC 188 (section 2.2.4) where the nature of the high-velocity outliers is unclear. They could either be members, whose velocity is offset due to its orbital motion, or they could be non-members. Due to this confusion the accuracy with which the binary fraction could be measured, was much lower as expected for such a large set of radial velocity data. From the top left panel of Figure 2.3 we find that  $(\delta f_{\text{bin}})_{\text{corr}}$  for a cluster with a binary fraction of roughly 100% and a velocity dispersion of  $0.5 \text{ km s}^{-1}$  is about 0.6. For the  $N \approx 500$  members in NGC 188 equation 2.7a gives an accuracy of 3%. This is much lower than the actual precision with which we could measure the binary fraction of  $\sim 15\%$ .

In addition to distinguishing between velocity outliers due to binary orbital motions and those caused by ejections or non-members, multi-epoch data has the advantage that it can be used to constrain the binary properties of the cluster. In principle the distribution of the high-velocity tail in the observed velocity distribution puts some constraints on the binary properties. If enough radial velocity data is available, this might be sufficient to reject a given set of binary assumptions. However the degeneracy between the effects of the period, mass ratio, and eccentricity distributions and the binary fraction on this high-velocity tail means that these distributions can not actually be fitted.

## 2.3 Multi-epoch radial velocities

In section 2.3.1 we introduce an extension of this procedure that is applicable to multi-epoch data, and discuss available constraints on the binary properties of OB stars in section 2.3.2. We describe Monte Carlo simulations used to test the procedure for single- and two-epoch datasets in section 2.3.3. We then present the R136 dataset and the results obtained when applying the maximum-likelihood method to these data in section 2.3.4. We discuss the implications of these results in section 2.3.5.

### 2.3.1 Method

For a single epoch of radial velocity data, the maximum-likelihood procedure described in section 2.2.1 gives the intrinsic velocity dispersion of a cluster corrected for the effect of binary orbital motions. This works well for stellar populations for which the binary orbital parameter distributions are well constrained (e.g. solar-type stars, Cottaar et al. 2012b). When these are more loosely constrained (e.g. for OB stars), multiple epochs can be used to identify and remove from the sample some spectroscopic binaries, thereby improving the accuracy of the final velocity dispersion determination. However, there will always remain undetected spectroscopic binaries that significantly affect the radial velocity distribution.

We describe below four adjustments to the likelihood procedure that make it possible to accurately estimate the intrinsic velocity dispersion of a cluster from a multi-epoch dataset corrected for the effect of these undetected spectroscopic binaries.

First, we identified as many spectroscopic binaries as possible and removed them from the sample. To identify these binaries, we used a  $\chi^2$ -test to assess whether the radial velocity observations are consistent with coming from a single star without radial velocity variations. For each star, we computed

$$\chi^2 = \sum_i \frac{(v_i - \bar{v})^2}{\sigma_i^2}, \quad (2.9)$$

where  $\bar{v}$  is the weighted mean velocity over all the observed epochs  $i$ , and  $v_i$  and  $\sigma_i$  are the velocities at individual epochs and their uncertainties. By comparing this with the  $\chi^2$ -distribution (with the number of degrees of freedom equal to the number of epochs minus one), we compute the probability that a value as high as the computed  $\chi^2$  can be due to measurement uncertainties alone. If this probability was low, we identified the star as a radial velocity variable and removed it from the sample. In line with previous work on R136 (Hénault-Brunet et al. 2012a), we rejected stars with a probability  $p < 10^{-4}$  of not being a radial velocity variable.

In principle, completely removing these radial velocity variables from the sample is waste of information. However, including this information would require solving the radial velocity orbit of the binary. This is computationally very expensive when only a few epochs are available. Even if it is computed, the uncertainty in the systemic velocity of the binary will tend to be very weakly constrained, therefore it will provide little useful information about the intrinsic velocity dispersion or even the mean velocity of the cluster. Of course the systemic velocity of the binary should be included in the fit of the velocity dispersion (with its appropriate uncertainty), if enough epochs have been observed to solve the binary orbit.

Secondly, we computed for the remaining and apparently single stars the effect of possible unidentified binary on the observed radial velocity distribution. For this, we generated a large population of binaries sampled from the adopted binary orbital parameter distributions and assumed that these systems have random phases and orientations. Using the same  $\chi^2$ -test as for the actual data, we then determined which binaries would have been detected given the timing of the observations and the measurement uncertainties. Eliminating these systems left us with a sample of binaries that would not be detected given the observational constraints. We computed the radial velocity offset distribution due to the orbital motions of these binaries, which gave us  $\text{pdf}_{\text{offset}}$  for binaries which are undetected in the multi-epoch dataset. This was recomputed for every star, because the detectability of binaries strongly depends on the time sampling of the observations and the measurement uncertainties.

Our proposed method differs substantially from the multi-epoch fit from Martinez et al. (2011). These authors used a very similar likelihood procedure to fit their multi-epoch

radial velocity data of the dwarf spheroidal galaxy Segue 1, but they made no explicit distinction between radial velocity variables and seemingly single stars. This distinction allowed us to reach a higher precision, because the systemic velocities of the seemingly single stars have much smaller uncertainties than the systemic velocities of the radial velocity variables. By not distinguishing these populations, Martinez et al. (2011) combined the probability distribution of the systemic velocity for seemingly single stars and radial velocity variables, which led them to underestimate the constraints that the seemingly single stars can put on the intrinsic radial velocity distribution.

After computing the radial velocity offsets due to binary orbital motions for the apparently single stars, we convolved this with an assumed intrinsic velocity distribution and added the contribution from truly single stars (equation 2.1), when using equation 2.1 we kept in mind that the binary fraction among the apparently single stars ( $f'_{\text{bin}}$ ) is lower than among the population as a whole

$$f'_{\text{bin}} = f_{\text{bin}} \frac{1 - f_{\text{det}}}{1 - f_{\text{bin}} f_{\text{det}}}, \quad (2.10)$$

where  $f_{\text{det}}$  is the fraction of binaries that would have been detected given the timing of the observations and the measurement uncertainties, as estimated from the random sample of binaries generated in the previous step.

Finally, we added an additional constraint on the binary fraction to match the observed fraction of binaries. This is given by a binomial distribution:

$$\mathcal{L} = \prod_{\text{variable}} (f_{\text{bin}} f_{\text{det}}) \prod_{\text{not variable}} (1 - f_{\text{bin}} f_{\text{det}}), \quad (2.11)$$

where we multiplied the probability of detecting a radial velocity variability for all stars with radial velocity variability ( $\prod_{\text{variable}}(f_{\text{bin}} f_{\text{det}})$ ) and the probability for detecting no radial velocity variability for all apparently single stars ( $\prod_{\text{not variable}}(1 - f_{\text{bin}} f_{\text{det}})$ ).

Here we briefly summarize this approach to fitting multi-epoch radial velocity data. Before performing the fit, four preparatory steps should be taken:

1. Separate the observed stars into radial velocity variables and seemingly single stars based on whether the radial velocity over the multiple epochs is consistent with being constant (see equation 2.9).
2. Draw a random population ( $N \sim 10^5 - 10^6$ ) of binaries from the assumed period, mass ratio, and eccentricity distribution and with a random phase and orientation.
3. For every observed seemingly single star, select a subsample of the simulated binary population by removing all simulated binaries that would have been detected as a radial velocity variable given the time sampling and measurement uncertainty of that observed star. The fraction of radial velocity variables in the simulated population sets  $f_{\text{det}}$ , which can be used to compute the probability that the observed seemingly single star is still a binary ( $f'_{\text{bin}}$ ) with equation 2.10.

4. For every observed seemingly single star, compute the distribution of orbital velocities projected onto the line of sight for the pruned simulated binary population from step 3 to derive  $\text{pdf}_{\text{offset}}(v_i - v')$ .

We then used the distribution of radial velocity offsets due to binary orbital motions to compute the likelihood of the data being drawn from a given intrinsic velocity distribution (e.g. parameterized by the mean velocity and velocity dispersion) and binary fraction by following the steps below. These steps needed to be repeated for every evaluation of the likelihood as part of the maximization procedure and associated analysis of the parameter uncertainties (e.g. from a MCMC simulation).

5. For every observed seemingly single star, use the distribution from step 4, the probability of the star being a binary  $f'_{\text{bin}}$  from step 3, and an assumed underlying velocity distribution to compute the likelihood of reproducing the observed radial velocity of that star using equation 2.1.
6. Compute the total likelihood to reproduce the observed velocity distribution of seemingly single stars by multiplying the likelihoods to observe the radial velocities for all the observed seemingly single stars (or adding the log-likelihood).
7. Finally, multiply this likelihood from step 6 with the likelihood of detecting the observed fraction of radial velocity variables from equation 2.11 using the  $f_{\text{det}}$  from step 3.

When only a single epoch of radial velocity data is available, steps 3-4 simplify to computing equation 2.4 for the binary population from step 2. As in this case no radial velocity variables can be detected ( $f_{\text{det}} = 0$ ), the probability of a star to be a binary becomes the binary fraction (i.e.  $f'_{\text{bin}} = f_{\text{bin}}$ ) and the likelihood from equation 2.11 will be equal to one for any binary fraction.

A possible extension of this procedure would be to perform a Bayesian analysis and allow the parameterization of the period, mass ratio, and eccentricity distributions to vary within the uncertainties set by previous observations. Although this would in principle accurately deal with the effect on the fitted velocity dispersion of the uncertainties in the binary orbital parameter distributions, it would require recomputing the preparatory steps 1-4 for every step in the optimization and subsequent MCMC simulation. Unfortunately, this is currently prohibitively slow, especially when multi-epoch data are considered.

### 2.3.2 OB binary properties

Below we focus on the orbital parameter distributions of short-period close binaries, that is those with the largest orbital velocities, the strongest impact on the fitted line of sight

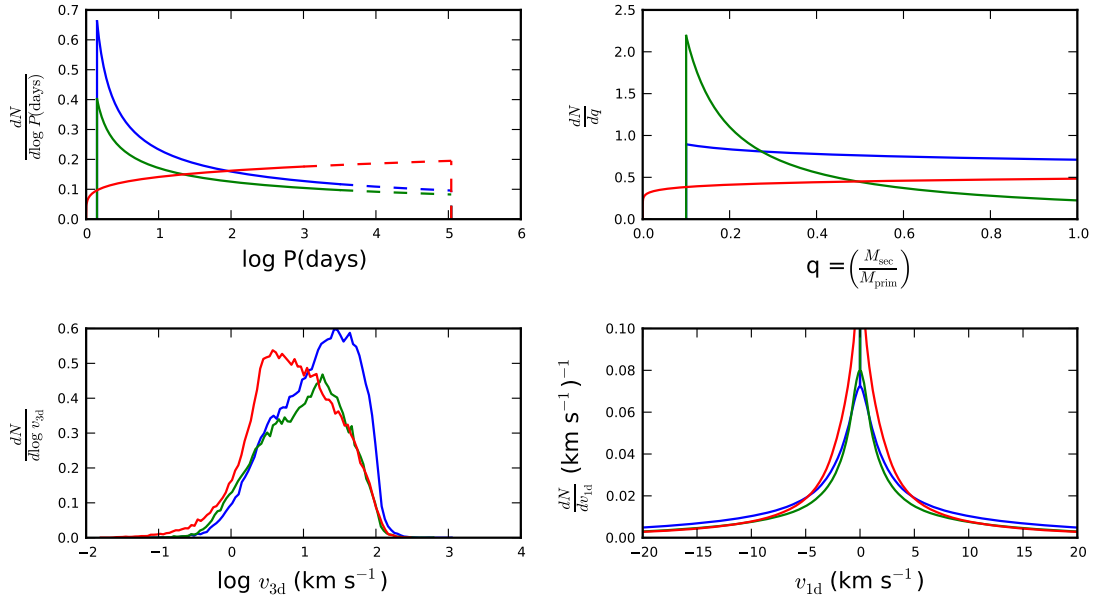


Fig. 2.7 — Assumed period distribution (upper left) and mass ratio distribution (upper right), as well as the unprojected logarithmic velocity distribution (lower left) and the projected velocity distribution (lower right). The extrapolation of the period distribution from the observed range to an upper limit of 300 years is plotted as a dashed line. This extrapolation has been taken into account in the lower panels that show the velocity distributions. The blue lines show the distributions from Sana et al. (2012), the green lines those from Sana et al. (2013), and the red lines the distributions from Kiminki & Koblunicky (2012), as detailed in Table 2.1.

velocity dispersion, and that are probed efficiently by Doppler shifts of spectral lines. There is now ample evidence that massive stars are preferentially found in binary systems, in particular in these close spectroscopic binary systems.

Unfortunately, the orbital parameter distributions of these binaries are still relatively poorly constrained, despite their fundamental importance to star formation, stellar evolution, and the early dynamical evolution of massive star clusters. Even when studies of massive binaries include a relatively large number of systems (e.g. Garmany et al. 1980; Mason et al. 2009), often only a small fraction of the identified binaries have well-constrained orbital properties (see Sana & Evans 2011). A few recent studies, which we discuss below, have achieved a better completeness in characterizing the identified binaries, in addition to correcting for observational biases in a more systematic way through Monte Carlo simulations (e.g. to translate the observed binary fraction into an intrinsic binary fraction).

Koblunicky & Fryer (2007) attempted to constrain the distributions of orbital paramete-

ters of massive binaries by using a sample of 900 radial velocity measurements of 32 O-type and 88 B-type stars in the Cyg OB2 association and comparing the raw velocities with the expectations of Monte Carlo simulations. They were forced to make several simplifying assumptions about the orbital parameter distributions however. Building upon this work and taking advantage of an extended dataset, Kiminki & Kobulnicky (2012) used 12 years of spectroscopic observations of 114 massive stars (B3–O5 primary stars) in Cyg OB2 and modeled the observed mass ratio, orbital period, and eccentricity distributions composed of the well-constrained orbital properties of 24 known binaries in the association (22 of which have periods shorter than 30 days).

Sana et al. (2013) analyzed the multiplicity properties of the O-type star population of 30 Doradus through multi-epoch spectroscopy obtained as part of the VLT-FLAMES Tarantula Survey. With 360 O-type stars surveyed, this is the largest homogeneous sample of massive stars analyzed to date. However, given the limited number of epochs obtained (typically six), the orbital parameters could not be determined for individual binary systems. The intrinsic binary fraction and period and mass ratio distributions in this case were therefore constrained using Monte Carlo simulations to simultaneously reproduce the observed binary fraction, the distribution of the amplitudes of radial velocity variations, and the distribution of the timescales of these variations.

Sana et al. (2012) homogeneously analyzed the O-type star population of six nearby Galactic open clusters and simultaneously fitted all the relevant intrinsic multiplicity properties. The larger average number of epochs allowed for a more complete binary detection than in other studies. Over 75% of the 40 binaries identified in this sample have measured orbital properties, which also made it possible for the authors to directly model and fit the orbital parameter distributions.

The distributions of binary orbital parameters from the three main studies discussed above are illustrated in Figure 2.7 and summarized in Table 2.1 along with the intrinsic spectroscopic binary fractions. The domains for which the period, mass ratio, and eccentricity have been considered and to which the quoted intrinsic binary fractions apply are also listed. These studies used power laws to describe the probability density functions of orbital periods (in  $\log_{10}$  space), mass ratios and eccentricities with exponents  $\pi$ ,  $\kappa$ , and  $\eta$ , respectively. In the following sections, we explore how sensitive the fitted velocity dispersion and binary fraction are to the adopted binary orbital parameter distribution by considering the differences between these orbital parameter distributions (which are consistent with each other at the two-sigma level).

We focus on the binary properties from the three papers listed in Table 2.1 because these studies are based on large samples and corrected for observational biases in a systematic way through Monte Carlo simulations. In contrast to some other studies, they also have the advantage that they do not a priori assume a fixed distribution for the periods or mass ratios (apart from assuming a power-law functional form). Moreover, they sample different combinations of period and mass ratio distributions, cover a relatively wide range of values of  $\pi$  and  $\kappa$ , and together are therefore representative of the current uncertainties on the

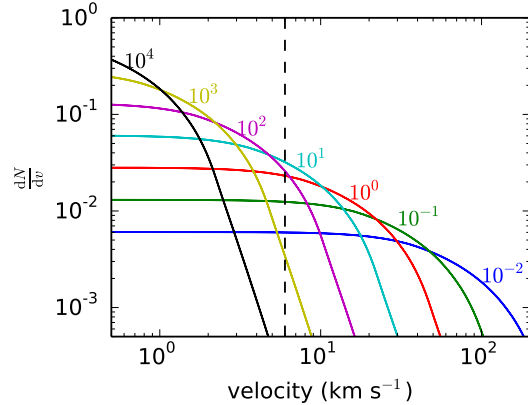


Fig. 2.8 — Probability distribution ( $\frac{dN}{dv}$ ) for the radial velocity difference between the primary star in a binary and its center of mass. Every line represents a binary with a fixed period and primary mass of  $20 M_{\odot}$ , but random mass ratios, eccentricities, and phases drawn from flat distributions as well as a random orientation. The periods increase by factors of 10 and are labeled in the figure in units of years. The vertical dashed line marks the intrinsic velocity dispersion within 10 pc of R136 ( $\sim 6 \text{ km s}^{-1}$ ; Hénault-Brunet et al. 2012a).

binary properties of massive stars. These studies also each sample a different environment in terms of cluster mass and density. The clusters considered by Sana et al. (2012) have relatively low masses ( $1\,000 - 5\,000 M_{\odot}$ ), and it is currently unknown whether the binary fraction and orbital parameter distributions are affected in the more energetic environment around a  $\sim 10^5 M_{\odot}$  cluster like the 30 Doradus region, where the stars in the sample of Sana et al. (2013) are located. Thus, while we may not expect all the scenarios presented in Table 2.1 to be applicable to the young massive cluster R136, it is interesting to test how the maximum-likelihood method behaves under different assumptions about the binary properties.

In the studies discussed above, only binaries with a period of up to  $\sim 10$  years could be detected due to the limited baselines of the observations. However, wider binaries still cause velocity offsets comparable to or larger than the velocity dispersion and hence significantly alter the observed velocity distribution. Figure 2.8 illustrates that large velocity offsets are likely to be caused by close binaries and small velocity offsets are more likely to be caused by wider binaries, as expected. Velocity offsets comparable to the velocity dispersion of R136 ( $\sim 6 \text{ km s}^{-1}$ , Hénault-Brunet et al. 2012a, see also section 2.3.4) are caused by binaries with periods between  $\sim 1$  and  $\sim 100$  years, thus extending beyond the period range covered by spectroscopic surveys. To account for all the relevant binaries in our fits of the R136 data, we extrapolated the orbital period distribution to an upper limit of 300 years. We also increased the binary fraction to match the intrinsic binary fraction determined over the period range covered by the observations (last row in Table 2.1).

### 2.3.3 Monte Carlo simulations

#### 2.3.3.1 Data generation

We used Monte Carlo simulations to

1. show the self-consistency of the method (i.e. ensure that it gives the correct result within the statistical uncertainties if all assumptions are met),
2. determine how the accuracy is limited due to the uncertainties on the orbital parameter distributions of massive binaries (see section 2.3.2),
3. and determine how the precision is limited due to small-number statistics.

In these simulations, we created a mock dataset of radial velocities through a two-step procedure. First, we assigned every star a systemic radial velocity from a Gaussian distribution with given mean velocity and intrinsic velocity dispersion. Then we assigned an additional velocity representing the effect of the binary orbital motions to a subset of these stars (where the probability to be a binary is set by the binary fraction). These additional velocities were computed using binary orbital parameters randomly drawn from one of the period, mass ratio, and eccentricity distributions listed in Table 2.1. In all cases we used the extrapolated period distribution out to 300 years and the corresponding binary fraction (last row in Table 2.1). In these simulations, we did not consider the effect that measurement uncertainties or a non-Gaussian velocity distribution have on the best-fit parameters. The provided python code can be used to generate these radial velocity distributions and reproduce the Monte Carlo experiments performed in this chapter.

These mock radial velocity datasets were fitted using our maximum-likelihood procedure, assuming one of the three sets of binary orbital parameter distributions listed in Table 2.1. This was either the same set of orbital parameter distributions used to generate the data, allowing to test for self-consistency and constrain the precision of the method (goals 1 and 3 above), or a different set of orbital parameter distributions, allowing to test the accuracy of the procedure when the orbital parameter distributions in the cluster do not match those assumed (goal 2 above). We repeated these experiments for various sample sizes and intrinsic velocity distributions in the cluster.

In addition to these single-epoch Monte Carlo simulations, we ran a number of simulations where two epochs of radial velocity data were sampled for every star. The radial velocity of the second epoch was generated by increasing the phase of the binary orbit with the ratio of the observational baseline  $b$  and the binary period  $P$  and recomputing the radial velocity offset from the center of mass. The systematic center-of-mass velocity of the binary was kept constant.

Although in the single-epoch case we could safely ignore the measurement uncertainty (as long because it is sufficiently lower than the velocity dispersion such that it has a negligi-



ble effect on the observed velocity distribution<sup>2</sup>), in the multi-epoch case the measurement uncertainty is crucial as it determines whether a specific binary can be spectroscopically detected. Thus, in this case, we added an additional (Gaussian) measurement uncertainty to every observation. For simplicity we adopted the same measurement uncertainty for all stars and epochs.

### 2.3.3.2 Results

The uncertainties in the orbital parameter distributions of OB stars, encapsulated by the differences in the sets of distributions we considered, induces systematic offsets in the fitted velocity dispersion (and binary fraction) when an assumption about the underlying binary properties is made to fit the observed velocity distribution. We first considered this systematic offset in the velocity dispersion for single-epoch data and then considered how it changes for multi-epoch data. Figure 2.9 shows the systematic offset in the fitted velocity dispersion induced when we fit the randomly generated radial velocity datasets assuming each of the sets of binary orbital parameter distributions listed in Table 2.1.

In Figure 2.9, we marked with a cross the simulations for which we found a best-fit binary fraction of 100%. Such a high best-fit binary fraction indicates that there are more high-velocity outliers in the dataset than can be explained by the assumed binary orbital parameter distributions. These high-velocity outliers could have many causes in real datasets, such as ejected stars, contaminating field stars, or poor radial velocity measurements. For the top panel of Figure 2.9, the radial velocity datasets were generated using the binary properties from Sana et al. (2012), which includes a relatively large proportion of close and similar-mass binaries. This leads to many high-velocity outliers in these datasets, which cannot be matched by the other orbital parameter distributions considered here (even for a binary fraction of 100%). This situation, where the assumed orbital parameter distributions cannot explain the large number of high-velocity outliers, will cause the fitted velocity dispersion to be systematically overestimated, because this reduces the number of outliers. Accordingly irrespective of the nature of the high-velocity outliers, when a binary fraction of 100% is found the fitted velocity dispersion will tend to be inflated and be unreliable. Therefore, below we only considered the cases where we found a best-fit binary fraction below 100%.

When we used the same orbital parameter distributions to fit the data as we used to generate the data, no systematic offset between the input and retrieved velocity dispersion were found (Figure 2.9). From this we conclude that the procedure is self-consistent (i.e. it yields the correct result if the assumptions made for the fit match the properties of the generated dataset). Significant systematic offsets were found when different orbital parameter distributions were used to generate the data than to fit the data. These systematic biases in the fitted velocity dispersion range from up to 60% for low input velocity disper-

---

<sup>2</sup>Even the case where the measurement uncertainty is too large for this approximation to be valid can be viewed as the measurement of a higher velocity dispersion  $\sigma_v'^2 = \sigma_v^2 + \sigma_{\text{meas}}^2$  with negligible measurement uncertainties, from which the (hopefully well-defined) measurement uncertainties are later subtracted.

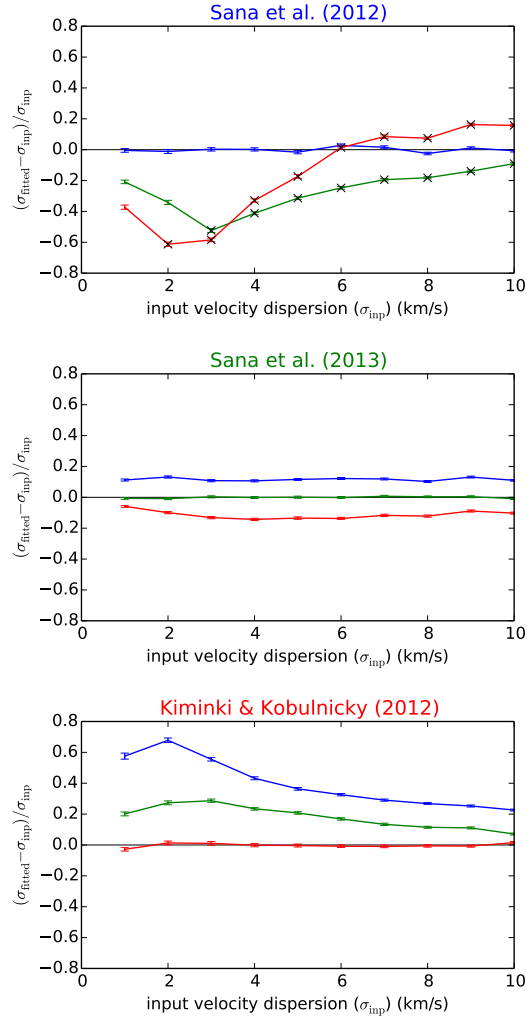


Fig. 2.9 — Systematic offset between the best-fit velocity dispersion ( $\sigma_{\text{fitted}}$ ) and the input velocity dispersion ( $\sigma_{\text{inp}}$ ) relative to the input velocity dispersion due to the uncertainties in the orbital parameter distributions of OB stars for a single epoch of radial velocity data. From top to bottom we have generated the radial velocity data using the orbital parameter distributions from Sana et al. (2012), Sana et al. (2013), and Kiminki & Kobulnicky (2012). The colors of the lines indicate the set of orbital parameter distributions assumed for the fit: blue line for Sana et al. (2012); green line for Sana et al. (2013); red line for Kiminki & Kobulnicky (2012). The error bars represent the uncertainty on the systematic offset after  $\sim 30$  Monte Carlo simulations, each of which included a sample of 2000 radial velocities. The simulations for which we find a best-fit binary fraction of 100% in the majority of cases are marked with a black cross.

sions ( $\sim 2 \text{ km s}^{-1}$ ) to as low as 25% for velocity dispersions of  $10 \text{ km s}^{-1}$  (Figure 2.9) for the sets of orbital parameter distributions under study here. This suggests that without precise knowledge of the binary properties of massive stars in a given environment, we

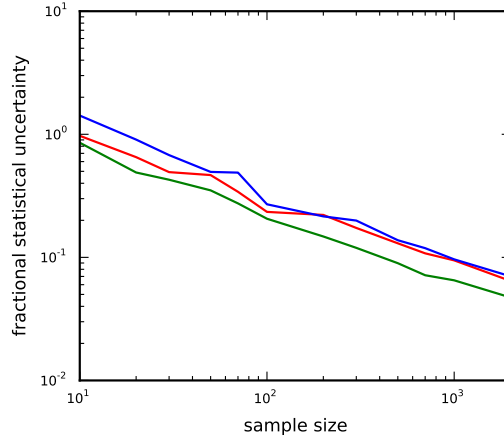


Fig. 2.10 — One-sigma statistical uncertainties due to small-number statistics in the fitted velocity dispersion as a function of the sample size  $N$  for single-epoch observations of a cluster with a velocity dispersion of  $5 \text{ km s}^{-1}$ . The colors indicate the set of orbital parameter distributions used to generate the data and assumed for the fit: blue line for Sana et al. (2012); green line for Sana et al. (2013); red line for Kiminki & Kobulnicky (2012). The color-coding is the same as in Figure 2.9. The statistical uncertainties are given relative to the input velocity dispersion of  $5 \text{ km s}^{-1}$ . Every point in this graph represents the average statistical uncertainty (as measured by the MCMC) in 60 Monte Carlo simulations, except for sample sizes smaller than or equal to 30, where 200 Monte Carlo simulations were averaged.

are limited to an accuracy of tens of percent when determining the line of sight velocity dispersion using a single epoch of radial velocities from OB stars. Most OB stars will form in massive clusters, whose virial velocity dispersion is generally expected to be higher than  $4 \text{ km s}^{-1}$ . In this range the velocity dispersion can be fitted to an accuracy better than  $\sim 40\%$ , which allows a cluster in virial equilibrium to be just barely distinguished from an unbound cluster from a single epoch of data.

If it is larger than the statistical uncertainties due to small-number statistics, this systematic offset of  $\sim 40\%$  will limit the accuracy on the velocity dispersion. Figure 2.10 shows how the statistical uncertainties of the fitted velocity dispersion depends on the sample size. From this figure we find that a  $2\sigma$  statistical uncertainty of  $\sim 40\%$  is reached for a sample size of  $\sim 100$  stars (for a cluster with a velocity dispersion of  $5 \text{ km s}^{-1}$ ). For a larger sample size the systematic offset due to the loosely constrained binary orbital parameter distributions will dominate the uncertainty on the velocity dispersion.

One option to decrease the systematic offset in the fitted velocity dispersion is to detect the spectroscopic binaries that alter the observed velocity distribution. This requires multiple epochs of data. The largest systematic offset was found when radial velocity data generated using the binary orbital parameter distributions from Kiminki & Kobulnicky

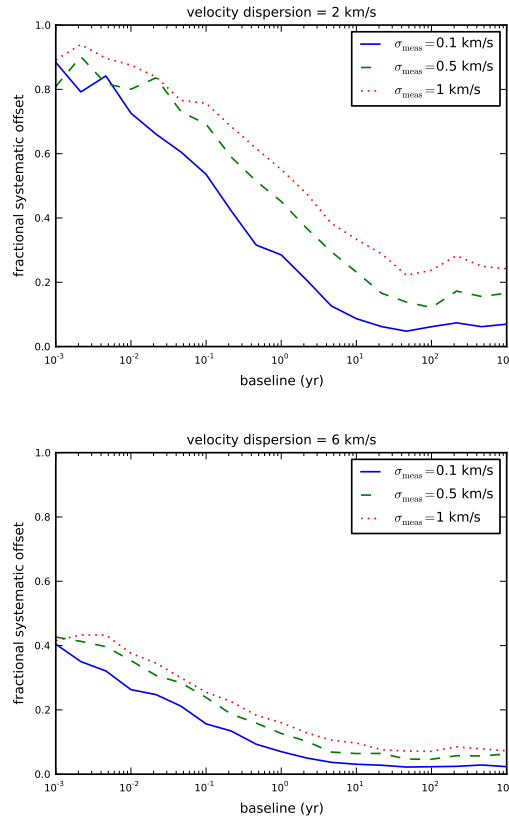


Fig. 2.11 — Systematic offset in the fitted velocity dispersion for radial velocity data generated using the Kiminki & Kobulnicky (2012) binary orbital parameter distribution and fitted assuming the Sana et al. (2012) binary orbital parameter distribution, plotted against the baseline between two epochs of observations. As the baseline between the two epochs of observations increases, more spectroscopic binaries are detected, leading to a decrease in the systematic offset of the velocity dispersion. We show the results from Monte Carlo simulations for clusters with a velocity dispersion of  $2 \text{ km s}^{-1}$  (upper panel) and  $6 \text{ km s}^{-1}$  (lower panel), as well as for measurement uncertainties of  $0.1 \text{ km s}^{-1}$  (solid),  $0.5 \text{ km s}^{-1}$  (dashed), and  $1 \text{ km s}^{-1}$  (dotted).

(2012) was fitted using the distributions from Sana et al. (2012) (blue line in the lower panel of Figure 2.9). For this specific case, we explored whether the systematic offset in the fitted velocity dispersion could be resolved by using two epochs of radial velocity data. The results of these Monte Carlo simulations are shown in Figures 2.11 and 2.12 for clusters with a velocity dispersion of  $2 \text{ km s}^{-1}$  and  $6 \text{ km s}^{-1}$ , for measurement uncertainties  $\sigma_{\text{meas}}$  of  $0.1$ ,  $0.5$ , and  $1 \text{ km s}^{-1}$  and a broad range of baselines between a few hours and hundreds of years.

A larger fraction of the spectroscopic binaries can be detected when the baseline is longer or the measurement uncertainties are smaller. As expected, this leads to a smaller

systematic offset in the fitted velocity dispersion. From Figure 2.12 we find that for a broad range of intermediate baselines the systematic offset decreases linearly with  $\log(\sigma_{\text{meas}}/b)$ , such that the systematic offset decreases by the same amount for every doubling of the baseline or halving of the measurement uncertainties. The size of the offset and the rate of decline depend on the exact binary properties assumed to compute the offset. This relation breaks down both for low  $\sigma_{\text{meas}}/b$ , when only very close binaries can be identified (whose large velocity offsets already marked them as binaries in single-epoch data), and for high baselines  $b$ , when the baseline becomes comparable to the period of the widest binaries that have a significant radial velocity offset.

In section 2.3.6, we analyze these relations in more detail. Here we note that for the typical measurement uncertainties of  $4 \text{ km s}^{-1}$  and the total baseline of one year of the radial velocity observations in R136, we obtain  $\sigma_{\text{meas}}/b \approx 4 \text{ km s}^{-1} \text{ yr}^{-1}$ . Accordingly from these Monte Carlo simulations we expect a significant systematic offset in the fitted velocity dispersion of  $\sim 40\%$  depending on the adopted binary orbital parameter distribution when analyzing a single epoch of the R136 radial velocity data. This systematic offset should be significantly reduced to  $\sim 20\%$  when considering the full baseline of one year of the radial velocity observations (see lower panel of Figure 2.12 for  $\sigma_{\text{meas}}/b \approx 4 \text{ km s}^{-1} \text{ yr}^{-1}$ ).

## 2.3.4 R136

### 2.3.4.1 Data

The dataset we used to test the maximum-likelihood method outlined in section 2.3.1 consists of multiple epochs (at least five) of radial velocity measurements for 81 O-type systems in the inner 10 pc (in projection) of R136, all obtained with the FLAMES instrument on the VLT as part of the VLT-FLAMES Tarantula Survey (VFTS). These 81 systems include both apparently single stars and objects showing radial velocity variability. Most of the stars in the inner 5 pc have been observed with the ARGUS integral-field unit coupled to the Giraffe spectrograph, while for the vast majority of stars between 5 pc and 10 pc the Medusa fiber-feed to Giraffe has been used (for more details on the VFTS data, see Evans et al. 2011). In both cases, the radial velocities were measured by fitting Gaussians to helium absorption lines using a similar approach and the same rest wavelengths (Hénault-Brunet et al. 2012a; Sana et al. 2013). This sample of 81 objects excludes the B-type and emission-line stars observed by the VFTS in the inner 10 pc of R136, but it includes a few supergiants (or supergiant candidates) for which the absolute radial velocities might be inaccurate because of the effect of stellar winds on the line profiles. However these were shown to have a negligible impact on the measured velocity dispersion of the apparently single stars of the sample (see Hénault-Brunet et al. 2012a). The radial velocity measurements for individual epochs are listed in Hénault-Brunet et al. (2012a) and Sana et al. (2013). The median radial velocity uncertainty of the single-epoch measurements for the objects of our sample is  $\sim 4 \text{ km s}^{-1}$ . Note that we did not include stars observed by the VFTS farther out than 10 pc to limit possible contamination from nearby clusters or other

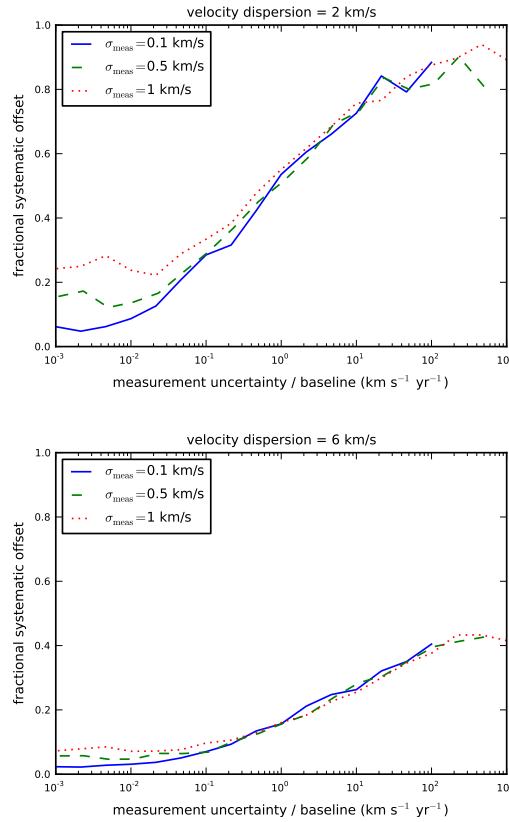


Fig. 2.12 — Same as Figure 2.11, but with measurement uncertainty over the baseline ( $\sigma_{\text{meas}}/b$ ), rather than the baseline on the x-axis. Note that for a broad region of intermediate baselines, all the curves overlap.

star formation events in the surroundings of R136.

Mackey & Gilmore (2003) found that the light profile of R136 is best fitted with a double-component EFF profile (Elson et al. 1987), suggesting that the cluster is superimposed on an OB association, that contributes a significant fraction of its total integrated light (Maíz-Apellániz 2001). In this double-component EFF fit, the projected radius within which the two components contribute equally is at about 5 pc, as illustrated in Figure 2.13 (top panel). To decide whether the velocity distributions of these two potentially distinct components should be considered separately, we also show in Figure 2.13 (bottom panel) the velocity distribution of the stars more likely to be part of the inner component (i.e. the cluster) compared to the velocity distribution of the stars more likely to be part of the outer component (i.e. the OB association). We see no evidence for a difference in the velocity distribution between the two components. Similarly, Hénault-Brunet et al. (2012a) found the measured velocity dispersion profile to be relatively flat between 1 and

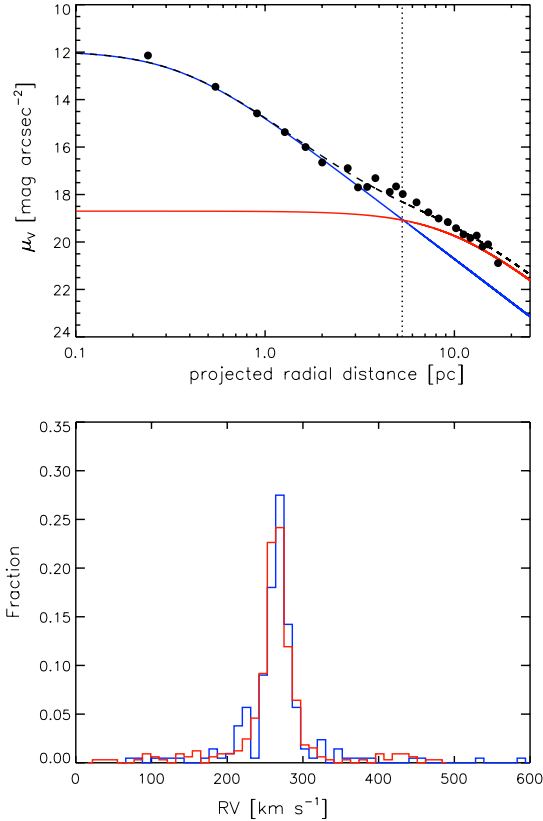


Fig. 2.13 — *Top*: Two-component EFF fit to the surface brightness profile of R136 as in Mackey & Gilmore (2003). The data points shown are Mackey and Gilmore’s recalibrated surface brightnesses from McLaughlin & van der Marel (2005). Stars that are farther out than  $\sim 5$  pc (marked by the dotted line) from the cluster center are more likely to be part of the OB association. Within this radius stars are more likely to belong to the R136 cluster itself. *Bottom*: Normalized histograms showing the velocity distribution of the 32 stars within 5 pc in blue (211 velocities), and the 49 stars between 5 and 10 pc in red (327 velocities).

10 pc from the center of R136<sup>3</sup>. Because the two components appear to be indistinguishable (at least kinematically) in the inner 10 pc, we conclude that it is justified to try to fit a single velocity dispersion for all the stars of our sample.

Note that Sabbi et al. (2012) found a dual structure in the density of low-mass stars in R136, hinting at a merger event between the main core of R136 and a second cluster. Because only a very small fraction our targets are expected to be associated with this second clump, we treated all the stars within 10 pc as one population.

<sup>3</sup>Even though only the inner  $\sim 5 - 6$  pc are more than a dynamical time old and can be considered to be bound, and thus strictly speaking as part of the cluster according to the definition of Gieles & Portegies Zwart (2011).

### 2.3.4.2 Results

Hénault-Brunet et al. (2012a) determined a velocity dispersion of  $\sim 6 \text{ km s}^{-1}$  for the O-type stars within 10 pc in projection from the center of R136<sup>4</sup> after selecting out identified binaries and estimating the effect of undetected binaries. To test our procedure, we fit single-epoch radial velocity datasets extracted from the full multi-epoch dataset presented in section 2.3.4.1. One such fit is shown in Figure 2.14.

We extracted five single-epoch radial velocity datasets without any overlap because every star in the sample was observed for at least five epochs. These datasets are not independent, because they all include observations of the same stars, albeit at different epochs.

The best-fit binary fraction, velocity dispersion and mean velocity for each of these five datasets are shown at the left side of each panel in Figure 2.15. The three different colors again represent the three sets of orbital parameter distributions assumed. The  $1\sigma$  error bars are somewhat larger than predicted from the Monte Carlo simulations for a sample of 81 radial velocities (see Figure 2.10), because the effective sample size is smaller than 81. A significant subset of the observed radial velocities in R136 have a measurement uncertainty comparable to or larger than the velocity dispersion. These radial velocities

<sup>4</sup>The velocity dispersion was slightly lower ( $\sim 5 \text{ km s}^{-1}$ ) when we only considered the stars within 5 pc from the center. We ignored the small potential contribution ( $\sim 0.5 \text{ km s}^{-1}$ ) to the velocity dispersion from cluster rotation (Hénault-Brunet et al. 2012b).

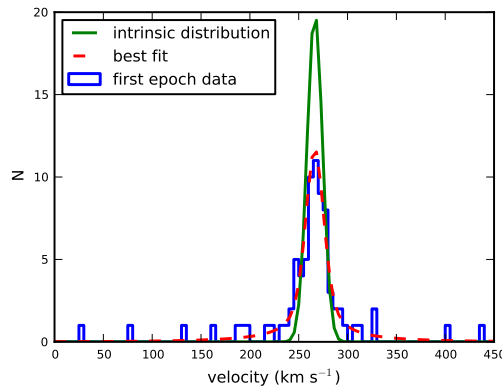


Fig. 2.14 — *Blue line*: The observed radial velocity distribution for a single epoch drawn from the multi-epoch radial velocity dataset of R136 (Hénault-Brunet et al. 2012a; Sana et al. 2013, see section 2.3.4.1 for details). *Red dashed line*: the best-fit radial velocity distribution, including the effect of the orbital motions of spectroscopic binaries. *Green line*: The intrinsic velocity distribution of the cluster, corrected for the orbital motions of binaries. This intrinsic distribution is assumed to be a Gaussian whose width and mean have been optimized to fit the data (see section 2.3.1).



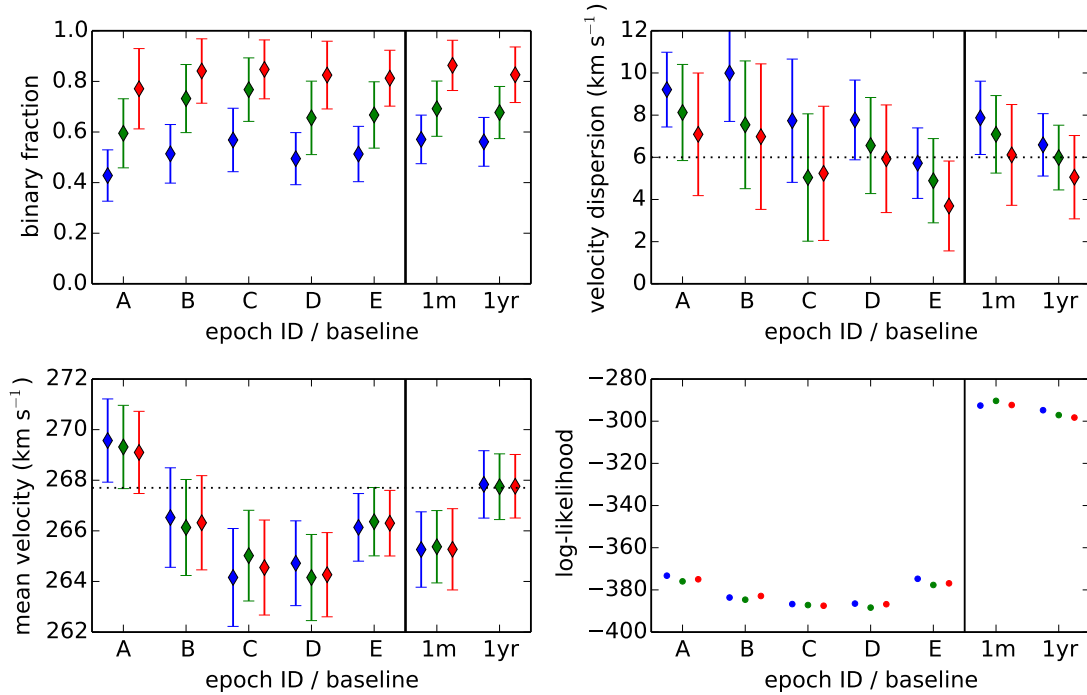


Fig. 2.15 — Best-fit binary fraction, velocity dispersion, and mean velocity and the log-likelihood of the best fit for five single-epoch radial velocity datasets (labeled A-E) of the O-type stars in R136, and two datasets with two epochs with a baseline of roughly one month and one year. The colors indicate the set of orbital parameter distributions assumed in the fit: blue line from Sana et al. (2012); green line from Sana et al. (2013); and red line from Kiminki & Kobulnicky (2012). The error bars show the  $1\sigma$  uncertainties on the best-fit values, estimated with MCMC simulations. The dashed lines in the upper-right and lower-left panels show the values found after removing the spectroscopic binaries identified from the full multi-epoch dataset (Hénault-Brunet et al. 2012a).

provide (nearly) no information about the velocity dispersion of the clusters, leading to a smaller effective sample size.

We found lower binary fractions for the orbital parameter distributions where an individual binary has a higher likelihood of causing a significant radial velocity offset. This explains the low binary fraction found for the parameters from Sana et al. (2012, blue in Figure 2.15), which has relatively many close and similar-mass binaries (see Table 2.1 and Figure 2.7). In contrast, the best-fit mass-ratio distribution of Sana et al. (2013) has more low-mass binary companions, while the period distribution favored by Kiminki & Kobulnicky (2012) has a larger proportion of wide binaries and hence requires a larger binary fraction to reproduce the same number of high-velocity outliers.

The fitted velocity dispersion is less sensitive to the exact parameters assumed than the binary fraction, although we did still find variations of  $\sim 3 \text{ km s}^{-1}$  (see central panel in Figure 2.15) for the single-epoch fits, which is comparable to the  $\sim 40\%$  systematic offset found from Monte Carlo simulations (section 2.3.3). The intrinsic velocity dispersion of R136 fitted from single-epoch radial velocities is consistent with the  $6 \text{ km s}^{-1}$  from the multi-epoch approach (Hénault-Brunet et al. 2012a).

Finally, the best-fit mean velocity is barely sensitive to the assumed orbital parameter distributions (see Figure 2.15), because as long as the projections of the binaries on the sky are random, the velocities from the binary orbital motions will be symmetrically distributed around the mean velocity. This means that the systematic uncertainties induced from an assumed binary population do not significantly affect the measurements of the mean velocity, which in turn means that parameters depending on the mean velocity (e.g. cluster rotation) can be accurately fitted.

The best-fit parameters obtained when using two epochs of data are shown at the right side of each panel of Figure 2.15. As we saw from the Monte Carlo simulations of section 2.3.3, the systematic offset in the fitted velocity dispersion induced when different binary orbital parameter distributions are used decreases significantly with multi-epoch data. For the single-epoch data, we found typical variations in the fitted velocity dispersion of  $\sim 3 \text{ km s}^{-1}$ , which decreases to only  $\sim 2 \text{ km s}^{-1}$  when using two epochs that are approximately one month apart. For a baseline of one year, the systematic offset decreases even more to about  $1 \text{ km s}^{-1}$ .

Although the fitted velocity dispersions show smaller systematic offsets between the adopted binary orbital parameter distributions when multi-epoch data are used, the fitted binary fraction is roughly the same for single- and multi-epoch data. This is consistent with a scenario where the fitted binary fraction depends on the proportion of close and similar-mass binaries. When assuming a high proportion of such systems, the fitted binary fraction will be lower, irrespective of whether these stars appear as high-velocity outliers (as in the single-epoch case) or as radial velocity variables (as in the multi-epoch case).

From inspecting the log-likelihood of the best-fit models for R136 (Figure 2.15), no set of orbital parameter distributions (Sana et al. 2012; Kiminki & Kobulnicky 2012; Sana et al. 2013) consistently fits the data better than the others. This does not imply that there is insufficient information in the dataset to distinguish between the orbital parameter distributions. After all, our method ignores some information (e.g. the observed distribution of radial velocity offsets between epochs) in the log-likelihood, which could have been used to constrain the binary orbital parameter distributions (e.g. Sana et al. 2013), but not the intrinsic velocity dispersion.

### 2.3.5 Discussion

We were able to fit the intrinsic velocity dispersion from a single epoch of radial velocity data with an accuracy ranging from  $\sim 60\%$  for a cluster velocity dispersion of  $\sim 2 \text{ km s}^{-1}$  to  $\sim 25\%$  for  $\sigma_v \sim 10 \text{ km s}^{-1}$ , given the present-day uncertainties on the orbital parameter distributions of OB spectroscopic binaries (e.g. Table 2.1 and Figure 2.7). For typical velocity dispersions of young massive clusters ( $\gtrsim 4 \text{ km s}^{-1}$ ) we found that an accuracy better than 40% can be reached, which is sufficient to distinguish a cluster in virial equilibrium from an unbound cluster. This systematic offset will dominate over the statistical uncertainties from small-number statistics for a sample size larger than about 100 stars. This means that after observing 100 stars for a single epoch, the accuracy of the fitted velocity dispersion will in principle no longer increase when more stars are observed due to the uncertainties in the binary orbital parameter distributions of OB stars. Observing the same stars for multiple epochs makes it possible to reduce the systematic offset. For example, a ratio of the measurement uncertainty over the baseline of  $1 \text{ km s}^{-1} \text{ yr}^{-1}$  is required to reduce the systematics below 15% for an intrinsic velocity dispersion of  $6 \text{ km s}^{-1}$ ,

To understand the systematic offsets, we directly compared the fits of the single-epoch R136 data for the orbital parameter distributions of Sana et al. (2012) and Kiminki & Kobulnicky (2012). In the case of Sana et al., the binaries typically orbit each other with tens of  $\text{km s}^{-1}$ , an order of magnitude larger than for Kiminki & Kobulnicky (Figure 2.7). Thus, an individual binary in the former case will have a much higher probability of causing a high-velocity outlier. To reproduce the high-velocity outliers in the R136 data we thus need a lower binary fraction for the binary orbital parameter distribution of Sana et al. (2012) than for Kiminki & Kobulnicky (2012), which explains the difference in the binary fraction found for the R136 data (left panel in Figure 2.15).

On the other hand, the fitted velocity dispersion is affected by the abundance of wider binaries with orbital velocities comparable to the intrinsic velocity dispersion of the cluster ( $\sim 6 \text{ km s}^{-1}$ ), because these binaries are more likely to really broaden the observed peak in the velocity distribution, instead of just creating a high-velocity tail. We can see in Figure 2.7 that these binaries are much more common for the orbital parameter distributions of Kiminki & Kobulnicky (2012) than for those of Sana et al. (2012), even before we take into account the fact that we find a lower overall binary fraction for Sana et al. (2012). This much higher fraction of wide binaries broadening the observed velocity distribution when assuming the binary orbital parameter distributions of Kiminki & Kobulnicky (2012) leads to a significantly lower fitted velocity dispersion (central panel in Figure 2.15) than in Sana et al. (2012). Still, it is remarkable that the systematic offset in the velocity dispersion is smaller than a factor of 2 given that the peaks in the orbital velocity distributions differ by an order of magnitude (see lower left panel in Figure 2.7).

Note that the differences between the sets of binary properties listed in Table 2.1 might be real to some extent (i.e. not only reflect uncertainties in our knowledge of these properties). There are reasons to assume that the binary properties of massive stars may depend on the environment and the age of the region in which they are located. For example, the

intrinsic fraction of O-type spectroscopic binaries seems lower in 30 Doradus than in the relatively low-density Galactic clusters (see Table 2.1), although the two results still agree within  $2\sigma$ . As discussed by Sana et al. (2013), this may suggest that the binary properties in the 30 Doradus region have already been significantly affected by dynamical and/or stellar evolution, which would induce merger events or binary disruption and decrease the observed number of binaries. This is to be expected given the presence of different populations in the region, some already quite old, and considering that a fraction of the O-star population consists of runaways. For the Galactic open cluster sample, cluster dynamics and stellar evolution are not expected to have significantly altered the orbital properties of the binaries (Sana et al. 2012). Given the young age of the clusters in this sample, the parameters reported in this case are probably a good representation of the properties of massive binaries at birth.

A wide variety of possible period, mass ratio, and eccentricity distributions for OB binaries have been considered in the literature. We chose to limit our analysis to the three sets of orbital parameter distributions in Table 2.1, which we felt were the most representative of our present-day knowledge about these distributions. However, we offer the provided python code<sup>5</sup> for use, which can be used to fit an observed radial velocity distribution, and to create and fit mock radial velocity distributions, using either the orbital parameter distributions described in this work or any other orbital parameter distributions. This code can thus be used to calculate the systematic offsets in the fitted velocity dispersion between any orbital parameter distributions (as in Figure 2.9) or to determine the accuracy with which the velocity dispersion can be fitted as a function of sample size when planning observations (as in Figure 2.10).

### 2.3.6 Effectiveness of multi-epoch radial velocities

Multi-epoch data are required to reduce the systematic offsets in the fitted velocity dispersion due to uncertainties in the adopted binary orbital parameter distributions. In particular, one needs to identify and remove from the sample the spectroscopic binaries with radial velocity offsets comparable to the intrinsic velocity dispersion. Binaries causing a larger velocity offset are easily identified in single-epoch data as high-velocity outliers and hence have little effect on the fitted velocity dispersion. Binaries causing a velocity offset smaller than the velocity dispersion have a negligible impact on the observed velocity distribution. Below, we therefore consider the properties of the critical binaries with velocity offsets similar to the intrinsic velocity dispersion, and we investigate under which conditions they can be identified as radial velocity variables in multi-epoch data.

For most of the binary orbit, the radial velocity offset is smaller but of the same order of magnitude as the radial velocity semi-amplitude  $K$ . This is illustrated in the central panel of Figure 2.16, where we plot the distribution of the radial velocity semi-amplitude over the velocity offset ( $K/v_{\text{off}}$ ) at a random point in time for a random set of binaries. The

<sup>5</sup><https://github.com/MichielCottaar/velbin>

distribution plotted here is independent of the period and mass ratio distribution and only depends on the eccentricity distribution. For both eccentricity distributions considered (flat and only circular), the distribution is strongly peaked at one and decreases quickly with increasing  $K/v_{\text{off}}$ . Only for eccentric orbits can the radial velocity offset exceed the semi-amplitude.

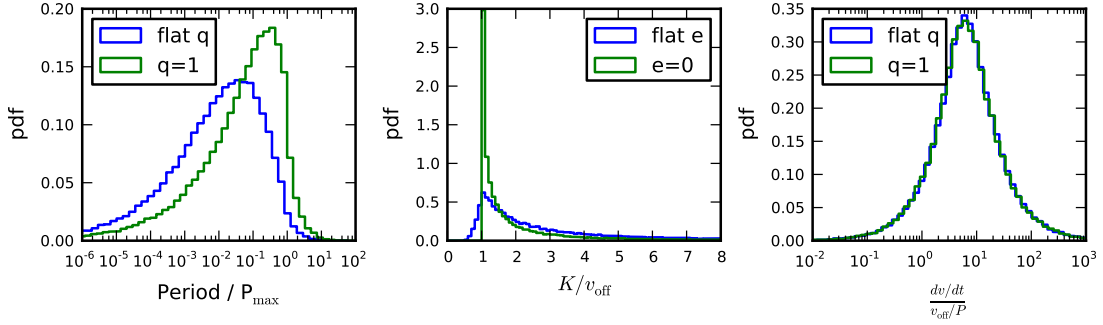


Fig. 2.16 — *Left:* the period distribution with respect to the longest period needed to obtain a given velocity offset for a circular orbit ( $P_{\text{max}}$ ; equation 2.12) for a flat distribution of mass ratios (blue) or only equal-mass binaries (green). *Middle:* the distribution of the radial velocity semi-amplitude ( $K$ ) relative to the velocity offset ( $v_{\text{off}}$ ) for a flat distribution of eccentricities and circular orbits. *Right:* the distribution of the velocity gradient ( $dv/dt$ ) relative to the velocity offset ( $v_{\text{off}}$ ) divided by the orbital period ( $P$ ) for a flat distribution of mass ratios (blue) or only equal-mass binaries (green). These plots are independent of the period distribution of the binaries, and only weakly depend on the mass ratio and eccentricity distributions.

If the time between radial velocity observations is sufficiently longer than the period of the binary, the phases of these observations become independent of each other. Radial velocities are drawn from a distribution set only by the radial velocity semi-amplitude  $K$  and eccentricity  $e$ , independent of the orbital period or mass ratio (except for their contribution to  $K$ ). To allow identification as a binary under this long-baseline condition, the measurement uncertainty should be at least smaller than the radial velocity semi-amplitude of the binaries. Thus, to identify the critical binaries with velocity offsets comparable to the intrinsic velocity dispersion, measurement uncertainties lower than the velocity dispersion are required. This is not really an additional requirement, because measurement uncertainties lower than the velocity dispersion help to accurately fit the velocity dispersion even when the effect of binaries is ignored. The detection rate of binaries will increase as the measurement uncertainties decrease or the number of epochs increases (by decreasing the probability that the observations are in phase with the binary orbit), but it does not depend on the baseline of the observations as long as it remains significantly longer than the period of the binary. This explains why, in our Monte Carlo simulations of the systematic offset of the fitted velocity dispersion for two-epoch data (Figure 2.11), the systematic velocity offset depends on the measurement uncertainty and not on the baseline once this baseline becomes comparable to the widest binaries in the

Monte Carlo simulations (i.e. 300 years).

For a reasonable baseline, there will be many binaries causing radial velocity offsets comparable to the intrinsic velocity dispersion with periods much longer than the baseline, in which case the argument above does not hold. To illustrate this, we computed from Kepler's third law the longest period needed to create a given velocity offset for circular orbits:

$$\begin{aligned}
 P_{\max} &= P(K = v_{\text{off}}, e = 0, \sin i = 1, q = 1) = \frac{1}{4} \frac{2\pi G m_1}{v_{\text{off}}^3} \\
 &= 2.6 \times 10^4 \text{ yr} \frac{m_1}{M_{\odot}} \left( \frac{v_{\text{off}}}{\text{km s}^{-1}} \right)^{-3}.
 \end{aligned} \tag{2.12}$$

Projection effects and unequal mass ratios will result in the typical period of the binary causing a given velocity offset to be lower. We found from randomly sampling a large number of binaries with a flat eccentricity distribution that even for equal-mass binaries the typical period is 0.5 dex shorter (green line in the left panel of Figure 2.16). For a flat mass ratio distribution (blue line in the left panel of Figure 2.16), the period distribution of stars that cause a given velocity offset is even 1.5 dex shorter than the longest period given in equation 2.12. The distributions plotted in Figure 2.16 are independent of the period distribution of binaries, because they are plotted relative to  $P_{\max}$ . For the R136 data ( $\sigma_v \sim 6 \text{ km s}^{-1}$ ;  $m_1 \sim 30 M_{\odot}$ ),  $P_{\max}$  is about 4000 years. Most of the binaries that cause a velocity offset comparable to the intrinsic velocity dispersion of the cluster will therefore have periods longer than a baseline of even a few years, although there is a significant minority of binaries with  $P < 10^{-3} P_{\max} < 4$  years (left panel in Figure 2.16) whose period may be shorter than the baseline.

Long-period binaries will be detected when the measurement uncertainty is significantly smaller than the velocity change between the first and last epoch<sup>6</sup>, which we assumed below to be separated in time by a baseline  $b$ . The velocity change is given by  $\frac{dv}{dt}b$ , where  $\frac{dv}{dt}$  is the velocity gradient of the binary, which is roughly constant over the observed time under the condition considered here ( $P \gg b$ ). Therefore the detection of a long-period binary depends on whether the velocity gradient is sufficiently steeper than the ratio of the measurement uncertainty and baseline ( $\sigma_{\text{meas}}/b$ ). In the two-epoch Monte Carlo simulations (Figures 2.11 and 2.12), we indeed find that the systematic offset in the fitted velocity dispersion mainly depends on  $\sigma_{\text{meas}}/b$  for baselines shorter than a few years. For these baselines, most of the binaries causing velocity offsets comparable to the intrinsic velocity dispersion are in the regime discussed here ( $P \gg b$ ). Because these binaries need to be detected to reduce the systematic offset, the systematic offset is to first order a function of  $\sigma_{\text{meas}}/b$  (see Figure 2.12), until the baseline becomes comparable to the widest binaries (with periods of  $\sim P_{\max}$ ).

<sup>6</sup>Intermediate epochs contribute less to the capability of observing shallow velocity gradients than the first and last epoch, suggesting that it is better to focus on just two deep epochs than on many less deep epochs with the same total baseline. However, intermediate epochs can still be important in confirming whether the velocity differences measured between the first and last epoch, are real and they are crucial in solving binary orbits, which allows the binary population to be characterized.

To quantify this further, we computed the velocity gradients for a large sample of binaries with flat eccentricity distributions. For binaries causing a given velocity offset  $v_{\text{off}}$  with orbital period  $P$ , we found that the velocity gradients follow a roughly log-normal distribution with a peak at  $8v_{\text{off}}/P$  and a width of about 0.5 dex (right panel in Figure 2.16). To detect the widest binaries causing a velocity offset comparable to the velocity distribution (i.e. with  $P \sim P_{\text{max}}$ ) in R136 ( $\sigma_v \sim 6\text{km s}^{-1}$ ;  $P_{\text{max}} \sim 4000$  years) would hence require the detection of a velocity gradient of  $8\sigma_v/P_{\text{max}} \approx 12 \text{ m s}^{-1} \text{ yr}^{-1}$ , which is virtually impossible. However, with typical periods being 0.5 - 3 dex shorter (left panel in Figure 2.16), a significant proportion of the critical binaries can actually be detected for the typical measurement uncertainty of  $1 \text{ km s}^{-1}$  and a baseline of one year. This explains the drop in the systematic offset between the velocity dispersion fitted assuming different binary orbital parameter distributions (which are represented by different colors in Figure 2.16) when multi-epoch data are used.

For many lower-mass clusters, the intrinsic velocity dispersion is much lower (often at the sub- $\text{km s}^{-1}$  level), leading to an increase in the longest period due to its dependence on the third power of the velocity offset (equation 2.12). Even though the light of these generally older clusters will be dominated by lower-mass stars (lowering  $m_1$  in equation 2.12),  $P_{\text{max}}$  is still likely to occur at roughly  $10^5 - 10^7$  years, such that the broadening of the velocity distribution is dominated by binaries with periods of  $10^3 - 10^5$  years. These are virtually impossible to detect by spectroscopic means (and will only be detectable in direct-imaging surveys for the most nearby clusters). Therefore, although a multi-epoch strategy with a baseline of a few years works well for the high velocity dispersions of young massive clusters, it has little effect on the accuracy with which clusters with a much lower velocity dispersion can be measured, because this would require the detection of binaries with periods of many thousands of years. This is quite fortunate because the need for a multi-epoch strategy is much lower for lower-mass clusters, whose light is dominated by solar-type stars with much better constrained binary properties.

## 2.4 Conclusions

We investigate here a maximum likelihood method to simultaneously fit an intrinsic velocity distribution with the velocity offsets induced due to binary orbital motions to a single epoch of observed radial velocities. The procedure was pioneered separately by Odenkirchen et al. (2002), Kley et al. (2002), and Martinez et al. (2011). It enables a proper treatment of the effect of binary orbital motions on the radial velocities observed in surveys of single-epoch high-resolution spectra.

This procedure requires assumptions about the period, mass ratio, and eccentricity distribution for the binaries in the observed stars, although we show that reasonable uncertainties in the assumed binary properties do not significantly affect the intrinsic velocity distribution we find (sections 2.2.3.2).

Assuming a binary period, mass ratio, and eccentricity distribution found for solar-type stars in the field (Raghavan et al. 2010) the precision with which the binary fraction, velocity dispersion, and mean velocity can be measured as a function of the number of observed stars, the velocity dispersion, and the binary fraction can be determined using equations 2.7a - 2.7c and Figure 2.3. These results can be used to get a prior estimate of the number of stars that should be observed to reach a given accuracy. Although we calculate the accuracy with which the velocity dispersion can be measured, we emphasize that the procedure can be trivially expanded to test complicated dynamical models, where for example the velocity dispersion and the mean velocity depend on the position of the observed star in the cluster and/or its mass.

As a test case we apply this procedure to three different sets of single epoch radial velocity data from 1108 stars in NGC 188 (Geller et al. 2009). Assuming the period, mass ratio, and eccentricity distribution from the field solar-type stars we are able to reproduce the velocity dispersion of  $\sim 0.5 \text{ km s}^{-1}$  for a single epoch of data, consistent with the value Geller & Mathieu (2011) derived from many epochs of radial velocity data, even though about half of the observed stars are fore- and background stars.

For an assumed binary period, mass ratio, and eccentricity distribution this maximum likelihood procedure can be used to characterize the intrinsic velocity distribution for any set of observed radial velocities, where the observed distribution has been significantly broadened by binary orbital motions. This will happen in almost any clusters where the velocity dispersion is lower than several  $\text{km s}^{-1}$  such as open clusters, faint Milky Way companion dwarf galaxies, young massive clusters, local star-forming regions, and some low-mass globular clusters. Determining the intrinsic velocity distribution will allow us to constrain the dynamical state of these clusters from a single epoch of radial velocity data, which gives a useful test on our understanding of the current state and evolution of these type of clusters.

We explored the applicability of this procedure to recover the intrinsic velocity dispersion of massive stars in young clusters from a single epoch of radial velocity data. By using Monte Carlo simulations and multi-epoch stellar radial velocity data of the young massive cluster R136 as a test case, we showed that the method works reasonably well, the main limitation being uncertainties in the binary properties of OB stars which can lead to a systematic offset of tens of percent in the fitted velocity dispersion ( $< 40\%$  for typical young massive cluster velocity dispersions, i.e.  $\gtrsim 4 \text{ km s}^{-1}$ ).

This systematic offset can be greatly reduced by directly detecting the spectroscopic binaries through radial velocity variations in multi-epoch data. Specifically, the spectroscopic binaries with velocity offsets comparable to the intrinsic velocity dispersion need to be detected to increase the accuracy of the fitted velocity dispersion. For a typical young massive cluster, these periods range from  $10^{-2}$  to  $10^4$  years, meaning that many can be detected with typical baselines of observations of a few years. Indeed, we found that the accuracy of a fitted velocity dispersion of  $6 \text{ km s}^{-1}$  improves to better than  $15\%$  for a typical ratio of the measurement uncertainty over the baseline of  $1 \text{ km s}^{-1} \text{ yr}^{-1}$ . However,



there will always remain undetected binaries that affect the observed velocity distribution for any reasonable baseline and measurement uncertainty, which will have to be corrected for (see section 2.3.1). Because the orbital period scales with the orbital velocity to the third power (Kepler's third law), multi-epoch data are far less useful in improving the accuracy of the fitted velocity dispersion of lower-mass clusters (with  $\text{sub-km s}^{-1}$  velocity dispersions) than of young massive clusters.

Unlike the velocity dispersion, the binary fraction fitted with the method tested in this chapter is very sensitive to the assumed binary properties. In general, the method can therefore not reliably recover the binary fraction from a radial velocity dataset if the distributions of orbital parameters of the binaries are poorly constrained.

Although we have tested the method on a sample of radial velocities of O-type stars in R136 and considered binary properties that were derived mainly from spectroscopic surveys of O-type stars<sup>7</sup>, it should also be applicable to samples of B-type stars because they appear to have similar binary properties (Dunstall et al., in preparation). This means that one may only have to use one or two epochs of radial velocities to estimate the velocity dispersion of the massive star population in a large number of young Galactic open clusters that may contain a few O-type stars at most but a much larger number of B-type stars.

We may even speculate that this method may eventually be used to study the dynamics of massive stars in systems where this has been almost impossible up to now. There has been an increasing interest in near-infrared spectroscopy of massive stars in recent years (e.g. Hanson et al. 2005). This wavelength regime offers the possibility of analyzing these stars in embedded regions and near the Galactic center because of the substantially lower extinction than in the optical, and quantitative atmospheric analysis of early-type stars from near-infrared spectral lines is now providing promising results (e.g. Stap et al. 2011). Provided that precise radial velocities can be obtained from near-infrared spectra in reasonable exposure times, then the results presented in this chapter offer a promising and efficient way of studying the dynamics of massive embedded clusters, or even the dynamics of the significant number of Galactic young massive clusters (e.g. Davies et al. 2012), which are strongly affected by extinction and for which we currently have very little kinematic information.

---

<sup>7</sup>Early B-type stars were also included in the study of Kiminki & Kobulnicky (2012).

Tab. 2.1 — Constraints on the distributions of orbital parameters of massive binaries from the literature. The intrinsic binary fractions inferred for these distributions of orbital parameters and their corresponding domain are listed. The intrinsic binary fractions corresponding to an extrapolation of the period distribution to 300 years are also given.

Parameter	<i>pdf</i>	Domain	Variable	Value	Sample	Reference
$\log_{10}(P/\text{day})$	$(\log_{10} P)^\pi$	0.15 — 3.5	$\pi$	$-0.55 \pm 0.22$	Galactic clusters	Sana et al. (2012)
		0.15 — 3.5		$-0.45 \pm 0.30$	30 Doradus	Sana et al. (2013)
		0.0 — 3.0		$0.2 \pm 0.4$	Cyg OB2	Kiminki & Kobulnicky (2012)
$q = M_2/M_1$	$q^\kappa$	0.1 — 1.0	$\kappa$	$-0.1 \pm 0.6$	Galactic clusters	Sana et al. (2012)
		0.1 — 1.0		$-1.0 \pm 0.4$	30 Doradus	Sana et al. (2013)
		0.005 — 1.0		$0.1 \pm 0.5$	Cyg OB2	Kiminki & Kobulnicky (2012)
e	$e^\eta$	0 — 0.9	$\eta$	$-0.45 \pm 0.17$	Galactic clusters	Sana et al. (2012)
		0 — 0.9		-0.5 (fixed)	30 Doradus	Sana et al. (2013)
		0.0001 — 0.9		$-0.6 \pm 0.3$	Cyg OB2	Kiminki & Kobulnicky (2012)
Binary fraction				$69 \pm 9\%$	Galactic clusters	Sana et al. (2012)
				$51 \pm 4\%$	30 Doradus	Sana et al. (2013)
				$44 \pm 8\%$	Cyg OB2	Kiminki & Kobulnicky (2012)
Binary fraction for extrapolated period distribution				$85 \pm 11\%$	Galactic clusters	Sana et al. (2012)
				$65 \pm 5\%$	30 Doradus	Sana et al. (2013)
				$82 \pm 15\%$	Cyg OB2	Kiminki & Kobulnicky (2012)



### 3 | Westerlund I: stability of a young, massive cluster

#### Abstract

Westerlund I is the richest young cluster currently known in our Galaxy, making it one of the most massive clusters for which we can resolve the individual stars even in the crowded centre. This makes it an ideal target to assess whether massive clusters formed currently will remain bound or will disperse and contribute significantly to the stellar field population. We measure the radial velocity dispersion of Westerlund I to explore whether the cluster is either currently in virial equilibrium, in the process of collapse, or expanding and dispersing into the field. We obtained MIKE/Magellan high resolution optical spectra of 22 post main-sequence stars in Westerlund I for 2 or 3 epochs with a maximum baseline of about one year. Radial velocities variations between these spectra are measured by means of cross-correlation. We calculate the velocity dispersion from the cross-correlation of five yellow hypergiants and one luminous blue variable, that show little radial velocity variations between epochs and have many spectral features in common. After taking into account the effect of small number statistics and undetected binaries, we estimate the velocity dispersion for the massive stars in Westerlund I to be  $2.1^{+3.3}_{-2.1}$  km s<sup>-1</sup>. For several different assumptions concerning possible mass segregation and the elongation of the cluster, we find that Westerlund I is subvirial at the 90% confidence level. We can rule out that the cluster is significantly supervirial at the 97% confidence level, indicating that Westerlund I is currently bound. This implies that Westerlund I has survived past the point where any gas expulsion has taken place and is expected to survive for billions of years. This chapter has been published in Cottaar et al. (2012a).

### 3.1 Introduction

Soon after its launch about twenty years ago, the Hubble Space Telescope identified many massive young star clusters in starburst and merging galaxies (Holtzman et al. 1992). These clusters are so massive that they appear unlikely to disperse in a Hubble time owing to tidal stripping (Lamers et al. 2005), which means they could possibly become globular clusters. However, violent internal or external events could cause the cluster to become unbound, in which case the cluster will dissolve into the field, contributing significantly to the stellar populations of their host galaxy. A likely process behind such an event would be the expulsion by stellar winds or the first supernovas of the remainder of the gas cloud out of which the cluster formed. This scenario has been extensively studied both analytically (Hills 1980; Mathieu 1983; Elmegreen 1983) and with N-body simulations (Lada et al. 1984; Goodwin & Bastian 2006). These studies have found that the expulsion of gas lowers the potential well in which the stars reside, causing a previously virial cluster to expand. The efficacy of the gas expulsion to disrupt clusters depends on several variables, including the star formation efficiency, the timescale of the expulsion (Hills 1980; Mathieu 1983), the spatial distribution of the stars relative to the gas (Chen & Ko 2009; Kruijssen et al. 2012), and whether the stars have achieved virial equilibrium with the potential of the surrounding gas before the gas is ejected (Goodwin 2009). Without studying the dynamical state of these clusters, we do not know which fraction of them would survive to become future globular cluster analogues and which will disperse into the field.

The only information that we have about the dynamic state of these distant massive clusters, that we can currently measure is the radial velocity dispersion (e.g. Bastian et al. 2006). Under the assumption of virial equilibrium the one-dimensional velocity dispersion can be used to estimate the mass of the cluster, if its size is resolved. This mass estimate is called the dynamical mass. The dynamical mass can then be compared to the mass derived from the luminosity of the cluster, assuming a universal IMF. Many clusters have been found to have a significantly higher velocity dispersion, than expected from the luminosity (Bastian et al. 2006). Several explanations of this have been proposed, including that: (i) the IMF might actually be different under extreme star forming conditions (Mengel et al. 2002); (ii) the velocity dispersion might be significantly higher owing to binaries (Kouwenhoven & de Grijs 2008; Gieles et al. 2010b); or (iii) the cluster might be supervirial, for example owing to a recent expulsion of gas from the cluster (Goodwin & Bastian 2006; Baumgardt & Kroupa 2007). These scenarios can be distinguished through observations of a cluster for which we can resolve the individual stars and thus measure the binary properties and the IMF.

Westerlund I is the most massive young cluster currently known in our Galaxy (Portegies Zwart et al. 2010). An analysis of photometric observations with the NTT/SOFI in the JHK<sub>S</sub> bands (Brandner et al. 2008; Gennaro et al. 2011) reveals an elongated cluster with a mass of  $4.9_{-0.5}^{+1.8} \times 10^4 M_{\odot}$ , a half-mass radius  $r_{\text{hm}} = 1.0$  pc, and a distance of  $4 \pm 0.2$  kpc. This distance was also found by comparing the radial velocity of the H II gas in Westerlund I with the rotation curve of the Galaxy (Koches & Dougherty 2007). At this distance from the Galactic center, stellar evolution and Galactic tidal stripping are expected to disperse

Westerlund I over  $\sim 9$  Gyr, if it is currently in virial equilibrium (Baumgardt & Makino 2003). Thus, Westerlund I might represent a precursor of a future low-mass, metal-rich “globular cluster”. However, at an age of 4.5-5 Myr (Crowther et al. 2006; Gennaro et al. 2011) we expect that Westerlund I might be out of virial equilibrium because of a recent expulsion of gas, that has not been converted into stars (Goodwin & Bastian 2006). In this chapter, we describe our measurements of the radial velocity dispersion in Westerlund I to explore whether the cluster is likely to be bound. If Westerlund I is in virial equilibrium, we expect a one-dimensional velocity dispersion of  $\sim 4.6 \text{ km s}^{-1}$  (see section 3.4) for the mass and radius measured by Brandner et al. (2008) and Gennaro et al. (2011).

Mengel & Tacconi-Garman (2007, 2009) previously measured the radial velocity dispersion of Westerlund I using K-band spectra. They found a velocity dispersion of  $9.2 \pm 2.5 \text{ km s}^{-1}$  based on a sample of ten stars. This value could be severely inflated owing to the presence of binaries (Kouwenhoven & de Grijs 2008; Gieles et al. 2010b). Ritchie et al. (2009a,b) also measured the radial velocities for a large sample of members and candidate members of Westerlund I using VLT/FLAMES+GIRAFFE spectra from 8350 Å to 9000 Å over multiple epochs to check for variability and investigate the binary properties of these massive stars.

In this chapter, we present multi-epoch high-resolution spectroscopy to find the velocity dispersion corrected for binaries of Westerlund I and thus constrain the dynamical state of Westerlund I. In section 3.2, we present the observations and discuss the data reduction. In section 3.3, we present the radial velocity variations between epochs caused by binaries or atmospheric instabilities in the target stars, and calculate the velocity dispersion using stars of low variability. The implications of the measured velocity dispersion for the dynamical state of Westerlund I are discussed in section 3.4. Finally we present our conclusions in section 3.5.

## 3.2 Observations & data reduction

Observations were made using the MIKE spectrograph (Bernstein et al. 2003) located on the Magellan Clay telescope at the Las Campanas Observatory in June 2009, August 2009, and July 2010. MIKE has a red and a blue arm, providing two echelle spectra with a combined wavelength coverage from 3200 Å to 9000 Å. A slit of 0.7 arcseconds was used, corresponding to a resolution of 53,000 ( $\sim 6 \text{ km s}^{-1}$  per resolution element). Owing to the large interstellar reddening towards Westerlund I ( $A_V = 9.6 - 12.3$  Negueruela et al. 2010), usable spectra are only obtained red-wards of 5000 Å. We observed 22 of the brightest spectroscopically confirmed members ( $I < 14.7$  mag) selected from Clark et al. (2005). These stars include two of the four red supergiants, all six yellow hypergiants, a sgB[e] star, a LBV in its cool phase, and 12 OB-supergiants. All of these targets were observed for two or three epochs.

The spectra were reduced with the MIKE Redux pipeline<sup>1</sup> with some minor adjustments. All images were bias subtracted using the overscan regions. Flat field images were derived from internal quartz lamp frames. The slit was in place during these measurements to ensure that the variation in wavelengths with the location on the CCD is similar to that in the observations. To obtain the flat field in the dark area between the orders, a diffusing glass was positioned in the optical path just downstream of the slit illuminating the area between the orders. After flat fielding we still found spurious low frequency spatial variations in the illumination of the detector above  $\sim 8200 \text{ \AA}$  for all spectra taken on August 2009 and July 2010, including the internal quartz lamp spectra. These features are slightly weaker for the internal quartz lamp and are spread out by the diffusing glass, suggesting that these features are created in the optical path of the telescope. To correct these variations, we calculated a smoothed flat field, which no longer contains the high frequency pixel-to-pixel variations, but only these low frequency spatial features. Although these spurious features are weaker in the flat field than in the science images, we found that they can still be roughly corrected for by dividing the flat fielded image twice by this smoothed flat field.

The curvature of the orders along the CCD is fitted using traces along the edge of the orders obtained from internal quartz lamp images. The scattered light was fitted from the dark areas between the orders by a B-spline with ten knots and this fit was then subtracted. The long slit of MIKE (five arcseconds) allowed us to identify the sky emission lines in the part of the order not illuminated by the star and subtract these emission lines. Regularly during the nights, ThAr images were taken for wavelength calibration. Two ThAr lamp images were taken at different exposure times to maximize the range of lamp line strengths that could be used in the wavelength calibration. Combined with the position of the orders on the CCD, these ThAr images were used to calculate a wavelength for every pixel on the image. The spectra were optimally extracted onto a common wavelength frame, allowing us to add the subsequent exposures of the same target. The noise was estimated at every pixel as the sum of the Poisson error in the observed flux and the readout noise. This calculated noise is consistent with the variations between multiple subsequent observations of the same target and corresponds to a S/N of over 100 in the red part of the spectra. The flux was normalized using a cubic spline fit with two knots.

To correct for possible off-center placement of the source star along the slit, we checked for zero-point shifts of the wavelength solution in every observed spectrum. To this end, we measured the shift of the telluric absorption lines in our stellar target spectra compared to a National Solar Observatory (NSO) telluric spectrum convolved to the resolution of our spectra. We selected sixteen wavelength ranges that have either no or only very weak contamination from stellar spectral lines or diffuse interstellar bands and that contain strong telluric lines. Over these wavelength ranges we calculated the peak of the cross-correlation between the NSO spectrum and the observed spectra. The shift of the zero-point of the wavelength for every spectrum is the average of the shifts calculated for the sixteen individual wavelength ranges. Figure 3.1 shows the difference between the individual measure-

---

<sup>1</sup>The MIKE Redux pipeline was written by S. M. Burles, J. X. Prochaska and R. Bernstein in IDL (<http://web.mit.edu/burles/www/>).

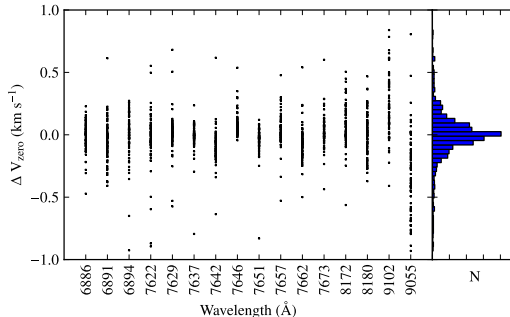


Fig. 3.1 — The offset of the velocity zero point measured for the individual telluric lines from the averaged velocity zero point for sixteen wavelength regions containing strong telluric lines. On the x-axis the central wavelength of these regions is given. On the right, the histogram of all these offsets is plotted. The standard deviation in this distribution is about  $230 \text{ m s}^{-1}$ .

ments and the average offset. The distribution of these variations is quite sharply peaked ( $\sigma = 0.23 \text{ km s}^{-1}$ ). These offsets are smaller than the precision we achieved in measuring the radial velocity variations of our target stars, implying that we are not limited by the accuracy of the wavelength calibration.

### 3.3 Results

#### 3.3.1 Radial velocity variations

Radial velocity variations caused by either binary stars or activity in the stellar atmospheres can inflate our measurement of the velocity dispersion of Westerlund I. To identify the variable stars, we searched for radial velocity variations between epochs over our about one year baseline. We calculated the velocity difference between epochs on a line-by-line basis, by cross-correlating the spectra around selected spectral lines. To determine the peak of the cross-correlation on a sub-pixel level we then fit a Gaussian to the 21 points closest to the peak.

For every spectral line, the procedure described above, provided the spectral shift between any two epochs. We denote this measured spectral shift between epoch  $i$  and epoch  $j$  as  $\Delta V_{ij}$ . When we had data for more than two epochs, then the optimal estimate of the line shift between two epochs was not only measured by the direct cross-correlation between these two spectra ( $\Delta V_{ij}$ ), but also through the difference in the velocities measured relative to any other epoch  $k$  ( $\Delta V_{ik} - \Delta V_{kj}$ ). These different determinations of the spectral shifts are not be the same in general (i.e.  $\Delta V_{ij} \neq \Delta V_{ik} - \Delta V_{kj}$ ). Allende Prieto (2007) showed that it is possible to combine information about the spectral shift from both



Tab. 3.1 — The observed stars with the id of the star from Westerlund (1987) , updated by Clark et al. (2005) (Col. 1), its spectral type (Negueruela et al. 2010; Clark et al. 2010) (Col. 2), the deviation in the velocities measured for a single epoch from the average velocity of that star (Cols. 3-5), and the maximum velocity difference between two epochs (Col. 6). All velocities are in  $\text{km s}^{-1}$ . The relative velocities have been plotted in Figure 3.2.

id	sp. type	13/14-06-2009	10-08-2009	09-07-2010	10-07-2010	$\Delta v_{\text{max}}$
W56	B0 Ia	$-2.6 \pm 1.3$	-	$0.1 \pm 0.8$	$2.5 \pm 1.7$	$5.1 \pm 2.9$
W13	B0.5 Ia	spectroscopic binary <sup>b</sup>				
W238	B1 Iab	$1.2 \pm 1.5$	-	$-1.4 \pm 0.5$	$0.2 \pm 1.1$	$2.6 \pm 2.0$
W23a	B2 Ia	$0.6 \pm 0.8$	-	$1.9 \pm 0.7$	$-2.5 \pm 1.3$	$4.4 \pm 1.9$
W2a	B2 Ia	$-5.2 \pm 1.1$	$-1.1 \pm 0.6$	-	$6.3 \pm 1.2$	$11.5 \pm 2.3$
W11	B2 Ia	$4.6 \pm 0.8$	-	$-6.5 \pm 0.4$	$1.9 \pm 0.8$	$11.1 \pm 1.0$
W28	B2 Ia	$5.7 \pm 0.8$	$-5.7 \pm 0.8$	-	-	$11.3 \pm 1.7$
W71	B2.5 Ia	$-5.9 \pm 0.5$	$5.9 \pm 0.5$	-	-	$11.8 \pm 1.0$
W70	B3 Ia	$-6.2 \pm 0.8$	$6.2 \pm 0.8$	-	-	$12.3 \pm 1.5$
W57a	B4 Ia	$0.4 \pm 0.2$	$-3.3 \pm 0.4$	$1.1 \pm 0.5$	$1.8 \pm 0.4$	$5.1 \pm 0.5$
W33	B5 Ia+	$6.4 \pm 0.8$	$1.2 \pm 1.1$	$-7.6 \pm 0.6$	-	$14.1 \pm 0.8$
W7	B5 Ia+	$-4.0 \pm 0.5$	$2.7 \pm 0.9$	-	$1.3 \pm 0.6$	$6.7 \pm 1.3$
W16a	A5 Ia+	$4.7 \pm 0.2$	$-1.4 \pm 0.4$	-	$-3.3 \pm 0.5$	$8.0 \pm 0.6$
W243 <sup>a</sup>	LBV	$-0.5 \pm 0.3$	$-0.5 \pm 0.2$	$1.0 \pm 0.3$	-	$1.6 \pm 0.6$
W12a <sup>a</sup>	F1 Ia+	$-0.7 \pm 0.4$	$1.2 \pm 0.2$	-	$-0.4 \pm 0.4$	$1.9 \pm 0.5$
W4 <sup>a</sup>	F3 Ia+	$-2.4 \pm 0.2$	$2.4 \pm 0.2$	-	$-0.1 \pm 0.2$	$4.8 \pm 0.4$
W265 <sup>a</sup>	F1-5 Ia+	$-1.2 \pm 0.3$	$2.0 \pm 0.2$	-	$-0.8 \pm 0.2$	$3.2 \pm 0.5$
W32 <sup>a</sup>	F5 Ia+	$-1.8 \pm 0.1$	$1.8 \pm 0.1$	-	-	$3.6 \pm 0.3$
W8a <sup>a</sup>	F8 Ia+	$-0.8 \pm 0.1$	$-0.4 \pm 0.1$	$1.1 \pm 0.1$	-	$1.9 \pm 0.2$
W237	M3 Ia	$0.7 \pm 0.6$	$-1.0 \pm 0.5$	$0.3 \pm 1.0$	-	$1.7 \pm 0.5$
W26	M5-6 Ia	$0.6 \pm 0.2$	$-0.2 \pm 0.1$	$-0.5 \pm 0.3$	-	$1.1 \pm 0.5$
W9	sgB[e]	$0.5 \pm 0.4$	-	$-0.4 \pm 0.4$	$-0.1 \pm 0.2$	$0.9 \pm 0.7$

<sup>a</sup> These stars were been included in our sample to calculate the radial velocity dispersion (see section 3.3.2).

<sup>b</sup> See Ritchie et al. (2010) for a discussion of the spectroscopic binary W13.

the direct cross-correlation and the spectral shifts measured relative to any other epoch, to get a more accurate estimate of the actual spectral shift, called  $\Delta V'_{ij}$  (their equation 3). These estimates obey the relation  $\Delta V'_{ij} = \Delta V'_{ik} - \Delta V'_{kj}$ , and hence can be used to assign a unique velocity to every epoch, relative to some arbitrary zero-point. We set this zero-point to the mean of the relative velocities.

Using the method from Allende Prieto (2007) we can thus estimate the relative velocities between the epochs for every spectral line. Figure 3.2 shows this relative velocity averaged

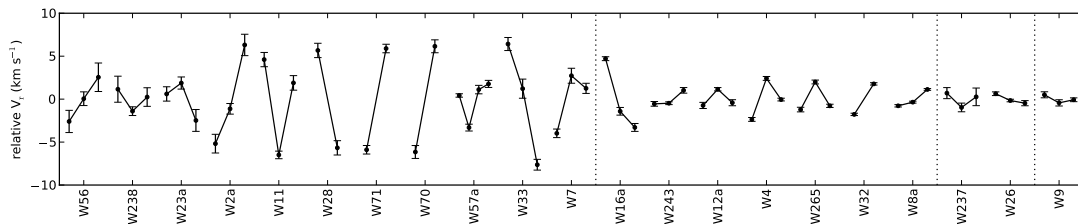


Fig. 3.2 — The radial velocity of an epoch relative to the mean of the velocities of all epochs that the star was observed in  $\text{km s}^{-1}$  with  $1\sigma$  uncertainties. These relative velocities have also been listed in Table 3.1. The vertical dotted lines delineate from left to right, the B-supergiants, the yellow hypergiants (and the LBV W243), the M supergiants, and the sgB[e] star W9. Only the stars W56, W238 and W9 are consistent with having no radial velocity variations.

over all spectral lines for every star, except for the spectroscopic binary W13 (Ritchie et al. 2010). The error bars are given by the standard deviation in the mean, which are an accurate representation of the uncertainty when this is dominated by random Gaussian errors as expected when the noise in the spectra is the main source of uncertainty. These velocity shifts have also been listed in Table 3.1, together with the largest velocity difference measured between two epochs. Only three stars (W56, W238, and W9) are consistent with having no spectral line shifts at the  $2\sigma$  level. All four of these stars tend to have large uncertainties of a few  $\text{km s}^{-1}$ . For all the other stars the radial velocity variations between the epochs are much larger than the quoted error bars, which mean that the same spectral shift is found consistently along multiple spectral lines. A similar analysis of our radial velocity standards reveals a discrepancy between our estimates and the published values (Udry et al. 1999) of about  $0.4 \text{ km s}^{-1}$ . Although this is much smaller than the radial velocity changes that we measured in our target stars, it is still slightly larger than our error estimate, indicating that we might have underestimated our errors. We note that radial velocity changes in our target stars do not have to be caused by a binary star. They may instead be related to stellar activity, such as large-scale super-granulation or changes in the stellar winds. That atmospheric activity can lead to radial velocity variations of many  $\text{km s}^{-1}$  for these massive post-main sequence stars has been well-established (e.g. de Jager 1998; Lobel et al. 1998).

That these spectral line shifts might have an atmospheric as well as a binary origin, is illustrated by the evolution of the spectrum of the M3 supergiant W237 shown in Figure 3.3. Over time, the Ca II line at  $8663 \text{ \AA}$  is seen to evolve differently from most other lines. While the Ca II line was blueshifted in the last epoch (red line in Fig 3.3) relative to the earlier observations, the other lines are clearly redshifted. These inconsistent line shifts occur repeatedly throughout the spectrum and are the cause of the relatively large errors in the relative velocity measurements of W237 relative to the other red supergiant W26 and the yellow hypergiants in Figure 3.2.

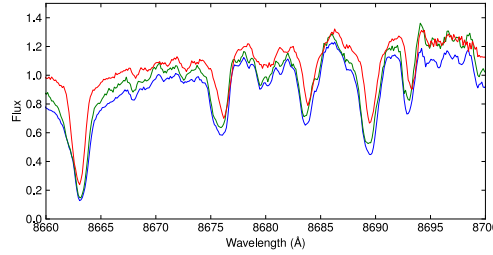


Fig. 3.3 — Part of the spectra of the three epochs of Wd1 237 (M3 Ia) with blue corresponding to June 2009, green to August 2009, and red to July 2010. The Ca II line at 8663 Å is slightly blueshifted in July 2010 relative to the other epochs, while the other lines are clearly redshifted.

Another argument for the importance of stellar activity can be made for W11, W23a, and to a lesser extent W56. These stars show a significant shift in their spectral lines over a one day baseline in July 2010. Although this could be explained by a short-period binary, such short-period binaries are expected to have a velocity amplitude of about  $100 \text{ km s}^{-1}$ . Such a large velocity shift is not found relative to the other epoch of these stars, which were observed on June 2010, which could be a coincidence or caused by either a large inclination or a low mass companion. It is unlikely that these scenarios can explain the observations for *all* stars, suggesting that the spectral line shifts are likely to be caused by atmospheric variability. For the other stars, distinguishing between the spectral line shifts caused by binaries or stellar activity, is difficult. However, given the large observed binary fraction among massive stars, we do expect a significant portion of the radial velocity variations to be caused by binary companions (Sana et al. 2011).

The stars in Table 3.1 and along the x-axis of Figure 3.2 have been roughly sorted by spectral type. The LBV is currently in a cool phase and has many lines in common with the A/F hypergiants. Figure 3.2 displays two trends with spectral type. The first trend is a decrease in the error bars towards later spectral types, which is caused by the far larger sample of spectral lines (most of which are less broad) available for the later type stars. The main exception on this trend is W237, which has been discussed above (see Fig 3.3). The other trend is that the yellow hypergiants and the red supergiants tend to have smaller radial velocity variations than the B-supergiants. This variation is much larger than the error bars, which means that this trend is found consistently for many different spectral lines. This might be because we are sensitive to relatively close binaries with periods of at most a few years. Eldridge et al. (2008) showed that yellow hypergiants and red supergiants in close binaries evolve more quickly into a Wolf-Rayett star, because they lose their hydrogen atmosphere more effectively in binary-induced mass loss. Hence yellow hypergiants and red supergiants in close binaries spend less time in these extended phases before becoming a Wolf-Rayett star than when these stars were in wide binaries or in isolation (Clark et al. 2011). This creates a selection effect, where observed yellow hypergiants or red supergiants tend to have a small fraction of close binaries.

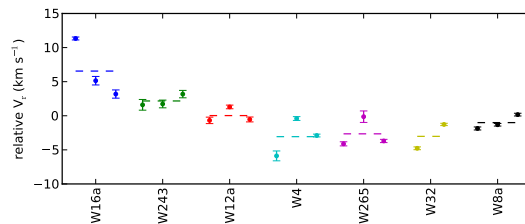


Fig. 3.4 — The velocities of all epochs of the yellow hypergiants and the luminous blue variable relative to each other. The horizontal dashed lines show the mean velocity for every star. The zero-point of the y-axis has been arbitrarily set to the mean of all the velocities.

### 3.3.2 Radial velocity dispersion

We calculate the velocity dispersion of the cluster using only the yellow hypergiants and the LBV. This sample was chosen because these stars in general have small radial velocity variations relative to most other stars and they have a large number of spectral lines in common with each other. The large number of lines in common means that we can measure the velocity dispersion based on the cross-correlation without having to deal with the systematics, which complicate the measurement of the absolute radial velocity. When trying to include more low variability stars in this sample, we find that the extra noise caused by having to place the radial velocities on an absolute scale offsets the advantage that we gain by having a larger sample size. The choice to base our measurement of the velocity dispersion on the cross-correlation implies that a direct comparison with previous radial velocity measurements of the stars in Westerlund I is impossible (Mengel & Tacconi-Garman 2007, 2009; Ritchie et al. 2009a,b).

Using the same method as in our search for radial velocity variations, we used cross-correlations to calculate the relative velocities between the different stars in our sample. The relative velocities for all the epochs of the yellow hypergiants is shown in Figure 3.4 with the mean relative velocity for every star marked as a dashed line. We can see that the velocity variations between epochs of the same star is of the same order as the velocity differences between stars. This implies that Westerlund I has a very small intrinsic velocity dispersion. On the basis of the outlying average velocity and the large velocity change between epochs, we identified W16a as a binary star (or as having a very active atmosphere) and excluded it from our calculation of the velocity dispersion. Below we calculate the velocity dispersion based on the other six stars.

Owing to the small number of stars in our sample, we have a large statistical uncertainty in the measured velocity dispersion. To calculate this statistical uncertainty, we evaluated the likelihood that the observed distribution would have been drawn from a cluster with a

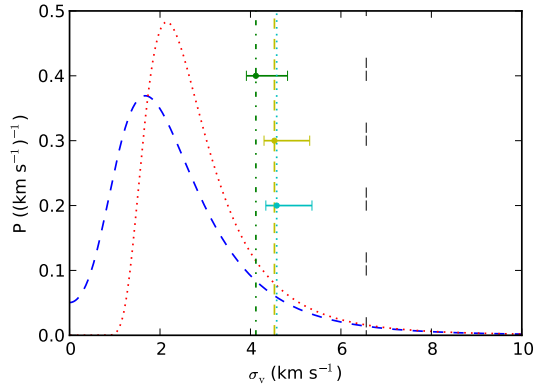


Fig. 3.5 — Our estimate of the probability distribution of the velocity dispersion for the massive stars in Westerlund I. The blue dashed line shows the case where the measurement error is set by the variation in the radial velocity between epochs. The red dotted line shows the limit, where we assume no measurement errors. The vertical lines mark the velocity dispersion expected in virial equilibrium under several assumptions explained in section 3.4. From the highest to lowest estimates, we have the velocity dispersion calculated for a spherical, non-mass-segregated cluster for the mass estimates from Negueruela et al. (2010) (black, long dashed) and Gennaro et al. (2011) (cyan, dotted). For the mass estimate of Gennaro et al. (2011) we also show the expected velocity dispersion taking into account the velocity anisotropy, which is consistent with the elongation of Westerlund I (yellow, dashed), and the case where we take into account both the velocity anisotropy and the possible mass segregation (green, dash-dot). The error bars represent the quoted uncertainty in the photometric mass of Gennaro et al. (2011).

Gaussian radial velocity distribution of standard deviation  $\sigma_v$  and mean  $\mu$

$$P(\sigma_v, \mu) = \prod_i \frac{1}{\sqrt{2\pi(\sigma_v^2 + \sigma_i^2)}} \exp\left(-\frac{(v_i - \mu)^2}{2(\sigma_v^2 + \sigma_i^2)}\right), \quad (3.1)$$

where  $v_i$  is the observed mean velocity of the star and  $\sigma_i$  is the uncertainty in the measured velocity. The likelihood that the observations were drawn from a distribution with a given velocity dispersion is calculated by integrating over  $\mu$ . With only two-three epochs over a one year baseline and most, if not all, stars being variable the uncertainties on the measured radial velocities of the stars ( $\sigma_i$ ) are not well-determined. Owing to this, we considered two cases. In the first case, we set  $\sigma_i^2$  to the variance of the velocity spread between epochs. This leads to the probability distribution shown as the blue dashed line in Figure 3.5 and corresponds to an intrinsic velocity dispersion of  $\sigma = 1.7_{-1.7}^{+3.1}$  km s<sup>-1</sup>, where the errors give the 95% confidence limits. Alternatively, we set  $\sigma_i$  to zero, leading to a velocity dispersion of  $\sigma = 2.1_{-0.9}^{+3.4}$  km s<sup>-1</sup>. This case is shown as the red dotted line in Figure 3.5. We note that the peak in the second case overlaps exactly with the standard deviation in the measured stellar velocities (2.14 km s<sup>-1</sup>).

The second case, with  $\sigma_i = 0$ , can be seen as an “upper-limit estimate” of the probability

distribution of the true velocity dispersion of Westerlund I. This velocity dispersion would be accurate, if the errors were much smaller than  $1 \text{ km s}^{-1}$ . Given the large radial velocity variations measured between epochs, as well as the possibility of undetected binaries with a period of longer than five years and a velocity amplitude of tens of  $\text{km s}^{-1}$ , it is very unlikely that the uncertainties in our estimate of the systematic radial velocity are smaller than  $1 \text{ km s}^{-1}$ . However, including more accurate measurement errors would only decrease the measured velocity dispersion, as illustrated by the case where we set the measurement errors to the variance of the velocity variations between epochs (blue dashed line in Figure 3.5). Increasing  $\sigma_i$  does not change the probability at the larger velocity dispersions significantly, i.e. the upper bound of the 95% confidence limit remains around  $5 \text{ km s}^{-1}$ . Since the uncertainties are not well-defined, we conservatively focus on the case with  $\sigma_i = 0$ .

### 3.4 Discussion

To explore the virial state of the cluster, we compared our measurement of the velocity dispersion with the velocity dispersion expected in virial equilibrium for the photometric mass of Westerlund I. We calculated a first estimate of the velocity dispersion expected in virial equilibrium assuming that Westerlund I is not mass segregated and that the velocities are isotropic. In virial equilibrium, the photometric mass is equal to the dynamical mass, which under these assumptions is given by:

$$M_{\text{dyn}} = \eta \frac{\sigma_{\text{rad}}^2 r_{\text{hm}}}{G}, \quad (3.2)$$

where  $\eta \approx 10$  is appropriate for the density profile found by Brandner et al. (2008),  $\sigma_{\text{rad}}$  is the radial velocity dispersion, and  $r_{\text{hm}} \approx 1.0 \text{ pc}$  (Brandner et al. 2008) is the half mass radius. On the basis of an extrapolation from the number of massive stars in Westerlund I, Negueruela et al. (2010) estimated a stellar mass of about  $10^5 M_{\odot}$ . In virial equilibrium, this corresponds to a velocity dispersion of  $\sim 6.5 \text{ km s}^{-1}$ . This is far larger than our measured velocity dispersion, implying that Westerlund I is subvirial at the 98% confidence level. An alternative photometric mass estimate was given by Gennaro et al. (2011). On the basis of an extrapolation of the measured IMF for the intermediate mass stars between  $3.5 M_{\odot}$  and  $27 M_{\odot}$ , these authors found a lower stellar mass of  $4.9_{-0.5}^{+1.8} \times 10^4 M_{\odot}$ . In virial equilibrium, we would then expect a velocity dispersion of  $4.6_{-0.3}^{+0.8} \text{ km s}^{-1}$ . For this velocity dispersion, our measurements are consistent with a subvirial cluster at the 91% confidence level.

In the conversions from the photometric mass to the velocity dispersion calculated above, we have assumed that the cluster has an isotropic velocity distribution and is not mass-segregated. Both of these assumptions are unlikely to be valid for Westerlund I. An isotropic velocity distribution would generally lead to a spherical cluster (except if the cluster is rapidly rotating). However, Westerlund I is observed to be elongated, with surfaces of constant density lying on ellipses rather than circles (Gennaro et al. 2011). The exact implications of this elongation on the expected velocity dispersion depend on its origins.

Under the assumption that this elongation is supported by a velocity anisotropy and thus is not a transient on the dynamical timescale and is not caused by rapid rotation, which is seldomly seen in older massive clusters, we calculated in Appendix 3.A the expected velocity dispersion. We found that the dynamical mass is given by equation 3.10, which is reproduced here

$$M_{\text{dyn}} = \eta_{\text{ellips}} \eta \frac{\sigma_{\text{rad}}^2 r'_{\text{hm}}}{G}, \quad (3.3)$$

where  $r'_{\text{hm}}$  is the half mass radius, assuming that the density profile in all dimensions is the same as along the observed semi-major axis.  $r'_{\text{hm}}$  can be estimated from the half-mass radius of 1.0 pc (Brandner et al. 2008) and the ellipticity of Westerlund I of 0.75 (Gennaro et al. 2011) to be roughly 1.2 pc. The correction factor for the ellipticity of the cluster  $\eta_{\text{ellips}}$  is approximately 0.85, if the axis along the line of sight is not much shorter than the observed axes. The other parameters in the equation are the same as in equation 3.2. For the photometric mass estimate of  $4.9_{-0.5}^{+1.8} \times 10^4 M_{\odot}$  (Gennaro et al. 2011), taking into account the elongation leads to a only slightly smaller expected velocity dispersion of  $4.5_{-0.2}^{+0.8} \text{ km s}^{-1}$ .

Owing to the tendency of massive stars to reside at the center of massive clusters (i.e. mass segregation), the velocity dispersion of the massive stars that we measured might not be representative of the cluster as a whole (Fleck et al. 2006). To calculate the effect of mass segregation on the difference between the measured and expected velocity dispersion, we separate the cluster into two populations. The first population represents the massive post-main sequence stars from which our sample was drawn, with a half-mass radius of 0.44 pc and a mass of  $6 \times 10^3 M_{\odot}$  (Clark et al. 2005; Negueruela et al. 2010). The second population contains the remaining low and intermediate mass stars in the cluster, with a half-mass radius of 1.0 pc and a much higher total mass of  $4.3 \times 10^4 M_{\odot}$  (Brandner et al. 2008). For a cluster whose stellar volume density is well-represented by a Plummer sphere, we compute the velocity dispersions of both populations, taking into account that they are embedded in the potential well of the other population (equation 7.158 in Binney & Tremaine 2008). We found that in virial equilibrium the velocity dispersion of the total population is about 10% larger than for the subset of massive stars using this two-fluid approximation. This would lead us to expect to measure a velocity dispersion of roughly  $4.1_{-0.2}^{+0.7} \text{ km s}^{-1}$  for a mass-segregated, elongated cluster.

The estimated effect of the mass segregation is small, because the degree of mass segregation is relatively small and the population containing the post-main sequence star is massive enough to nearly become self-gravitating. If our population of observed stars is better represented by a population with both a smaller radius and a lower total mass (to prevent self-gravitation), the ratio of the low-mass to high-mass velocity dispersion could be much higher. Although equipartition is never reached the low-mass stars could have a velocity dispersion up to about a factor of 2 higher after long relaxation (Trenti & van der Marel 2013). However, there is no evidence of such a strong mass segregation in the observed distribution of stars.

Besides showing the probability distribution of the velocity dispersion of the massive stars in Westerlund I implied by our observations, Figure 3.5 also illustrates the veloc-

ity dispersions expected in virial equilibrium based on the various assumptions discussed above. Even for the lowest estimate, our observations still imply that Westerlund I is either subvirial or virial. For the probability distribution including a rough estimate of our measurement errors, we inferred a 91% probability of the observed velocity dispersion being smaller than the smallest estimate of  $4.1 \text{ km s}^{-1}$ . For the more conservative probability distribution, which assumes no measurement errors, we found a 87% probability.

For the cluster to be unbound, the kinetic energy has to be higher than the binding energy, which would correspond to a velocity dispersion  $\sqrt{2}$  larger than expected in virial equilibrium. This can be excluded with at least 97% confidence from our measurements, with the exact percentage depending on the assumptions made. This implies that Westerlund I is bound and has survived any recent gas expulsion. To survive the gas expulsion, Westerlund I should either have had a high star-formation efficiency, which would cause the cluster to remain close to virial equilibrium or the stars in the cluster should have been dynamically cold at the moment the gas was expelled (Goodwin 2009). If the case of Westerlund I were typical of a massive cluster, the excessive velocity dispersion measured for extragalactic clusters would not automatically be indicative of a supervirial cluster, but have another origin, for example in binaries (Gieles et al. 2010b). In any case, Westerlund I itself will not disperse into the field quickly and likely persist for billions of years.

### 3.5 Conclusions

We have presented multi-epoch high resolution spectra of 22 massive post main-sequence stars in the young, massive, Galactic cluster Westerlund I. For 21 of these 22 stars, the velocity variations have been measured between multiple epochs by means of cross-correlation (see Table 3.1 or Fig. 3.2). Many of these stars seem to show radial velocity variations at the one to ten  $\text{km s}^{-1}$  level. Some of these variations might be explained by an underestimate of our uncertainties. Alternatively, these variations could be caused by either binaries or instabilities/waves in the complex atmospheres of these super- and hypergiants.

Using the five least variable yellow hypergiants and the LBV, we have measured a velocity dispersion for the massive stars in Westerlund I of  $\sigma = 2.1_{-0.9}^{+3.4} \text{ km s}^{-1}$  with a confidence limit of 95%, assuming no significant errors in the measured radial velocity differences between the stars. In reality, even these least variable stars have displayed radial velocity variations between epochs of a few  $\text{km s}^{-1}$ , implying that the quoted velocity dispersion is only an upper limit to the true velocity dispersion.

In Figure 3.5, the probability distribution of the velocity dispersion from our measurements have been compared to several estimates of the velocity dispersion that we expect in virial equilibrium. These estimates have been calculated using different estimates of the total mass of Westerlund I, as well as different rough approximations of the effects of both possible mass segregation and a velocity anisotropy, as suggested by the observed spatial elongation of Westerlund I. For all of these cases the observations are consistent with those



of a subvirial cluster. For the lower photometric mass estimate of Gennaro et al. (2011), the observations are also consistent with the cluster in virial equilibrium. In all cases, we have excluded that Westerlund I is significantly supervirial, implying that the cluster is bound, and that it has survived any recent gas expulsion. Barring any violent interactions with other clusters or molecular clouds, Westerlund I, which might be the most massive young cluster in our Galaxy, is expected to survive for billions of years.

## Acknowledgments

NSO/Kitt Peak FTS data used here were produced by NSF/NOAO. We would like to thank Justin Read, Kevin Covey, Richard Parker, Phil Massey, and Hans Martin Schmidt for helpful discussions. We are also very grateful to an anonymous referee, whose comments and suggestions led to major improvements in the chapter.

### 3.A Appendix: Velocity dispersion in ellipsoidal cluster

The density distribution of both the massive and intermediate mass stars in Westerlund I has been shown to be elongated (Negueruela et al. 2010; Gennaro et al. 2011). We calculated the effect of this elongation on the dynamical mass calculation of Westerlund I, under the assumption of an ellipsoidal density profile, as suggested by Gennaro et al. (2011), who fitted a density profile to their stellar density distribution of Westerlund I, where the lines of constant densities lie along ellipses instead of circles. To limit the number of free parameters as well as greatly simplify the equations, we assumed that one of the axis of the ellipsoid lies along the line of sight. The other two axes are then the axes found by Gennaro et al. (2011) in the plane of the sky. We defined the length of the semi-major axis found by Gennaro et al. (2011) as  $a_1$ , the length of the semi-minor axis as  $a_2$ , and the length along the line of sight as  $a_3$ , the last of which is unconstrained by observations.

For an ellipsoidal cluster in virial equilibrium, an elongation implies a velocity anisotropy, which is given by the tensor form of the virial theorem

$$2K_{jj} + W_{jj} = 0, \quad (3.4)$$

where  $2K_{jj} = M_{\text{dyn}}\sigma_j^2$  is the tensor form of the kinetic energy along the axis  $j$  and  $W_{jj}$  is the potential energy tensor. For an ellipsoidal system, this potential can be represented as the in a product of two factors (see eq 2.144 in Binney & Tremaine 2008), one that depends only on the axial ratios of the cluster, and another that is independent of either the clusters ellipticity or the axis along which the potential energy tensor is calculated and depends only on the density dropoff along a single axis, which we take to be the observed semi-major axis. In functional form, this corresponds to

$$W_{jj} = -f_j(a_1, a_2, a_3) * g(\rho_{\text{along semi-major axis}}), \quad (3.5)$$

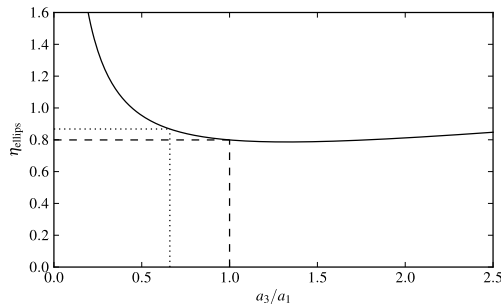


Fig. 3.6 — The correction factor  $\eta_{\text{ellips}}$  needed to take into account the spheroidal shape of the cluster plotted against the ratio of the length of the axis along the line of sight to the length of the observed semi-major axis for an observed ellipticity of 0.75 ( $a_2/a_1 \approx 0.66$ ). The cases where the density dropoff along the line of sight is the same as the semi-major axis (dashed) and the same as the minor axis (dotted) are shown.

with

$$f_j(a_1, a_2, a_3) = \frac{3}{2} \frac{a_2 a_3}{a_1^2} \left( \frac{a_j}{a_1} \right)^2 A_j, \quad (3.6)$$

where the  $A_j$  are a complex function of the axial ratios given by Table 2.1 in Binney & Tremaine (2008). We note that the equations in this table assume that  $a_1 > a_2 > a_3$ , which will make it necessary to rearrange the indices, if the axis along the line of sight is not the shortest.

Since  $g$  does not depend on both  $a_2$  and  $a_3$ , we can calculate this term for the spherical case, where we set  $a_2$  and  $a_3$  to  $a_1$ . For a spherical cluster we have  $A_j = 2/3$ , so  $f_j(a_1, a_2, a_3) = 1$  and  $W_{jj} = \frac{1}{3}W$ , where  $W$  is the total potential energy. Using the equation for the dynamical mass of a spherical cluster (e.g. Portegies Zwart et al. 2010), we get

$$W_{jj,\text{circ}} = -g = -\frac{1}{\eta} \frac{GM'_{\text{dyn}}{}^2}{r'_{\text{hm}}}, \quad (3.7)$$

where  $\eta \approx 10$  (Portegies Zwart et al. 2010) for the density profiles fitted by Brandner et al. (2008) and Gennaro et al. (2011),  $M'_{\text{dyn}}$  is the mass of this circular cluster, and  $r'_{\text{hm}}$  is the half-mass radius of this cluster. The dynamical mass of this artificial spherical cluster is related to the mass of the spheroidal cluster with

$$\frac{M'_{\text{dyn}}}{M_{\text{dyn}}} = \frac{a_1^3}{a_1 a_2 a_3}. \quad (3.8)$$

Entering equations 3.6-3.8 into the equation for the ellipsoidal potential energy tensor gives

$$W_{jj} = -\frac{3}{2} \frac{a_j^2}{a_2 a_3} A_j \frac{1}{\eta} \frac{GM'_{\text{dyn}}{}^2}{r'_{\text{hm}}}. \quad (3.9)$$

Combined with the virial equation (Eq. 3.4) for the radial velocity dispersion ( $j = 3$ ) this can be converted as

$$M_{\text{dyn}} = \eta_{\text{ellips}} \eta \frac{\sigma_{\text{rad}}^2 r'_{\text{hm}}}{G}, \quad (3.10)$$

where the correction for the ellipsoidal structure has been completely integrated in  $\eta_{\text{ellips}}$ , which is defined as

$$\eta_{\text{ellips}} \equiv \frac{2}{3} \frac{a_2}{a_3} \frac{1}{A_3}. \quad (3.11)$$

This correction factor depends only on the axial ratios. For an ellipticity along the line of sight of 0.75 ( $a_2/a_1 \approx 0.66$ ) (Gennaro et al. 2011), we plot the dependence of this correction factor on  $a_3/a_1$  in Fig. 3.6. This figure shows that there is only a small dependence of the correction factor on the actual length of the axis along the line of sight for  $a_3/a_1 > 0.5$ . In this range, an increase in the length of the axis causes the total potential and thus the total kinetic energy to drop. However, this sharp decline in kinetic energy mostly corresponds to a lowering of the velocity dispersion in the plane of the sky, with the radial velocity dispersion staying roughly constant. This interplay between the change in the total kinetic energy and the division of this kinetic energy over the three axes produces the curve shown in Fig. 3.6.

## 4 | IC 348

### Abstract

How stellar groups emerge from their molecular clouds is still very uncertain. Here I present the spectral analysis based on forward modeling of high-resolution, near-infrared spectra from APOGEE of the Sloan Digital Sky Survey III as part of the IN-SYNC collaboration. I show that for cool stars (temperature  $< 4500$  K) the radial velocities, effective temperature, and surface gravities can be reproduced with a precision of respectively roughly  $300 \text{ m s}^{-1}$ ,  $100 \text{ K}$ , and  $0.1 \text{ dex}$ , while the precision degrades for hotter stars. The precision in the spectroscopic surface gravities suffices to confirm its luminosity spread in the young cluster IC 348 and the precision in the radial velocity suffices to resolve the velocity distribution of these young stellar groups. We find that IC 348 is likely supervirial (but bound) and that the more deeply embedded stars in cluster are blueshifted with respect to less deeply embedded stars, indicative of collapse. These measurements can be reconciled if the cluster is regaining virial equilibrium after a major disruption. Finally we report a tentative detection of a velocity gradient in IC 348.

### 4.1 Introduction

Studies tracing molecular gas in dense prestellar cores have found that they have very similar velocities. Despite being embedded in a turbulent molecular cloud with velocity dispersions of over  $1 \text{ km s}^{-1}$  (Larson 1981), they have core-to-core radial velocity dispersions of only  $200 - 400 \text{ m s}^{-1}$  in the Rho Ophiuchi molecular cloud (André et al. 2007) and the Perseus molecular cloud (Kirk et al. 2007). These motions seem to be insufficient to prevent collapse due to gravity (e.g. Kirk et al. 2007), which suggests that newly-formed stars will fall into the potential well of the molecular cloud. The kinetic energy gained by

the stars during this collapse might also be important in the dispersal of the stellar cluster after the molecular cloud disperses.

We need detailed kinetic information of young, embedded and recently exposed clusters to learn more about this potential initial collapse, and which embedded clusters will remain bound and which will dissolve into the field population. With this goal in mind the multi-object, high-resolution, near-infrared spectrograph APOGEE targeted hundreds of stars in several nearby star-forming regions as part of the IN-SYNC ancillary science program of the Sloan Digital Sky Survey III (SDSS-III) (Eisenstein et al. 2011). At the time of this writing over 4000 spectra were taken of pre-main sequence stars in the star-forming regions IC 348, NGC 1333, NGC 2264, and Orion. In this work we present the analysis of all of the spectra taken from these young pre-main sequence stars in section 4.3.

In addition we present here the first scientific results from this dataset on the dynamical state of the young cluster IC 348 at the edge of the Perseus molecular cloud. This cluster contains more than 400 stars (Luhman et al. 2003; Muench et al. 2007; Luhman 2008), 339 of which have been targeted by APOGEE. Estimates of the age vary from 2-3 Myr (e.g. Luhman et al. 2003) to 6 Myr (Bell et al. 2013), which makes it one of the youngest known clusters that is already optically revealed. The spherical rather than substructured stellar distribution in IC 348 suggests that the cluster has already dynamically evolved somewhat at this time. This might also explain the mass segregation observed in IC 348 (Schmeja et al. 2008). Previous studies of the dynamics of IC 348 have been limited to one proper motion study from Scholz et al. (1999), which at a precision of  $4 \text{ km s}^{-1}$  was unable to resolve the velocity dispersion of the cluster.

In section 4.2 we discuss the target selection, observations, and data reduction for the APOGEE IC 348 spectroscopic sample. In section 4.3 we present our spectral analysis techniques, with detailed estimates of the precision and accuracy of the resulting stellar parameters. We use these stellar parameters to estimate the extinction and luminosities of the observed stars in section 4.4, leading to a confirmation of a luminosity spread in IC 348 in section 4.4.2. The kinematics of IC 348 are derived in section 2.3.3.2 and discussed in section 2.2.5. Finally our conclusions are presented in section 2.4.

## 4.2 Observations

### 4.2.1 Target selection

Likely IC 348/Perseus members was selected from a catalog of confirmed and candidate IC 348 members compiled by August Muench (private communication), supplemented with mid-IR excess sources identified by the cores-to-discs (c2d) Spitzer survey team (Jørgensen et al. 2006; Rebull et al. 2007). The Muench catalog includes 449 confirmed and candidate IC 348 members; the majority of these sources were drawn from previously published catalogs of photometrically selected, and often spectroscopically confirmed, members (e.g.

Luhman et al. 1998; Luhman 1999; Luhman et al. 2003; Muench et al. 2003; Luhman et al. 2005; Muench et al. 2007). With candidates selected on the basis of deep X-ray observations of the cluster center (i.e. Preibisch & Zinnecker 2001; Preibisch et al. 2003), this catalog is likely highly complete in the cluster center, as verified by our independent analysis of source counts in the region (see Figure 2, below). The Muench et al. catalog does include additional candidates selected via an R vs. R-J color-magnitude cut performed utilizing photometry from the USNO NOMAD catalog, however; these candidates are less secure, particularly at early types, where member selection via the R vs. R-J CMD becomes less efficient due to the steep cluster sequence, and at large radii, where source contamination from members of the background Per OB2 association is expected to become significant.

We provide evidence for the completeness of the target catalogue in the cluster core by studying the distribution of the 2MASS sources that are not in our target catalogue in a similar manner as Cambr esy et al. (2006). If the target catalogue is complete, all of these stars should be background and hence should have the same brightness distribution and spatial density as background stars in an off-cluster field (after correcting for extinction). The upper panel in Figure 4.1 shows the H-band distribution of these untargeted 2MASS sources in the cluster core (blue) and the 2MASS sources in an off-cluster field covering 1200 arcseconds to 1 degree from the cluster center (cyan). In the magnitude range covered by our spectroscopic observations, the distributions are consistent, suggesting that the targeting catalogue is (mostly) complete. This is confirmed in the spatial distribution of non-targeted 2MASS sources with  $H < 14$  (lower panel of Figure 4.1), which shows no remaining overdensity of sources at the location of IC 348.

Although most targets in the outskirts were observed, only about half of the targets in cluster center were observed (Figure 4.2), because APOGEE is unable to simultaneously target stars within  $\sim 71.5$  arcseconds of each other due to a collision through fiber assignment. This meant that even though 7 separate plates were drilled to cover IC 348, many stars in the dense cluster center could still not be targeted.

The priority of the targets was based on the H-band magnitude. The highest priority was given to stars with  $7 < H < 12.5$ . For these high priority target we are mostly complete ( $\sim 90\%$ ), even in the cluster center (upper panel in Figure 4.1). For fainter targets the priority was assigned based on the H-band magnitude after correction of the background extinction. Brighter stars were targeted first.

### 4.2.2 APOGEE

APOGEE is a multi-object, high-resolution ( $R \sim 20,000$ ) spectrograph, whose spectra cover most of the H-band in the near-infrared from 1.52 to 1.69 microns. In this work we analyze the spectra in the ApVisit files <sup>1</sup>, which have already been corrected for telluric emission and absorption lines, as well as wavelength calibrated (based on ThArNe and UNE

<sup>1</sup>The data reduction pipeline to produce these files is described at <http://www.sdss3.org/dr10/irspec/apred.php>

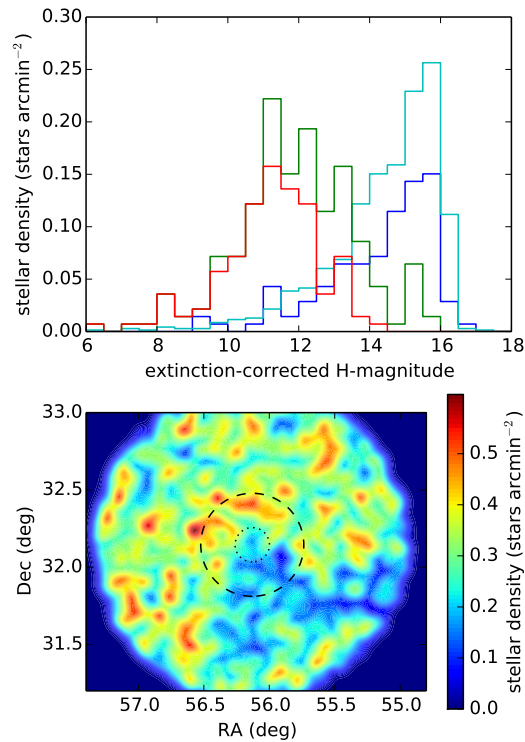


Fig. 4.1 — The upper panel shows the stellar density distribution per bin of H-band, corrected for the background extinction as estimated from the sub-millimeter continuum observed by Herschel. The various histogram show the stellar density of potential targets (green), the stars actually observed (red), the 2MASS sources classified as background within the cluster center (within 400 arcseconds; blue), and 2MASS sources outside of the cluster (further than 1200 arcseconds; cyan). The bottom panels shows the density distribution of all 2MASS sources not classified as potential members with  $H < 14$ . The two circles are at 400 (dotted) and 1200 (dashed) arcseconds from the cluster center (same as in Figure 4.2). The lack of an overdensity of 2MASS sources classified as background at the position of IC 348 provides evidence for the completeness of the adopted targeting catalog.

lamps). A complete description of the data reduction leading to these spectra is described in Nidever et al. (in prep).

The total dataset analyzed consists of 12,957 APOGEE spectra of 4773 young pre-main sequence stars. Exposure times varied from 500 to 3000 seconds, with a typical value of 2000 seconds. This led to a wide variety of signal-to-noise ratios with 90/% lying between 20 and 300 and a median of 66. The number of observations per star differs greatly per star-forming regions, with up to 13 spectra per star in IC 348. The spectra were taken over a total baseline of 1 year.

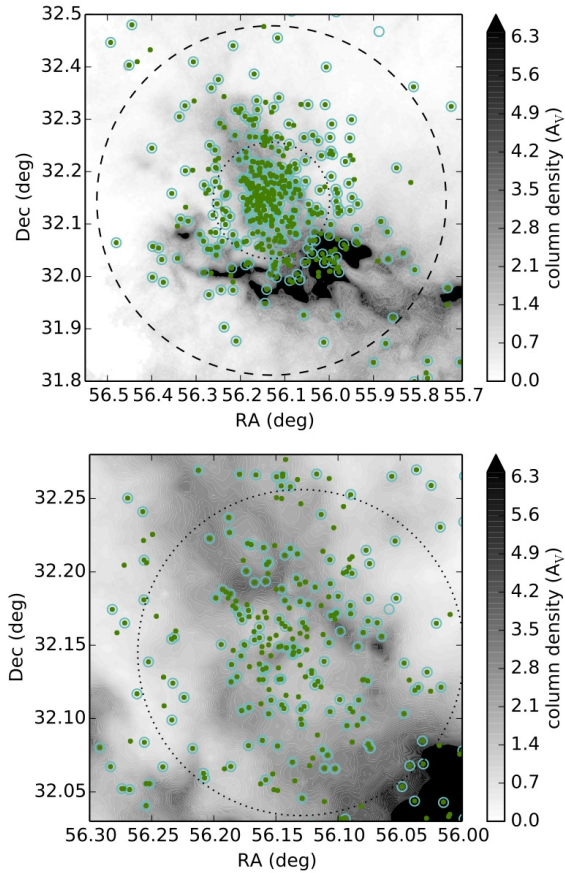


Fig. 4.2 — Map of potential targets in green. Stars circled in cyan have been observed. Additional background stars observed to fill up the APOGEE fibers have not been marked. The lower panel shows a zoom-in of the center of the upper panel, illustrating the lower coverage in the cluster center. For comparison with Figure 4.1 we added two circles at 400 (dotted) and 1200 (dashed) arcseconds from the cluster center.

### 4.3 Spectral analysis

We apply a forward modeling approach to derive stellar parameters from the observed spectra, similar to Blake et al. (2007, 2010). In section 4.3.1.1 we summarize this approach, with more details on the spectroscopic model given in section 4.3.1.2 and more details on the fitting procedure in section 4.3.1.3. In section 4.3.2 we discuss in more detail the precision and accuracy of the derived stellar parameters.



### 4.3.1 Forward modeling

#### 4.3.1.1 Overview

We model the observed spectra with synthetic spectra with five degrees of freedom: the effective temperature, surface gravity, radial velocity, rotational velocity, and H-band veiling due to possible flux from an inner disc. These synthetic spectra are then compared with the observed spectra and the  $\chi^2$ -offset between them is minimized. Finally the uncertainties on the best-fit stellar parameters are computed by a Markov chain Monte Carlo (MCMC) simulation. Sample fits have been shown in Figure 4.3.

For most stars in our sample we have obtained multiple spectra. Rather than fitting each spectrum individually, we simultaneously fit all spectra obtained for a single star. This allows us to fit a single effective temperature, surface gravity, and rotational velocity to each star, while allowing the radial velocity and veiling to vary between epochs.

#### 4.3.1.2 The model

First we prepared a grid of synthetic spectra. As a basis for our forward modeling approach, we adopt the grid of synthetic spectra from BT-Settl (Allard et al. 2011) at solar metallicity for the solar abundances from Caffau et al. (2011). These spectra cover the complete visible and near-infrared wavelength range with very high resolution, and accurately reproduce interferometrically determined bolometric effective temperatures when fit to low-resolution visible and near-infrared spectra of calibrator stars (Mann et al. 2013).

We first degraded the BT-Settl spectra to match APOGEE’s resolution of  $\sim 22,500$ . To do this efficiently we resampled the spectra onto a wavelength grid covering the H-band with a sampling resolution of 700,000. The spectra were then convolved with a Gaussian, whose full width at half maximum is set to  $700,000 / 22,500 = 31.1$  pixels. Then we down-sampled the spectra to a sampling resolution of 300,000. This sampling resolution was chosen to minimize the computational time needed to rotationally broaden and interpolate the spectra, while still being sufficiently dense so that the spectrum can be accurately interpolated to the observed wavelength grid.

During the fitting procedure we vary the effective temperature and surface gravity as continuous variables. We use cubic interpolation to extract spectra at arbitrary effective temperatures and surface gravities between the grid points. These extracted spectra are then post-processed to produce synthetic spectra with different radial velocities, rotational velocities and levels of veiling:

1. The wavelength grid is Doppler-shifted by a given radial velocity.
2. The spectral lines are rotationally broadened by convolving the flux array with the

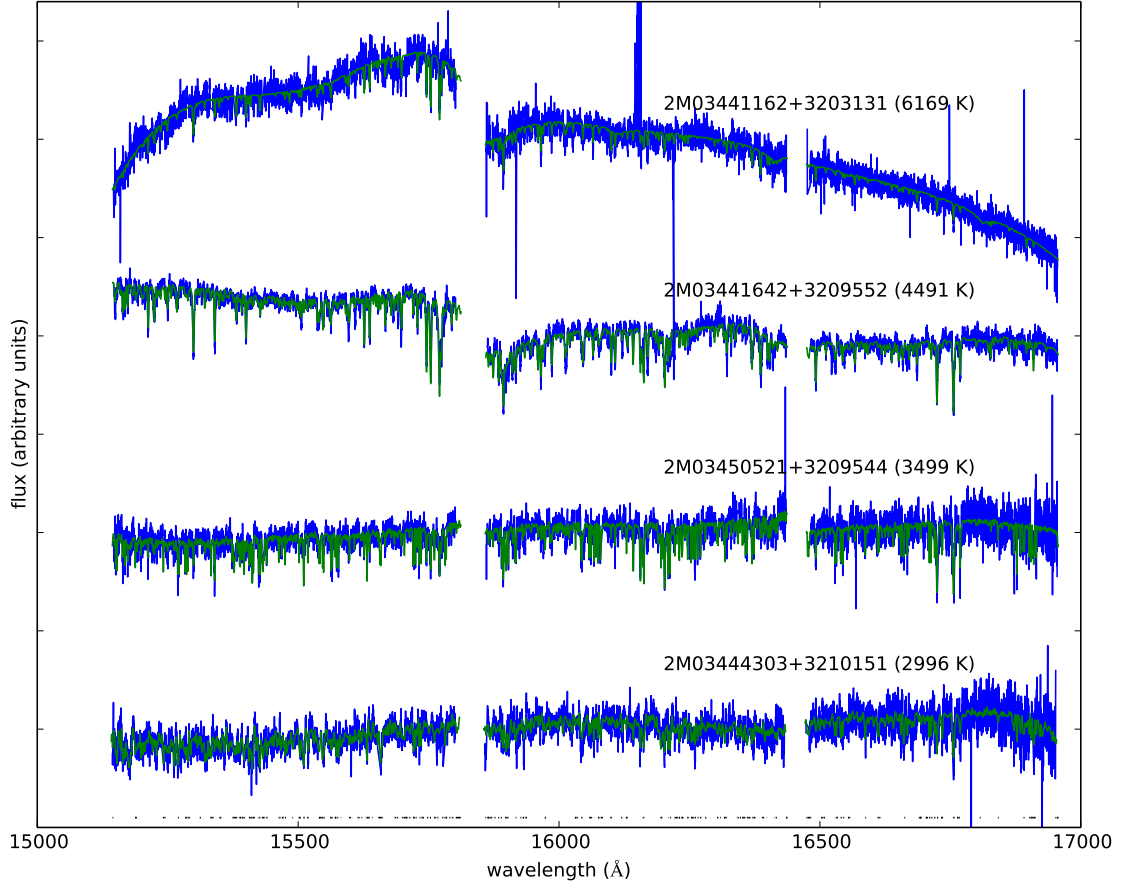


Fig. 4.3 — Sample fits of pre-main sequence stars in IC 348 for effective temperatures around 3000, 3500, 4500, and 6000 K. The blue lines show the observed spectrum in a single epoch and the green lines the best-fit spectrum. Residual sky emission lines and bad pixels have been masked out. The horizontal black lines in the bottom show the typical extent of this masking. The two gaps in every spectra separate the three CCDs of APOGEE.

rotational profile from equation 17.12 in Gray (1992):

$$\text{kernel}(v_i) \propto 2(1 - \epsilon) \sqrt{1 - \left(\frac{v_i}{v \sin i}\right)^2} + \frac{\pi\epsilon}{2} \left(1 - \left(\frac{v_i}{v \sin i}\right)^2\right), \quad (4.1)$$

where  $\epsilon = 0.6$  is a parameter describing the limb darkening,  $v \sin i$  is a variable representing the projected rotational velocity, and  $v_i$  is the pixel offset in units of velocity.

3. A flat featureless flux is added to represent the veiling of the spectral lines due to flux from the inner part of the discs. This veiling flux is parameterized by  $R_H$ , the ratio of the non-stellar and stellar flux in the H-band.

Before comparing the fluxes from the synthetic and observed spectrum, we fit the continua, so that the  $\chi^2$  is determined by how well the spectral lines match and is not dominated by the slope of the continuum. For this purpose we multiply the synthetic spectrum with a polynomial. This polynomial is recomputed for every synthetic spectrum to minimize  $\chi^2$  of that fit. It is computed separately for the three chips of the APOGEE spectra. The degree of the polynomial is varied according to the optimization scheme described below.

#### 4.3.1.3 The fitting

After matching the continua, the  $\chi^2$  is computed for that synthetic spectrum. During this process any pixels covered by telluric emission lines or marked by the APOGEE pipeline as bad are masked: a typical spectrum has 20% of its pixels masked (Figure 4.3).

The procedure described above allows us to efficiently compute the  $\chi^2$  between the synthetic and observed spectra for a set of stellar parameters. We minimize this  $\chi^2$  using a three-step procedure:

1. First an initial set of best-fit parameters are found by a global minimization of the  $\chi^2$  by varying the radial velocities and veiling in every epoch and varying a single effective temperature, surface gravity, and rotational velocity per star. At this stage a second-order polynomial is used for every chip in every spectrum to match the continuum of the observed spectrum. To find the global minimum we use the differential evolution routine implemented by Stepan Hlushak as part of the OpenOpt python library (Kroshko 2007). This routine alters a set of initially random candidate solutions by proposing for every candidate a new set of parameters by moving it in the direction of other candidate solutions. The proposed solution will replace the original solution, only if it is an improvement in a  $\chi^2$ -sense. This optimization is run over the whole range of effective temperatures (100 - 7000 K) and surface gravities (0-5.5) covered by the BT-Settl grid, as well as a wide range in veiling (0 -  $10^3$ ), rotational velocity (0 -  $10^3$  km s<sup>-1</sup>), and radial velocity ( $-10^3$  -  $10^3$  km s<sup>-1</sup>).
2. For the initial best-fit stellar parameters the degree of the polynomial used to match the continuum is optimized using Bayes Information Criterion (BIC). According to BIC another parameter should only be added (by increasing the order of the polynomial) if it decreases the  $\chi^2$  with at least the natural logarithm of the number of data points ( $\ln n \approx 8$  for the APOGEE spectrum on a single chip). The optimum polynomial degree found in this step is typically between two and five and is kept fixed throughout the rest of the minimization and the MCMC simulation.
3. Finally the  $\chi^2$  is minimized locally using a Nelder-Mead downhill routine to adjust the parameters in response to the change in the polynomial degree. During this final optimization the stellar parameters are only bounded by the limits in effective temperature and surface gravity of the grid of synthetic spectra, as well as the physical requirements of non-negative veiling and rotational velocity.

Starting from the global  $\chi^2$  minimum we aim to compute the uncertainties on the best-fit stellar parameters. For this we use the MCMC routine “emcee” (Foreman-Mackey et al. 2013), which is based on the affine-invariant sampler from Goodman & Weare (2010). In this routine multiple walkers (200 in our case) make a constrained random walk through the parameter space, where the direction of the next step is informed by the positions of the other walkers. The distribution of walker positions after the burn-in phase is used to compute a first estimate of the uncertainties on the stellar parameters (which is later corrected in section 4.3.2.1).

Although the quoted parameters depend only on the Markov chain, it is still important to first minimize the  $\chi^2$  to provide a starting point for the MCMC. Starting at (or close to) the  $\chi^2$  minimum greatly shortens the burn-in time (i.e. convergence) of the MCMC. This burn-in phase can be very long for a routine like “emcee”, because every walker will have to reach the global minimum before their distribution start reflecting the uncertainties on the stellar parameters.

### 4.3.2 Precision and accuracy

#### 4.3.2.1 Statistical uncertainties on stellar parameters

Statistical uncertainties should measure the precision of the observed stellar parameters; in other words they describe how much variation we would expect in the observed value if the measurement was repeated. Given an accurate error array for the observed spectrum, these statistical uncertainties are estimated by the MCMC. Here we check these estimates of the statistical uncertainties by checking the variations in best-fit stellar parameters between multiple epochs and looking at the best-fit reduced  $\chi^2$ .

The distribution in reduced  $\chi^2$  should peak at one for a good fit. However, the observed distribution peaks at two to four rather than at one (upper row in Figure 4.4) for all stars fitted in preparation of this chapter (i.e. hundreds of pre-main sequence stars in IC 348, NGC 1333, NGC 2264, Orion, and the Pleiades and several hundred field stars). This implies either a poor fit or an underestimation of the error array. To distinguish between these scenarios we check whether the variability in the radial velocity and veiling between epochs is consistent with the noise levels. We expect some real variability in these parameters (e.g. due to spectroscopic binaries), however the variability between multiple epochs is consistently several times higher than expected from the noise array in each spectrum (lower two rows in Figure 4.4). Combined this strongly suggests that the noise in the spectra is underestimated by a factor of two to four, which might be partly due to a correlation introduced in the errors of neighboring pixels during the resampling. Irrespective of the origin, we take this apparent underestimation of the uncertainties in our derived parameters into account by tripling the uncertainties on the stellar parameters. These tripled uncertainties will be used throughout this chapter.

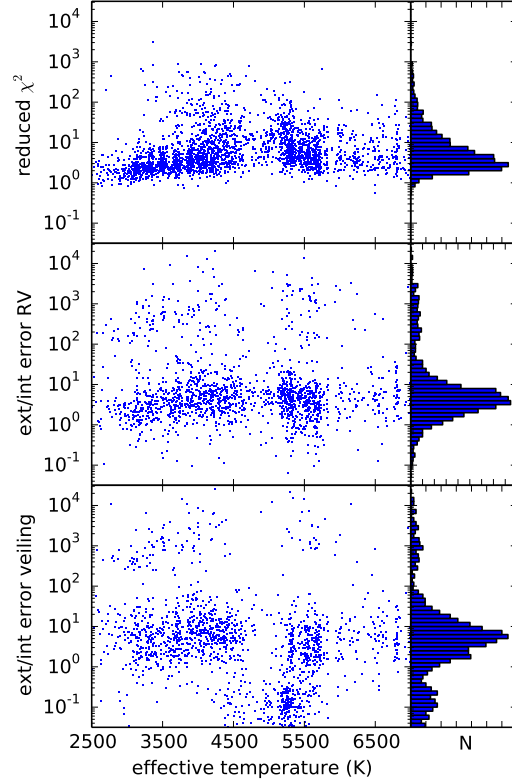


Fig. 4.4 — The reduced- $\chi^2$  distribution (upper row) and the external over internal uncertainties for the radial velocity (center row) and the veiling (lower row). In every row the left panel shows the dependence on effective temperature with the histogram of the distribution in the right panel. Only stars for which two or more epochs have been observed are included in the lower row, while all stars are included upper row. The low external uncertainties for the veiling around 5000 K are due to the best-fit veiling for stars at these temperatures to be typically negative, which is below the lower limit of zero.

#### 4.3.2.2 Velocity zero-point

To compare with previous radial velocity observations, as well as measurements of the gas velocity in IC 348 we need to characterize the accuracy of the zero-point of the observed radial velocities. Furthermore, to measure the velocity dispersion of a cluster the velocity zero-point should be independent of stellar parameters.

We find a systematic offset of a few  $\text{km s}^{-1}$  for the coolest stars ( $T_{\text{eff}} < 3500$  K) with respect to the hotter stars in the same cluster. Figure 4.5 shows this trend for three young clusters observed with APOGEE, namely IC 348 (blue squared), the Pleiades (cyan diamonds), and NGC 1333 (red circles). If this offset was real the low-mass stars with

$T_{\text{eff}} < 3000$  K would separate from the cluster containing the hotter stars in less than a few Myr. Because such a translational separation based on mass has never been observed, we conclude that the trend of the mean radial velocity with temperature is unphysical and is caused by a systematic error in the measured radial velocities.

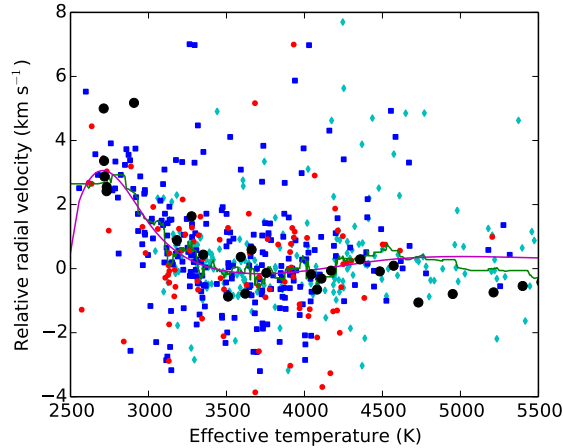


Fig. 4.5 — The trend of the radial velocity zero-point with effective temperature. For all stars with an RV precision better than  $1 \text{ km s}^{-1}$  in IC 348 (blue squares), the Pleiades (cyan diamonds), and NGC 1333 (red circles) the weighted means of the radial velocities measured over all observable epochs are plotted relative to the median radial velocity for stars hotter than 4000 K. In black the radial velocities derived from NIRSPEC H-band spectra of RV standards from Prato (2007) are plotted relative to their literature values. Finally the green trend line is computed by median-filtering the individual radial velocity offsets and the magenta line shows the best-fit cubic spline through this trend line.

We are able to reproduce this systematic offset with effective temperatures under a wide variety of conditions. The same systematic offset was found in the SYNTHVHELIO radial velocities measured for cool dwarves by the APOGEE radial velocity pipeline. The APOGEE RV pipeline measures SYNTHVHELIO values by cross-correlating, not  $\chi^2$ -minimizing, each APOGEE spectrum against its best-fitting synthetic template from the APOGEE RV mini-grid. The APOGEE RV mini-grid is primarily drawn from a set of synthetic spectra calculated by the APOGEE/ASPCAP team from a custom line list and Kurucz model atmospheres for warmer stars ( $T_{\text{eff}} > 3500$  K), but also includes BT-Settl models for  $T_{\text{eff}} < 3500$  K to extend the grid to better cover the coolest dwarfs. The presence of a similar systematic offset in the SYNTHVHELIO values measured for the coolest dwarfs in IC 348, NGC 1333, and the Pleiades suggest that the offset is related to the shared usage of the BT-Settl model grid as an RV zero-point, rather than the distinct and independent RV measurement algorithms incorporated into the main APOGEE and the IN-SYNC specific analysis pipelines.

To rule out instrumental effects as a potential cause for this apparent RV trend with stellar effective temperature, we first measured multiple independent RV values for each APOGEE spectrum, treating portions of the spectrum sampled by different detectors independently. These independent RV measurements showed the same  $\text{RV}-T_{\text{eff}}$  trend, indicating

that the cause was not isolated to one or two prominent features, but rather affected all parts of the spectra of the coolest stars equally. As a second check on potential instrumental effects that could be causing this trend, we also applied our fitting procedure to NIRSPEC H-band spectra of well-established RV standards obtained and made publicly available by Prato (2007). The RV offsets we measure with respect to these star’s known RVs, which were determined using empirical templates, are included in Figure 5, and show the same trend with effective temperature as the APOGEE spectra, indicating that the RV trend is not an artifact of a particular instrument or reduction procedure.

Having ruled out potential instrumental and algorithmic causes for this  $RV-T_{\text{eff}}$  trend, we then investigated the model spectra themselves as a potential cause of this effect. Re-fitting the APOGEE spectra with synthetic spectra from the Gaia-ESO grid (Husser et al. 2013), we found again the same  $RV-T_{\text{eff}}$  trend, indicating that the cause of this affect is not specific to a single model grid. With the  $RV-T_{\text{eff}}$  seemingly related to multiple model grids, most prominent at cool temperatures, and prevalent throughout the full H-band spectrum, we suggest molecular line-lists as a potential cause of the RV offset.

To compute the velocity dispersion of any of our target clusters we subtract out this systematic offset for all the velocities measured from the APOGEE spectra. We characterize the offset by fitting a cubic spline to the median-filtered trend of radial velocity with effective temperature (magenta and green lines in Figure 4.5 respectively). We then use this spline to assign a radial velocity correction to every star based on its effective temperature. No radial velocity correction is applied for stars hotter than 4000 K, where the correction is comparable to the statistical uncertainties.

This correction homogenizes the velocity zero-point at all temperatures to that of the stars hotter than 4000 K, however it does not guarantee that this velocity zero-point is accurate. On the one hand we measure radial velocities  $450 \pm 120 \text{ m s}^{-1}$  systematically *lower* than the RV standards from Prato (2007) from their NIRSPEC H-band spectra (Figure 4.5). On the other hand in the Pleiades we measure radial velocities  $400 \pm 60 \text{ m s}^{-1}$  systematically *higher* than the radial velocities measured for the same stars with CORAVEL (Mermilliod et al. 2009). The latter offset is consistent at the 2 sigma level with the radial velocity offset of  $602 \pm 116 \text{ m s}^{-1}$  found between the APOGEE radial velocity measurements and the CORAVEL velocity measurements for the same stars in Coma Ber (Terrien et al. 2014). We decided not to calibrate our radial velocities to either one of these systems, because of the different directions of the zero-point offsets with respect to the radial-velocity standards from Prato (2007) and Mermilliod et al. (2009). From these analyses we estimate a systematic uncertainty in the velocity zero-point on the order of  $0.5 \text{ km s}^{-1}$ .

### 4.3.2.3 Further systematic uncertainties

Here we study the accuracy of our fit to the effective temperatures and surface gravities from the APOGEE spectra. The offset between these effective temperatures and the ef-

ffective temperature values from several literature sources are plotted in Figure 4.6. The literature effective temperatures are mostly derived from visible spectroscopy and photometry, although a few are based on near-infrared spectral types. We will discuss the accuracy of the effective temperature for stars in three temperature ranges: cool stars with  $T_{\text{eff}} < 3800$  K, intermediate stars with  $3800 \text{ K} < T_{\text{eff}} < 5500$  K and hot stars with  $T_{\text{eff}} > 5500$  K

For the coolest stars ( $T_{\text{eff}} < 3800$  K) we find a temperature-dependent systematic offset ranging from -300 K to +300 K, when comparing our effective temperatures with the effective temperatures derived from visible and near-infrared spectral types in IC 348 by Luhman et al. (2003) and with the effective temperatures from dedicated red medium-band filters sensitive to TiO lines in Orion (Da Rio et al. 2012) (Figure 4.6). The strong agreement in the systematic offset in the effective temperatures relative to both Luhman et al. (2003) and Da Rio et al. (2012) implies that the effective temperature scale obtained from the APOGEE observations in the H-band using the BT-Settl grid disagrees with the conversion from spectral type to effective temperature from Luhman (1999). This conversion was both used in Luhman et al. (2003, except for a small change for  $T_{\text{eff}} < 2700$  K) and to calibrate the photometry to effective temperatures in Da Rio et al. (2012). The spectral types themselves are an unlikely origin of the systematic offset as they come from a wide variety of literature sources and have been derived from both visible and near-infrared spectra. Ignoring the systematic offset a scatter remains of only  $\sim 80$  K over this temperature range, which is in line with the precision of half of a spectral subtype claimed by Luhman et al. (2003) and Da Rio & Robberto (2012). A likely cause of this remaining scatter is the tendency of the best-fit effective temperatures to cluster around every other BT-Settl grid point in effective temperature (Figure 4.7). The APOGEE effective temperatures can be converted to the effective temperature scale from Luhman (1999) by:

$$T_{\text{Luhman (1999)}} = T_{\text{APOGEE}} - 0.5(T_{\text{APOGEE}} - 3200\text{K}), \quad (4.2)$$

where  $T_{\text{APOGEE}}$  is the measured effective temperature and  $T_{\text{Luhman (1999)}}$  is according to the temperature scale from Luhman (1999).

For hotter stars ( $T_{\text{eff}} > 3800$  K) the systematic offset becomes more loosely constrained. Although we seem to overestimate the effective temperature with  $\sim 300$  K with respect to literature values from the visible for a majority of stars at intermediate temperatures ( $3800 \text{ K} < T_{\text{eff}} < 5500 \text{ K}$ ), the scatter greatly increases in this temperature range. From this scatter we estimate uncertainties on the order of 300-500 K. For even hotter stars ( $T_{\text{eff}} > 5500$  K) the scatter with respect to literature values decreases somewhat, suggesting uncertainties of 100 - 200 K. The upper limit of the BT-Settl grid at 7000 K sets an upper limit to the effective temperature measured.

Finally we determine the accuracy of the measured surface gravities by comparing the observed effective temperature vs. surface gravity diagrams with those expected from isochrones (Figure 4.7). For the cooler stars ( $T_{\text{eff}} < 4500$  K) the stars in the different clusters clearly differ in their surface gravity and agree reasonably well with the Dartmouth isochrones at their respective ages. The increased spread and offset from the isochrones



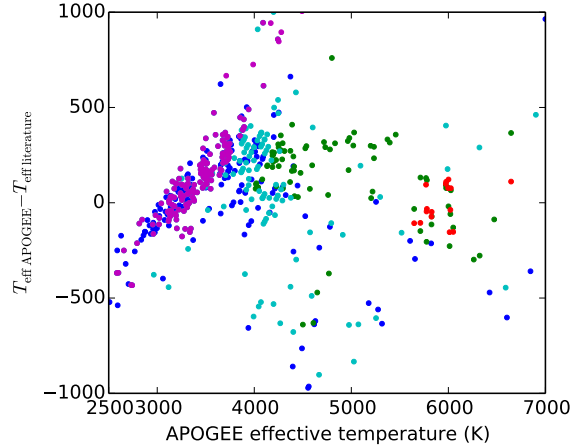


Fig. 4.6 — A comparison of the measured APOGEE/BT-Settl effective temperatures with literature values. Every dot represents the effective temperature of a star observed with APOGEE and a previous survey. Blue dots compare with the effective temperature in IC 348 derived from both visible and NIR spectral types from a variety of sources collected by Luhman et al. (2003). The green dots compare with the effective temperature in the Pleiades from visible echelle spectra from the Hamilton spectrograph on the Lick Observatory (Soderblom et al. 1993) and the red dots compare with similar data for solar-like stars in the Pleiades from Soderblom et al. (2009). The magenta dots compare with the effective temperatures in Orion A from deep visible photometry with dedicated medium-band filters (Da Rio et al. 2012). Finally the cyan dots compare with the effective temperatures in Orion collected by Nicola Da Rio from Hillenbrand (1997) and Hsu et al. (2012).

in surface gravities for hotter stars ( $T_{\text{eff}} > 4500$  K) again suggest a lower precision and accuracy for the hotter stars, although the older pre-main sequence stars in the Pleiades retain a higher surface gravity than those in the younger clusters.

#### 4.4 Stellar luminosities and masses

To study the dynamical state of IC 348, we need to determine the gravitational potential well, caused by the stars and gas in the young cluster. Before we can calculate the total mass we need to measure the interstellar extinction towards the stars observed in IC 348 (section 4.4.1), so that we can compute the stellar luminosities in section 4.4.2. We then use the Dartmouth pre-main sequence tracks (Dotter et al. 2008) to convert the spectroscopic temperatures and luminosities into stellar masses, which are combined with the gas mass in section 4.4.3 to compute the total mass distribution in IC 348.

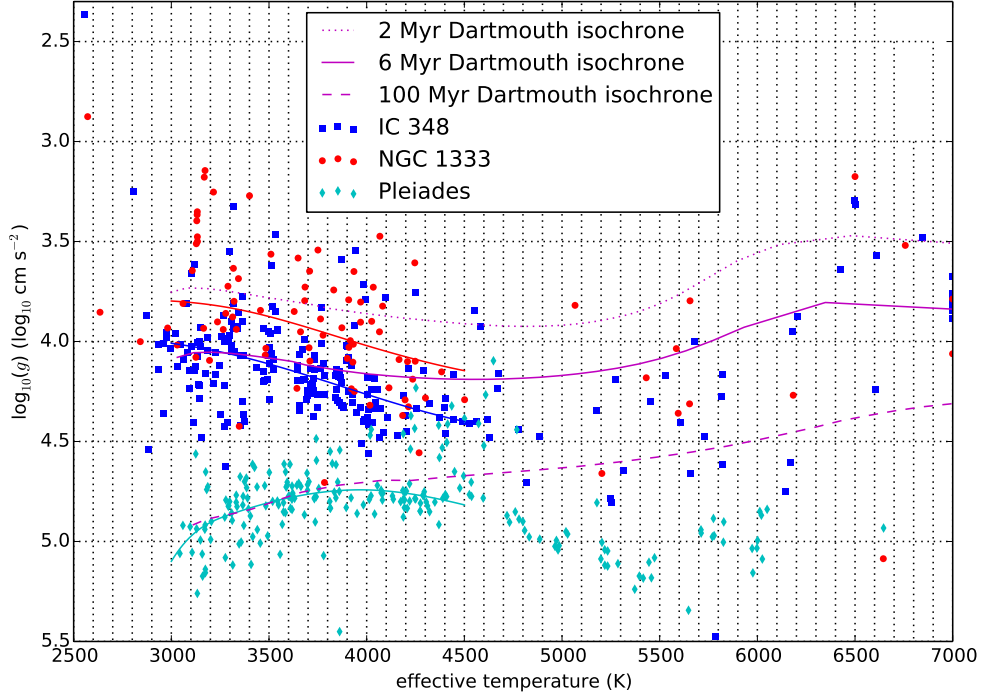


Fig. 4.7 — The distribution of spectroscopic effective temperatures and surface gravities (blue squares for IC 348; red circles for NGC 1333, and cyan diamonds for the Pleiades) with trend lines overplotted in the same color between 3000 and 4500 K. Only stars with  $\sigma_{\text{Teff}} < 100$  and  $\sigma_{\log(g)} < 0.1$  have been included for clarity. Overplotted in magenta are the Dartmouth isochrones (Dotter et al. 2008) at 2 Myr (dotted), 6 Myr (solid), and 100 Myr (dashed). The BT-Settl grid contains a model spectrum at every intersection of the black dotted lines and extends to lower effective temperatures and lower surface gravities than plotted here.

#### 4.4.1 Extinction

The extinctions to the observed young pre-main sequence stars have been derived from the excess redness in J-H with respect to a star in the Pleiades with the same effective temperature. Although the Pleiades at an age of  $\sim 110$  Myr is significantly older than the 1 - 5 Myr old clusters targeted in this survey, the cluster serves as an excellent calibrator due to its very low overall extinction and the targeting of the cluster by APOGEE, which means we can calibrate the colors in the Pleiades to the temperature scale found by APOGEE. For every Pleiades member with APOGEE spectra, we find the point on the single-star photometric locus for the Pleiades defined by Bell et al. (2012) with the smallest unweighted residuals in their visible and near-infrared photometry. These stars are then used to calibrate the spectroscopic effective temperature scale in this work to the colors

of the Bell et al. single-star photometric locus. The extinction towards every star in the younger clusters is computed from the excess J-H color with respect to the J-H color of the Pleiades single-star locus at the same spectroscopic effective temperature (Figure 4.8). An additional reddening of  $E(J-H) = 0.013$  is added to correct for the mean extinction of  $E(B-V) = 0.044$  in the Pleiades (e.g. Breger 1986)<sup>2</sup>, where we used the extinction law from Rieke & Lebofsky (1985).

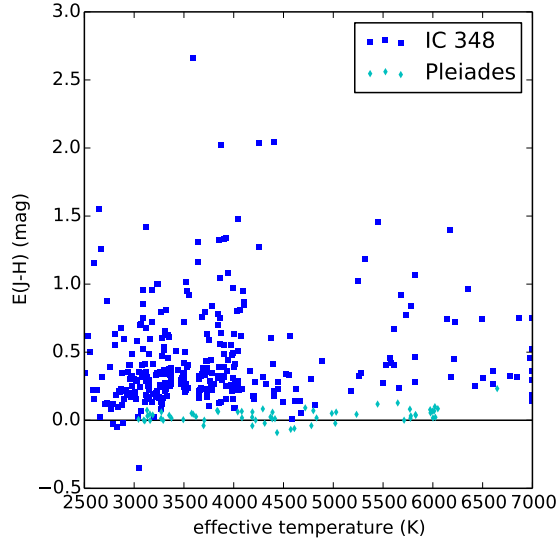


Fig. 4.8 — The reddening in J-H with respect to the Pleiades as a function of effective temperature in IC 348 (blue squares) and the Pleiades (cyan diamonds).

We test the accuracy of this procedure by considering a subset of spectroscopically observed stars in IC 348, which have visible photometry from Bell et al. (2013). Bell et al. (2013) observed many young clusters, including IC 348 and the Pleiades, using the visible griZ filters of the Wide Field Camera on the Isaac Newton Telescope (INT-WFC) (additional u-band photometry is available for some clusters). The single-star photometric locus from Bell et al. (2012), which we calibrated to our spectroscopic effective temperature above, contains the stellar magnitudes in the four griZ visible bands and the 2MASS JHKs bands. We can thus define the excess magnitude in all seven visible and near-infrared bands after extinction-correction for the subset of stars in IC 348 with both visible photometry from Bell et al. (2013) and APOGEE spectra. Figure 4.9 shows the resulting excess magnitude using the extinction estimates from the  $E(J-H)$  (i.e. how much brighter are the stars in IC 348 in apparent magnitude after extinction correction with respect to the stars with the same effective temperature in the Pleiades). The excesses in the visible and the J-band typically agree within several hundredth to tenths of a magnitude at least for stars with  $A_J < 1$  (red in Figure 4.9), suggesting that these photometric excesses are caused by changes in the solid angle that these stars cover on the sky, and not uncertainties

<sup>2</sup>The differential extinction in the Pleiades ( $A_V \sim 1.3$ ) caused by a CO cloud covering the southwest region of the cluster Breger (1987) is not taken into account in this analysis, because it only covers a very small part of the cloud.

in extinction. The scatter around the  $\Delta I = \Delta J$  line in Figure 4.9 puts an upper limit on the uncertainty in the extinction of 0.16 mag in  $A_J$ .

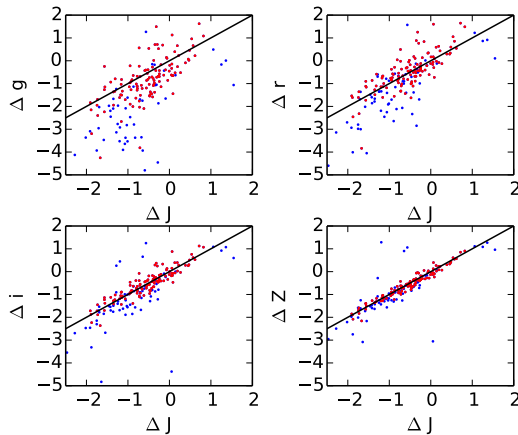


Fig. 4.9 — The excess magnitudes in various bands in IC 348 with respect to a single star with the same temperature in the Pleiades after extinction correction. We only include stars with the INT-WFC visible photometry in griZ from Bell et al. (2013). The black lines in each panel show perfect one-to-one agreement between the excess in the J-band and in the visible. The excess J-band magnitude with respect to the Pleiades correlates very well with the excesses in the visible bands, implying that the excess magnitude is color-independent. The stars have been separated by color into those stars with  $A_J > 1$  (blue) and  $A_J < 1$  (red).

#### 4.4.2 Stellar luminosities

After extinction-correction and adopting a distance modulus of 6.98 to IC 348 (Ripepi et al. 2014), we can derive the absolute magnitudes of the stars in IC 348. Figure 4.10 shows a J-band magnitude-temperature diagram. Similarly to Figure 4.7 we overplot the Dartmouth isochrones (Dotter et al. 2008). The spread in absolute magnitudes of the star suggest a somewhat younger age (1-10 Myr) than the surface gravities (2-10 Myr), which might be partly explained by an excess brightness due to binarity or a systematic offset in the surface gravities.

As previously pointed out by Luhman et al. (2003) and Muench et al. (2007), at any given effective temperature the stars in IC 348 show a broad spread in extinction-corrected J-band magnitude relative to the trend line with a standard deviation of 1 mag (Figure 4.10). Such a spread can be caused by a wide variety of sources, including photometric uncertainties ( $\sim 0.02$  mag), errors in the extinction ( $\sim 0.16$  mag), unresolved binary companions, differences in distance, contamination of background stars, and a real luminosity differences between the stars (Hartmann 2001; Reggiani et al. 2011). However, we find that each of these (as well as them all combined) is insufficient to explain the observed luminosity spread with photometric uncertainties of only about 0.02 mag in the 2MASS

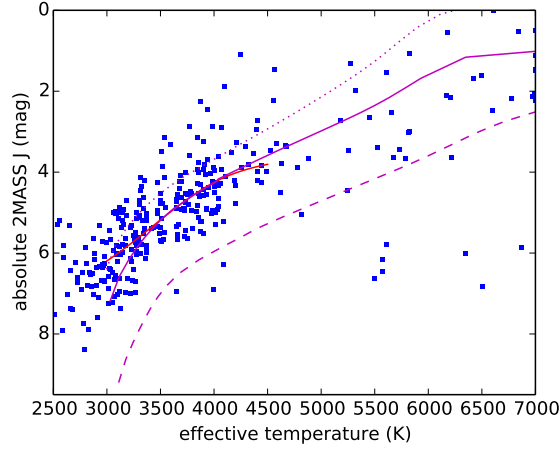


Fig. 4.10 — The absolute J-band magnitude as a function of spectroscopic effective temperature in IC 348 after extinction-correction, assuming a distance modulus of 6.98 with a trend line added in red. Overplotted are the same Dartmouth isochrones as in Figure 4.7 with the 2MASS J-band magnitude derived from PHOENIX synthetic fluxes (Dotter et al. 2008). From top to bottom the ages of the isochrones are 2 Myr (dotted), 6 Myr (solid), and 100 Myr (dashed).

J-band, uncertainties in  $A_J$  of  $\sim 0.16$  mag (see above), and a spread of 1 pc (twice the half-mass radius) in distance to the stars corresponding only to a shift in magnitude of 0.01 mag. The contribution of the binaries is larger, but even if 100% of the stars had unresolved binaries with a flat mass ratio distribution, this would only add 0.22 mag to the dispersion in J-band magnitudes. This suggests that the vast majority of the observed spread is caused by real luminosity differences (and hence radius differences) between stars of the same temperature, which could be caused by an age difference or differences in accretion history (e.g. Dunham & Vorobyov 2012; Baraffe et al. 2012).

If this luminosity spread is real, the brighter stars at any effective temperature should have a lower surface gravity due to their larger radius. To confirm this we plot in Figure 4.11 the extinction-corrected J-band magnitude and the surface gravity relative to other stars in IC 348 of the same effective temperature for stars hotter than 3000 K and cooler than 5000 K. Except for a single outlier with a measured surface gravity of -0.3, these parameters are strongly correlated (Pearson  $r = 0.59$  with a p-value of  $\approx 10^{-19}$  rejecting the null-hypothesis that the parameters are uncorrelated if the outlying star is ignored; the p-value increases to  $\approx 10^{-3}$  if the outlying star is included). Cooler and hotter stars do not appear to follow this correlation, which probably illustrates the larger uncertainties in the stellar parameters for these stars (see section 4.3.2.3). This correlation at intermediate temperatures (which contains most stars) indicates that brighter stars have a lower surface gravity, confirming that the excess brightness is indeed caused by a larger stellar size.

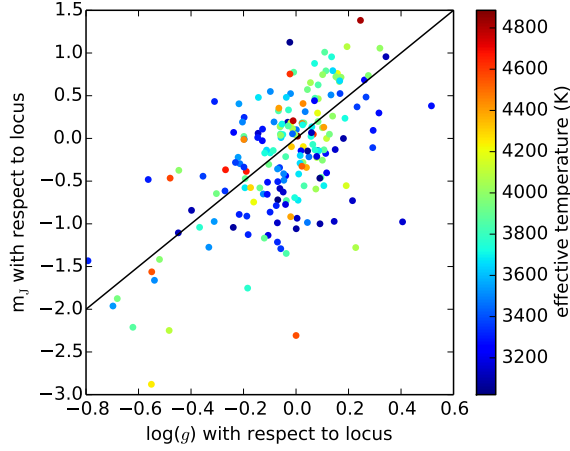


Fig. 4.11 — The J-band magnitude and in  $\log(g)$  relative to the trend lines plotted in Figure 4.7 and 4.10. Only stars with precise parameters ( $\sigma_{T_{\text{eff}}} < 100$  and  $\sigma_{\log(g)} < 0.1$ ) between 3000 and 5000 K have been included. A single star with very low surface gravity lies outside of this plot. The color coding indicates the spectroscopic effective temperature of the star. The black line illustrates  $\Delta J \propto 2.5\Delta \log(g)$  as expected for a single mass at every effective temperature.

#### 4.4.3 IC 348 cluster mass

We need an estimate of the stellar and gas mass of IC 348 to determine its virial state. In this section we derive the stellar mass in IC 348. We will only consider stars more massive than  $0.25 M_{\odot}$  (i.e. hotter than  $\sim 3300$  K), because these are typically brighter than H=13 for which our target catalogue of potential members seems to be complete (see completeness analysis in section 4.2.1 and Figure 4.1).

First we derive the stellar mass of the stars with APOGEE spectra using the spectroscopic effective temperature and extinction-corrected absolute J-band magnitude from the Dartmouth isochrones (see Figure 4.10). For the stars with a spectroscopic masses above  $0.25 M_{\odot}$  the total mass adds up to about  $125 \pm 20 M_{\odot}$ , where the uncertainty comes from an assumed systematic uncertainty of 200 K on the effective temperature.

We then extend this mass estimate to the unobserved stars in the target catalogue. We assume that these unobserved stars have the same properties as the observed stars at the same *apparent* H-band magnitude, because the priority in the targeting was based on this magnitude. For every unobserved star we select the 20 stars with the most similar apparent H-band magnitude and randomly assign one of their masses to the unobserved star. On average this leads to an additional mass of  $35 \pm 6 M_{\odot}$  for cluster members with a mass above the  $0.25 M_{\odot}$ . Hence we estimate the total cluster mass for stars more massive than  $0.25 M_{\odot}$  to be  $160 \pm 25 M_{\odot}$ .

Finally we estimate how much of the total cluster mass we missed by assigning a min-

imum stellar mass of  $0.25 M_{\odot}$ . For this we use the initial mass function (IMF) from Maschberger (2013), which has been designed to match the classical IMFs from Kroupa (2001) and Chabrier (2003, 2005), but has the advantage of consisting of a single continuous function. By integrating this IMF with the default parameters from Maschberger (2013) we find that stars with masses below  $0.25 M_{\odot}$  contribute 17% of the initial total mass. Correcting for this implies a final total stellar mass in IC 348 of  $192 \pm 31 M_{\odot}$ . The distribution of this mass has been plotted in Figure 4.12 together with the mass contribution from several gas tracers. Throughout this work we will use the mass estimate of the dust emission from Herschel.

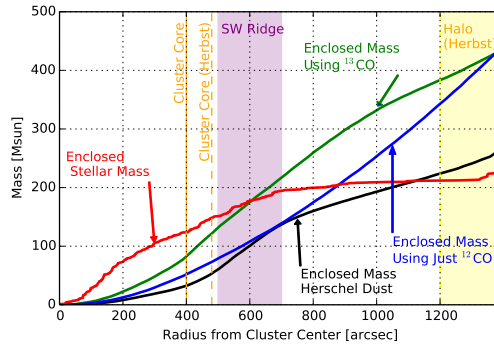


Fig. 4.12 — The enclosed stellar and gas mass in IC 348 as a function of distance from the cluster center. For the gas mass estimates from the Herschel dust emission maps,  $^{12}\text{CO}$  maps, and  $^{13}\text{CO}$  maps have been included. The core and halo radius of Herbst (2008) have been marked together with the half-mass radius at 300 arcseconds. The dense gas clump called the southwestern ridge extends from 500 to 700 arcseconds to the south of IC 348.

## 4.5 Results

Here we analyze the radial velocities observed in IC 348 to constrain the clusters dynamical state. In section 4.5.1 we find a velocity dispersion of  $0.75 \pm 0.05 \text{ km s}^{-1}$  in IC 348 after correction for the radial velocity offsets due to binary orbital motions. In section 4.5.2 we show a trend between stellar extinction and radial velocity, which suggests that IC 348 might be collapsing. In section 4.5.3 we search for trends of the velocity distribution with the position in the cluster. Finally in section 4.5.4 we discuss whether the velocities in IC 348 are spatially correlated. Unless otherwise noted we will only consider stars that do not show radial velocity variability (see section 4.5.1), have an uncertainty on the mean radial velocity of less than  $500 \text{ m s}^{-1}$ , and are within 800 arcseconds (i.e. two half-mass radii) from the cluster center. The velocities used throughout this section are those corrected for the unphysical radial velocity offset at low effective temperatures (see section 4.3.2.2). In the current fits a significant fraction of the stars is rejected as RV variable, because the radial velocity failed to converge. This will be fixed in Cottaar et al. (in prep).

### 4.5.1 Global velocity dispersion

The observed radial velocity distribution is not only influenced by the stellar motions through the cluster’s potential, but also by orbital motions of members of a binary. The multiple epochs over which APOGEE spectra were taken allows the binaries with short periods to be detected through their radial velocity variations. However, many binaries with velocity amplitudes comparable to or larger than the velocity dispersion of IC 348 remain undetected, broadening the observed radial velocity distribution.

We statistically correct for the effect of these binary orbital motions using the procedure outlined in Cottaar et al. (2012b) and Cottaar & Hénault-Brunet (2014). In short, we exclude from the analysis all stars with variable radial velocities (i.e. inconsistent with being single at the  $p < 10^{-4}$  level according to a  $\chi^2$ -test). For the remaining stars we compute the distribution of radial velocity offsets due to binary orbital motions by (1) drawing in a Monte Carlo like fashion a large number of binary orbits, (2) discarding those binary orbits that would have been detected given the observational details of that star, and (3) computing the distribution of radial velocity offsets between the observed and systematic velocities for the remaining binaries. This radial velocity offset distribution due to binary orbital motions is then convolved with the intrinsic velocity distribution of the cluster (assumed to be Gaussian in this work) and used to compute the likelihood of the observed velocity of that star. The best-fit parameters are found by maximizing the total likelihood of reproducing all observed velocities. All quoted uncertainties in the mean velocity and velocity dispersion of the cluster have been computed using an MCMC simulation.

For this procedure to work we need to draw many random binary orbits and hence we need to assume a period, mass ratio, and eccentricity distribution for the observed stars. We are mainly interested in the number of binaries with periods between tens and thousands of years, whose binary orbital motions cause velocity offsets on the order of the velocity dispersion of IC 348. The binary distribution in this period range has only been extensively characterized in the solar neighbourhood (see review from Duchêne & Kraus 2013), so we will use these results to inform our assumed orbital parameter distributions. First we assign to every star an age and a mass based on the Dartmouth tracks and its position in the temperature-magnitude diagram (see Figure 4.10). The binary fraction, the peak of the semi-major axis distribution, and the width of semi-major axis distribution all decrease towards lower masses (e.g. Lada 2006; Janson et al. 2012). For brown dwarves we set the binary fraction to 22% (Burgasser et al. 2007). Above the hydrogen burning limit we let the binary fraction increase linearly, so that the binary fraction at one solar mass is 44% (Raghavan et al. 2010). We implement the period distribution as three log-normals, with a mean of  $\log a_0 = 0.86$  and a width of  $\sigma_{\log a} = 0.24$  below  $0.2 M_{\odot}$  (Burgasser et al. 2007), with  $\log a_0 = 1.2$  and  $\sigma_{\log a} = 0.8$  between  $0.2 M_{\odot}$  and  $0.8 M_{\odot}$  (Janson et al. 2012), and with  $\log a_0 = 1.64$  and  $\sigma_{\log a} = 1.52$  above  $0.8 M_{\odot}$  (Raghavan et al. 2010). We adopt a flat mass ratio distribution (Reggiani & Meyer 2013) and flat eccentricity distribution (Duchêne & Kraus 2013).



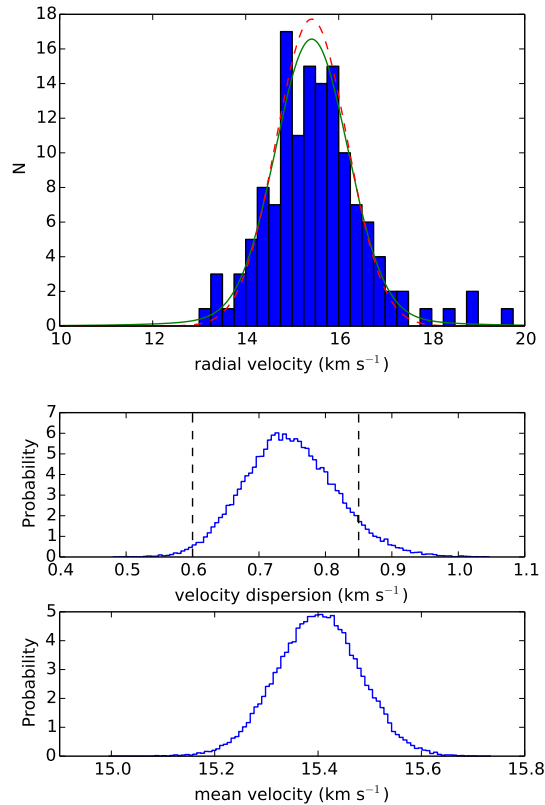


Fig. 4.13 — Upper panel: the radial velocity distribution of stars that are not RV variable, are within 0.2 deg from the cluster center, and have a radial velocity precision of  $< 0.5 \text{ km s}^{-1}$  (histogram), with an approximation of the best-fit radial velocity distribution including the effect of binary orbital motions (green solid line) and the best-fit underlying Gaussian velocity distribution corrected for binary orbital motions (red dashed line). Lower panels: posterior probability distributions in the velocity dispersion and the mean velocity.

Figure 4.13 shows a histogram of the observed velocity distribution with an approximation of the best-fit distribution including the velocity offsets due to binary orbital motions. This best-fit distribution is only an approximation appropriate for a typical star, because the probability distribution varies for every star in the maximum-likelihood analysis, because it depends on the velocity uncertainty and on the timescale over which the star was observed. The Gaussian underlying velocity distribution corresponding to this best-fit is also overplotted in Figure 4.13 (and is the same for all stars). A MCMC simulation gives a velocity dispersion of  $0.75 \pm 0.05 \text{ km s}^{-1}$  and mean velocity of  $15.40 \pm 0.08 \text{ km s}^{-1}$ .

#### 4.5.2 Velocity gradient with extinction

Ignoring for a moment local circumstellar material, the extinction measures how deep a star is embedded within the gas in IC 348, and if the gas is roughly uniformly distributed it gives

us an indication of which stars are closer and further away from us along the line of sight. This would suggest that collapse or expansion of IC 348 might be directly detected through a correlation between the radial velocity and extinction of a star. To test this scenario we divide the population of IC 348 into three subpopulations. One subpopulation contains all stars with reddening in J-H corresponding to  $A_J > 1$ , which is a higher extinction as expected for the background stars based on extinction maps or the Herschel dust maps. This implies that these stars either have excess extinction due to dense gas surrounding the star along the line of sight (e.g. envelope or circumstellar disc) or they might have an other source of reddening in their J-H color, such as emission from an inner protoplanetary disc. Either way, the reddening observed for these stars is likely to be unrelated to the position within the cluster and hence no correlation with radial velocities is expected. The remaining low-extinction stars are divided into two roughly equal-size subpopulations (with  $A_J < 0.65$  and  $A_J > 0.65$ ). The radial velocity distributions of these three populations have been plotted in the upper panel in Figure 4.14. The radial velocity distributions for the low-extinction and intermediate-extinction populations are significantly different ( $p = 10^{-4}$ ). In the same manner as for the global velocity dispersion (section 4.5.1) we derive a mean velocity and velocity dispersion for the three subpopulations corrected for binary orbital motions. The resulting probability distributions on the mean velocity and velocity dispersion are shown in Figure 4.14. We find that the stars with intermediate extinction are more blue-shifted at the 3-sigma level than the low-extinction sample. This implies that the stars in the cluster are moving towards each other along the line of sight, which corresponds to collapse along this dimension. The stars with high extinction have an intermediate mean velocity and velocity dispersion, suggesting that they are a mixture of the two other subpopulations, which is expected if the extinction for these stars is indeed uncorrelated with the location in the cluster.

### 4.5.3 Spatial dependence of the velocity distribution

In globular clusters the radial velocity dispersion is often found to drop steeply with increasing cluster radius (e.g. Watkins et al. 2013) as expected from the Jean's equation. We use the same method used to test the velocity gradient with the extinction (section 4.5.2) to find if such a trend with radius is also present in IC 348.

The upper panel in Figure 4.15 shows the velocity distribution as a function of distance from the cluster center, separated into those stars within a half-mass radius ( $\approx 0.1$  deg), between one and two half-mass radii, and those stars beyond two half-mass radii. There is a suggestive drop in the velocity dispersion towards the edge of the cluster, although it is not statistically significant (Figure 4.15). Neither is the apparent blueshift for the cluster at the edge.

The cluster does not show any obvious rotation (upper panel of Figure 4.16), although a small rotation is found with the mean velocity slightly increasing from the northeast to the southwest (middle panel of Figure 4.16). To determine the significance of this trend, we add the possibility of a velocity gradient to the assumed Gaussian velocity distribution

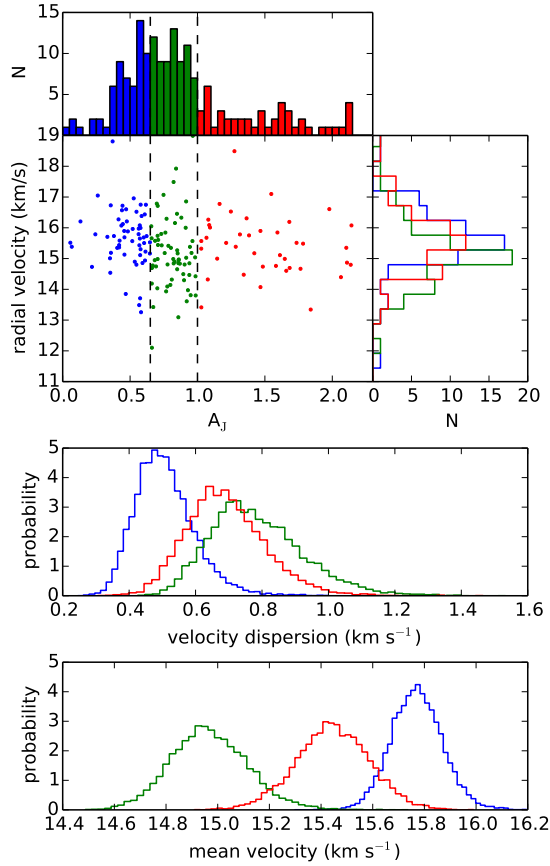


Fig. 4.14 — (upper) Scatter plot of the radial velocity distribution versus stellar extinction with their histograms. The stars have been split into three subpopulations based on stellar extinction ( $A_J < 0.65$  in blue;  $0.65 < A_J < 1$  in green; and  $A_J > 1$  in red). (lower) The probability distribution of the velocity dispersion and mean velocity of the three subpopulations. We find a significant offset between the stars with  $A_J < 0.65$  (blue) and  $0.65 < A_J < 1$  (green).

(see section 4.5.1) through the replacement of the global mean velocity with a different mean velocity for every star given by:

$$\mu_i = v_{\text{rot}} \frac{r_i}{r_{\text{hm}}} \cos(\theta_i - \alpha) + \mu, \quad (4.3)$$

where  $r_i$  and  $\theta_i$  are the positions for star  $i$  in circular coordinates around the cluster center,  $v_{\text{rot}}$  is the change in the mean velocity across a half-mass radius  $r_{\text{hm}} = 0.1$  deg,  $\alpha$  is the angle of the rotation axis, and  $\mu$  is the global mean velocity.

The lower panel in Figure 4.16 illustrates the distribution of the MCMC, when fitting such a velocity gradient. Although the uncertainties on both the rotational velocity and the angle of rotation are large, in 93% of the simulations in the Markov chain there is a positive velocity gradient from the northeast to the southwest, suggesting that there is a

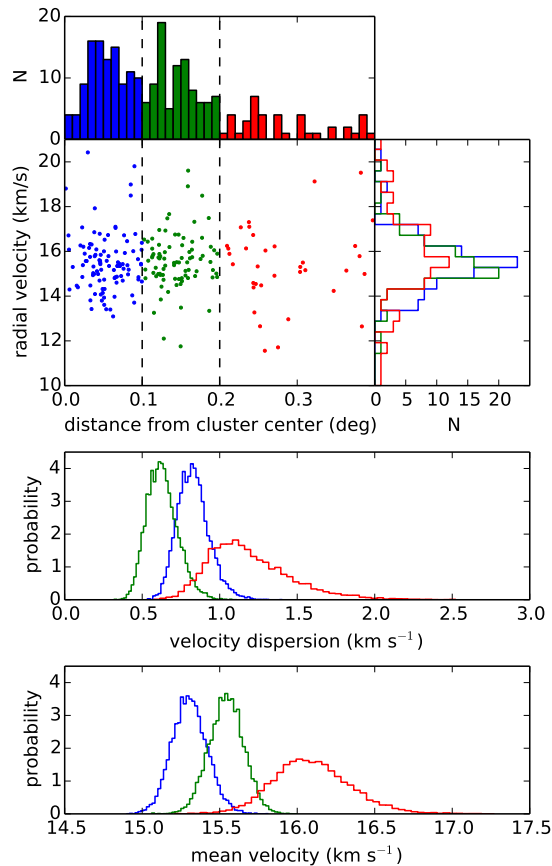


Fig. 4.15 — (upper) Scatter plot of the radial velocity distribution versus the distance from the cluster center with their histograms. The stars have been split into three subpopulations based on distance from the cluster center ( $d < 0.1$  deg in blue;  $0.1 \text{ deg} < d < 0.2$  deg in green; and  $d > 0.2$  deg in red). (lower) The probability distribution of the velocity dispersion and mean velocity of the three subpopulations. We do not detect a significant shift in the mean radial velocity or velocity dispersion as a function of distance from the cluster center.

real gradient in this direction.

#### 4.5.4 Spatially correlated velocities

In the statistical analysis of the significance of the spatial trends of the velocity distribution discussed above, an implicit assumption was made that every star represented a random, independent draw of the velocity distribution. However, stars form from a turbulent molecular cloud in which the velocities are strongly spatially correlated (Larson 1981; Heyer & Brunt 2004). Here we check whether the stellar velocities in IC 348 are still spatially correlated, even though most stars will probably have completed some orbits.

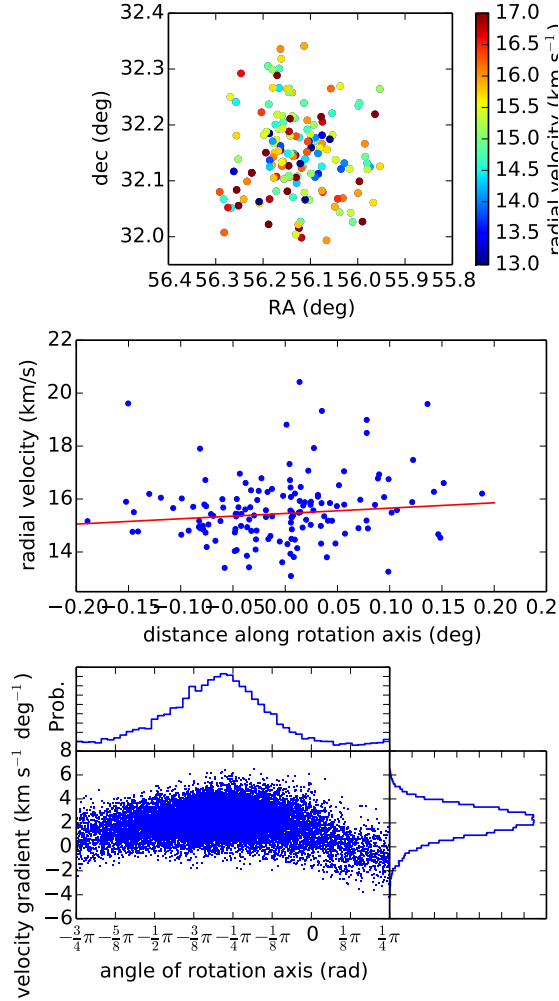


Fig. 4.16 — Spatial distribution of stars in IC 348, colored by their radial velocity (upper panel); the best-fit velocity gradient along a rotation axis from the northeast to the southwest (middle panel); and the probability distribution of the angle of rotation and the size of the velocity gradient (lower panel).

We test this correlation by computing the velocity differences between all stars and sorting them into equal-sized bins based on the projected distances between the stars. Figure 4.17 shows for every bin the dispersion in velocity differences after cutting any velocity differences bigger than  $4 \text{ km s}^{-1}$  to minimize the effect of binary orbital motions. The dispersions are significantly higher than the global velocity dispersion (see section 4.5.1), because the dispersion is not properly corrected for binary stars and the dispersion is computed for the velocity differences rather than the velocities, leading to an increase of  $\sqrt{2}$ . Although the dispersion in molecular clouds increases by a factor of 4.5 as the distance scale goes up by a factor of 10 (Heyer & Brunt 2004), we find that over the same increase in distance scale the stars show barely any increase in the velocity dispersion with an upper limit of  $\sim 10\%$  suggested by the scatter. From this we conclude that there is no

significant correlation left in the velocities between neighboring stars in IC 348.

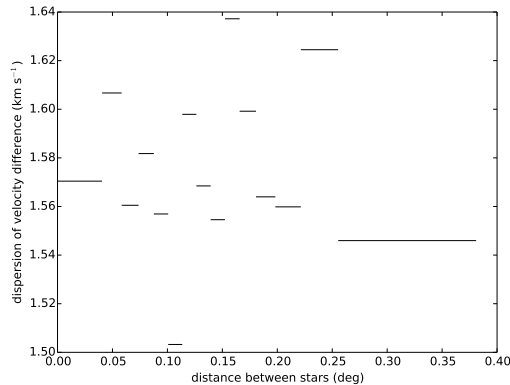


Fig. 4.17 — The dispersion of the velocity differences of stars with a projected separation in the range given by the length of the lines along the x-axis after cutting all velocity differences bigger than  $4 \text{ km s}^{-1}$  showing no obvious trend. Every bin contains about 3270 velocity differences between stars.

## 4.6 Discussion

### 4.6.1 Virial equilibrium

Although IC 348 is not deeply embedded in the Perseus molecular cloud, its young age suggests that the molecular gas in the cluster has only recently dissipated. The loss of the molecular gas causes the gravitational potential to decrease, which can cause the stellar cluster to unbind (e.g. Hills 1980; Lada et al. 1984; Goodwin & Bastian 2006). Even though the low star-formation efficiency in molecular clouds implies that a large fraction of the total gravitational potential is lost during the dispersal of the molecular cloud, the effect on the boundedness of the stars might be limited if they reside in regions with relatively little gas due to stellar accretion and contraction of the star cluster (e.g. Kruijssen et al. 2012).

To determine whether IC 348 is expected to expand we compare the measured velocity dispersion of  $0.75 \pm 0.05 \text{ km s}^{-1}$  to the velocity dispersion needed for virial equilibrium (assuming spherical symmetry), which is given by:

$$\sigma_{\text{dyn}} = \sqrt{\frac{GM}{\eta r_{\text{hm}}}}, \quad (4.4)$$

where  $G$  is the gravitational constant,  $M$  is the total stellar plus gas mass, which adds up to about  $350 M_{\odot}$  within the cluster’s outer radius of about 700 arcseconds (Figure 4.12),  $r_{\text{hm}}$  is the half-mass radius, which for a distance of 270 pc (Ripepi et al. 2014) is 0.4 pc, and

$\eta \approx 10$  is a structural parameter that depends on the density distribution (e.g. Portegies Zwart et al. 2010). Entering these values in equation 4.4 we find a velocity dispersion of  $0.6 \text{ km s}^{-1}$  for Virial equilibrium, while a cluster with a velocity dispersion  $\sqrt{2}$  higher (i.e.  $0.85 \text{ km s}^{-1}$ ) would have enough energy to unbind. The measured velocity dispersion represents a convolution of both random and the structured motions of the observed velocity gradient with extinction and across the cluster. We do not attempt to remove these structured motions, as they contribute to the total velocity dispersion and need to be included in the calculation of virial equilibrium in an equal manner as the random motions (Binney & Tremaine 2008).

We can reject a velocity dispersion of  $600 \text{ m s}^{-1}$  or lower at the 98% level, implying that IC 348 is supervirial. On the other hand an unbound state ( $> 0.85 \text{ km s}^{-1}$ ) is rejected at the 90% level, so IC 348 should be able to regain virial equilibrium through expansion. At present the stellar mass ( $244 M_{\odot}$ ) is likely to be insufficient to keep the cluster bound, so if the cluster were to lose a large fraction of its gas (or stellar) mass before it is able to revirialize, the cluster would likely become unbound and disperse.

#### 4.6.2 Signature of collapse

Up to  $A_J = 1$  the stars more deeply embedded in IC 348 seem to be preferentially blueshifted with respect to the less embedded stars (see section 4.5.2). Because the spatial information we get through the stellar extinction is in the same direction as the radial velocity, this implies that the more deeply embedded stars in the back of the cluster are moving towards the less deeply embedded stars in the front of the cluster, which indicates that the cluster is collapsing along the line of sight. Here we will discuss several scenarios to explain this trend, focusing on (1) IC 348 being in global collapse along all three dimensions, (2) two clumps of stars with correlated velocities are moving towards each other, and (3) the trend is caused by a systematic offset in the observed radial velocities.

The first scenario for the radial velocity trend we discuss is that the cluster is actually collapsing. This is very unlikely to be the remnants of an initial collapse, because at an age of 3 to 6 Myr (Luhman et al. 2003; Bell et al. 2013) the cluster is already many free-fall times ( $\approx 2 \times 10^5 \text{ yr}$ ) old. However, instigating collapse at a later stage seems unlikely, because the gas mass binding the cluster together is constantly decreasing, which should lead to expansion. The velocity dispersion also suggests a slightly supervirial state. A possible scenario to explain all these observations is that the cluster is currently revirializing after a large departure from virial equilibrium a few dynamical times ago (i.e. within  $\sim 1 \text{ Myr}$ ), which could be caused by a large ejection of gas. N-body simulations show that such clusters often show dampened fluctuations around virial equilibrium, with alternate phases of expansion and contraction (e.g. Goodwin & Bastian 2006). IC 348 could be in a contracting phase, which is currently transitioning to an expanding phase due to its supervirial state. A more detailed comparison with N-body simulations are required to test whether the speed of contraction and the size of the supervirial state are consistent with the simulations, but that is beyond the scope of this chapter.

Alternatively the radial velocity trend could not be a sign of global collapse, but merely reflective of two (or more) clumps of stars with correlated velocities with the more deeply embedded clump blueshifted with respect to the less deeply embedded clump of stars. This scenario would require a very high spatial overlap of these clumps when projected on the sky to explain the small size of any velocity trends in the plane of the sky (see section 4.5.3). This scenario also seems inconsistent with the lack of correlation seen in the velocities along the plane of the sky (see section 4.5.4), which suggests that IC 348 is already well mixed.

Finally we consider whether the radial velocity offset could be caused by the spectral analysis, potentially caused by diffuse interstellar bands biasing the radial velocities or a bias towards lower mass stars only being observed at low extinctions. This seems unlikely as the same trend is not observed in the other young clusters. This might be partly related to the smaller sample size in NGC 1333, the lack of highly extinguished stars in the Pleiades, and the larger velocity dispersion in Orion and NGC 2264.

Every scenario proposed here requires some finetuning, either temporal if the cluster is revirializing, or in the angle of observations if the trend reflects the relative velocity between two clumps of stars. The former scenario seems more likely, especially because large deviations from virial equilibrium could have happened in the recent past due to the dispersal of the molecular cloud out of which IC 348 formed. Future proper motion observations should be able to distinguish between these scenarios by looking for collapse in the plane of the sky.

In reality the correlation between extinction and distance along the line of sight is expected to be weak, due to the non-uniform, filamentary nature of molecular clouds (André et al. 2010). This suggests that the correlation between line-of-sight position and line-of-sight velocity might be even stronger than found between the extinction and the line-of-sight velocity, as the scatter increases, when line-of-sight positions are converted into extinction measurements.

## 4.7 Conclusions

Here we present the spectral analysis of young stars observed in the clusters IC 348, NGC 1333, NGC 2264, Orion, and the Pleiades with the high-resolution, multi-object spectrograph APOGEE. Tables with the stellar properties for IC 348 and the Pleiades have been included electronically. Radial velocities have been found with a typical precision of a few  $100 \text{ m s}^{-1}$ , although a systematic offset was found for the coolest stars ( $T_{\text{eff}} < 3500 \text{ K}$ ) in the sample, for which we correct. For these cool stars the effective temperatures also show a systematic offset with respect to the effective temperature scales from low-resolution spectra in IC 348 (Luhman et al. 2003) and visible medium-band photometry in Orion (Da Rio et al. 2012). Once corrected the effective temperatures agree with the previous estimates within  $\sim 100 \text{ K}$  for stars cooler than  $4500 \text{ K}$ , although larger offsets of up to



300 K are found for hotter stars. Finally the surface gravities agree reasonably well with the isochrones with again a better agreement for the cooler stars. The precision in surface gravities suffices to confirm the luminosity spread in the young cluster IC 348.

In addition we discuss the dynamical state of IC 348. When compared with the gravitational mass we find that IC 348 is slightly supervirial, but most likely bound, although the stellar mass is insufficient to keep the cluster bound if it does not revirialize before expelling the rest of the gas. We also find a blueshift for more deeply embedded stars compared to less deeply embedded stars, suggestive of a collapse in IC 348. We propose that this could be reconciled with the supervirial state of IC 348 if the cluster is currently revirializing, as expected if it recently ejected a significant portion of the molecular cloud out of which the cluster formed.

## Acknowledgments

I would like to thank Kevin Covey for leading the IN-SYNC collaboration, organizing its regular telecons, and for the many discussions on both the spectral analysis pipeline and the science. I would also want to thank Michael Meyer, Jonathan Tan, Jonathan Foster, David Nidever, and all the others on the IN-SYNC team for their helpful discussions. Finally I would like to thank the Sloan Digital Sky Survey III (SDSS-III) for deciding to start observing young stellar regions and allow me (as an external collaborator) to lead the analysis.

Funding for the SDSS and SDSS-II has been provided by the Alfred P. Sloan Foundation, the Participating Institutions, the National Science Foundation, the U.S. Department of Energy, the National Aeronautics and Space Administration, the Japanese Monbukagakusho, the Max Planck Society, and the Higher Education Funding Council for England. The SDSS Web Site is <http://www.sdss.org/>.

The SDSS is managed by the Astrophysical Research Consortium for the Participating Institutions. The Participating Institutions are the American Museum of Natural History, Astrophysical Institute Potsdam, University of Basel, University of Cambridge, Case Western Reserve University, University of Chicago, Drexel University, Fermilab, the Institute for Advanced Study, the Japan Participation Group, Johns Hopkins University, the Joint Institute for Nuclear Astrophysics, the Kavli Institute for Particle Astrophysics and Cosmology, the Korean Scientist Group, the Chinese Academy of Sciences (LAMOST), Los Alamos National Laboratory, the Max-Planck-Institute for Astronomy (MPIA), the Max-Planck-Institute for Astrophysics (MPA), New Mexico State University, Ohio State University, University of Pittsburgh, University of Portsmouth, Princeton University, the United States Naval Observatory, and the University of Washington.

## 5 | Conclusions

### 5.1 Summary

In this thesis we probed the dynamical state of young star clusters using their radial velocities in an effort to determine their dynamical evolution. A crucial step towards this goal was the development of a statistical tool to correct the observed radial velocity distribution for binary orbital motions. This was achieved by fitting a model distribution including the effects of binary orbital motions to the observed velocity distribution (chapter 2). Although the main advantage of this procedure lies in the possibility of reproducing the velocity dispersion with only a single epoch of radial velocities (Cottaar et al. 2012b), we also show that the accuracy of the measured velocity dispersion can benefit from multi-epoch radial velocities, if the binary properties are poorly characterized (Cottaar & Hénault-Brunet 2014). However, multi-epoch observations only noticeably increase the accuracy of the measured velocity dispersion, if the ratio of the measurement uncertainties and the baseline is small enough to detect the velocity gradients of the spectroscopic binaries, whose binary orbital motions cause velocity offsets similar to the velocity dispersion.

In chapter 3 we showed using the multi-epoch radial velocities of only five yellow hypergiants and one luminous blue variable, that the young massive cluster Westerlund I has an upper bound to the velocity dispersion of  $\sigma = 2.1_{-0.9}^{+3.4} \text{ km s}^{-1}$  (Cottaar et al. 2012a). This velocity dispersion was surprisingly low given the mass of the cluster, suggesting that Westerlund I is subvirial, although the velocity dispersion is also consistent with virial equilibrium. We can rule out that the cluster is unbound. Due to the small sample size, we could not study the dynamics in Westerlund I in more detail.

The situation was very different for IC 348, where the Sloan Digital Sky Survey took thousands of H-band high-resolution spectra of 339 young pre-main sequence stars, many of which have as many as 13 spectra taken (only 10 of which have been analyzed at the

time of this writing) over a baseline of more than a year. These spectra were analyzed together with spectra taken in four other young stellar groups, to retrieve highly accurate estimates of the stellar parameters using a custom spectral analysis pipeline. The surface gravities, for instance, were measured precisely enough to detect a spread in stellar sizes in IC 348. IC 348 showed a much smaller velocity dispersion than Westerlund I of  $0.75 \pm 0.05$  km s<sup>-1</sup>. However, because this cluster is much smaller than Westerlund I, this still only implies that the cluster is barely supervirial, but still bound. This velocity dispersion is not caused purely by random motions, but also by structured motions. We report a tentative detection of a small velocity gradient across the cluster, and a larger velocity gradient as a function of extinction. The orientation of the latter gradient suggest the stars in IC 348 are moving towards each other along the line of sight, which implies collapse.

## 5.2 Are young massive stellar groups bound?

Using these results, we can now address the first question asked in the introduction: do dense, young stellar groups emerge bound from their natal cloud? We will first address the dynamical state of young massive stellar groups. Unresolved stellar groups in other galaxies often appeared to have large velocity dispersions compared to their masses and hence appeared to be unbound, even if they are dense like a cluster (e.g. Bastian et al. 2006; Goodwin & Bastian 2006), which makes the result of a bound state of Westerlund I seem suprising. Over the past few years, several more studies have reported that resolved young massive clusters are bound. Hénault-Brunet et al. (2012a) used multi-epoch radial velocities to argue that the velocity dispersion in the young massive cluster R136 is only about 5 km s<sup>-1</sup> (see also Cottaar & Hénault-Brunet 2014), which suggests that this cluster is also bound. Clarkson et al. (2012) similarly used proper motions for the young massive cluster Arches finding a velocity dispersion of only  $5.4 \pm 0.4$  km s<sup>-1</sup>, a factor of two lower than expected from their mass estimate of  $(4 - 6) \times 10^4 M_{\odot}$ . Finally Rochau et al. (2010) measured a velocity dispersion of  $4.5 \pm 0.8$  km s<sup>-1</sup> in NGC 3603, somewhat larger than expected from the photometric mass of 10,000 to 16,000  $M_{\odot}$ , however the data is consistent with being in virial equilibrium.

All four of these clusters are very young (only a few Myr old with Westerlund I being the oldest), very massive (containing more than  $10^4 M_{\odot}$  of stars), and appear to be (mostly) bound, as opposed to the unresolved clusters in other galaxies. The most likely reason for this difference is that the velocity dispersion observed in unresolved clusters is inflated by binary orbital motions (Kouwenhoven & de Grijs 2008; Gieles et al. 2010b) or the strong spectral variability caused by large-scale motions in the atmospheres of massive stars. In the resolved clusters these effects can be corrected for, either by multiple epochs of radial velocity observations used to identify the RV-stable stars (as for Westerlund I and R136) or by proper motions, which are less sensitive to binaries and not sensitive to the spectral variability (as for NGC 3603 and Arches). Alternatively Mengel et al. (2002) suggested that the unresolved clusters could be more massive than suggested by their brightness, if

they contained an excess of low-mass stars<sup>1</sup>. However, so far no direct evidence of such variations in the distribution of stellar masses has been found (Bastian et al. 2010) and this overabundance of low-mass stars is the exact opposite of what Clarkson et al. (2012) proposed to explain the low velocity dispersion they measured in the Arches cluster.

As argued in the introduction for a stellar group to remain bound after expulsion of the stellar cluster, either requires a high local star-formation efficiency (Kruijssen et al. 2012) or a dynamically cold stellar group at the time of the ejection (Goodwin 2009). This could be caused by massive, dense clouds either having a much higher star-formation efficiency than local clouds or by having stars form subvirially in these clouds, which will allow them to collapse to a relatively star-rich region in the center of the cloud or even still be dynamically cold at the time of the gas expulsion.

### 5.3 Are low-mass young stellar groups bound?

We now turn our attention to low-mass stellar groups forming in the solar neighbourhood. In addition to the results for IC 348 (chapter 4) we will here also add results from the Gaia-ESO large public spectroscopic survey. This survey aims to retrieve high-resolution visible spectra of more than  $10^5$  stars in order to understand the chemodynamical evolution of our own galaxy (Gilmore et al. 2012). Many different stellar components of our Galaxy have been targeted and will be targeted over the coming years, including some young, dense stellar groups. As part of our involvement in this collaboration, we analysed the dynamics of two of these young regions.

Chamaeleon I is a well-studied local star-forming region with an age of  $\sim 2$  Myr and more than 300 stars (Luhman 2008; Lopez Martí et al. 2013). Radial velocities for 34 stars and brown dwarfs had been previously measured in Chamaeleon I (e.g. Dubath et al. 1996; Joergens & Guenther 2001; Joergens 2006) and have been collected and analysed by Joergens (2006), who found a velocity dispersion of about  $0.9 \text{ km s}^{-1}$  for the very low mass stars and brown dwarfs and  $1.3 \text{ km s}^{-1}$  for the more massive pre-main sequence stars. Corrected for binary orbital motions, the Gaia-ESO radial velocities in Chamaeleon I have a velocity dispersion of  $1.0 \pm 0.2 \text{ km s}^{-1}$  (Figure 5.1B) in agreement with previous results. In Figure 5.1A we see the spatial distribution of confirmed cluster members (Luhman 2008) targeted by the Gaia-ESO large spectroscopic survey, which show a clear separation into two clumps of stars in the northern and southern part of the cluster<sup>2</sup>. Both subclusters show similar velocity dispersions of  $0.9 \pm 0.3$  and  $1.0 \pm 0.3 \text{ km s}^{-1}$  (Figure 5.1C and 5.1D) and only have a difference in the mean velocity of  $0.7 \pm 0.4 \text{ km s}^{-1}$ . These low velocity dispersions suggest that Chamaeleon I is bound by the molecular gas mass of  $3600 M_{\odot}$  still present within the cluster (Mizuno et al. 1998). The full results for this cluster will be discussed in detail by Sacco et al. (in prep).

---

<sup>1</sup>Low-mass stars (around  $0.5 - 1 M_{\odot}$ ) dominate the mass of a cluster due to their sheer abundance, the light emitted by young stellar groups is still dominated by the few much more massive stars.

<sup>2</sup>This separation is also seen in the complete population of confirmed members (e.g. Luhman 2008)

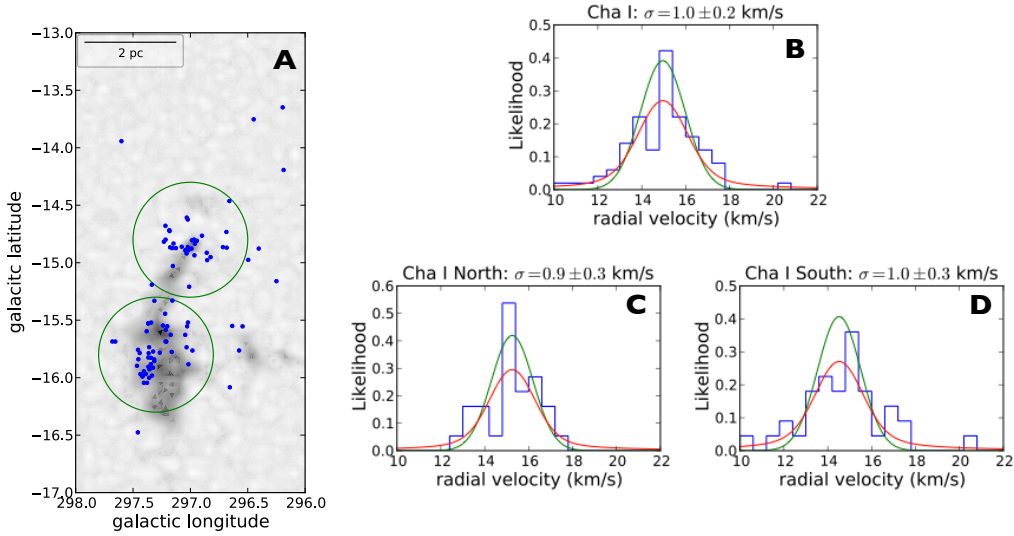


Fig. 5.1 — Radial velocity distribution for stars in star-forming region Chamaeleon I, which were already confirmed as members in the Luhman (2008) catalogue. A: Spatial distribution of spectroscopically observed cluster members (blue) with in the background an extinction map from Dobashi (2011). The stellar group is split into two clumps (North and South), whose extent is approximated by the green circles. B: Observed radial velocity distribution (blue) with best-fit Gaussian velocity distribution including the effects of binary orbital motions (red) and excluding the effects of binary orbital motions (green). C and D: The same as panel B, but only for the Northern and Southern clump of stars respectively. See Sacco et al. (in prep) for a detailed analysis of this dataset.

Another young stellar group, for which the Gaia-ESO high-resolution spectra have already been reduced is Gamma 2 Velorum, which is an overdensity of stars surrounding the massive star  $\gamma^2$  Vel in the Vela OB2 association (Jeffries et al. 2009). Figure 5.2AB shows the radial velocity distribution of a nearly complete sample of young stars with  $V < 19$  around the massive star  $\gamma^2$  Vel, where the young stars have been identified based on their equivalent width of the Lithium spectral line (Jeffries et al. 2014). The radial velocity distribution is fitted much better by two Gaussians, than a single one, suggesting that there are two dynamically distinct populations. One population has a very broad velocity distribution and is probably related to the Vela OB2 associations, while the other has a narrower velocity distribution, consistent with being a bound cluster (Jeffries et al. 2014).

Large radial velocity datasets were also collected by Fűrész et al. (2008) and Tobin et al. (2009) in Orion and by Fűrész et al. (2006) in NGC 2264. Tobin et al. (2009) found that the velocity dispersion in Orion varies between 1 and 3 km s<sup>-1</sup> with a higher dispersion in regions with more gas. Fűrész et al. (2006) found very non-Gaussian velocity distribution in NGC 2264 with a dispersion of about 3.5 km s<sup>-1</sup>. Both of these stellar groups are still embedded within their molecular cloud, making a conclusion about their dynamical state more difficult, because it depends on the spatial correlation between the stars and the gas. These surveys used high-resolution spectra in the visible, so they are biased towards the

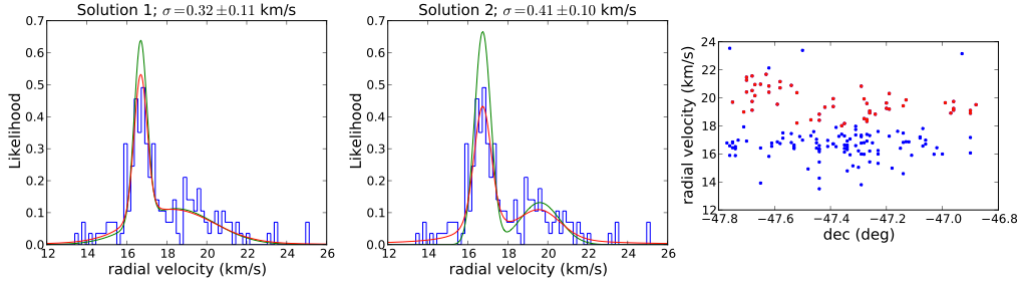


Fig. 5.2 — Radial velocity distribution and best-fit for Gamma 2 Velorum. The young stars in the direction of Gamma 2 Velorum show a bimodal velocity distribution (blue histogram in left two panels). The solution space also shows a bimodality with the fits of the two local maxima shown in the first two panels (red: with binary orbital motions; green: without binary orbital motions). The right panel shows the radial velocities versus the declination. The high-probability members to the population with the broad velocity dispersion are shown in red. These have a velocity gradient, which can be interpreted as shearing, if solution 2 (central panel) is correct. A detailed analysis of the Gamma 2 Velorum dataset is provided by Jeffries et al. (2014).

surface population. Combined with the radial velocities from the near-infrared APOGEE spectograph (chapter 4), it should be possible to study the dynamical evolution of these young embedded clusters in detail.

A final conclusion for the boundedness of the low-mass clusters is more difficult to reach as for the high-mass cluster, as Chamaeleon I, Orion, and NGC 2264 are still embedded in large amounts of molecular gas, whose gravity binds the stars. Gamma 2 Velorum and IC 348 do appear to be bound, although the former is so low-mass that it will likely dissipate due to two-body relaxation on a short timescale.

The analyses presented in this thesis might give the impression that most stars emerge bound. This is clearly not the case, as only 10% of stars formed in embedded clusters are still found to be bound after 10 Myr (Lada & Lada 2003). In this thesis we focused on the high-density, young stellar groups, showing them to be bound. However, plenty of young stars are not in such high-density cluster, but in low-density associations, which are unbound. These low-density associations could either have formed in that state or could be the result of high-density clusters that become unbound. The lack of unbound dense stellar groups suggest that the former is a more likely scenario. This was confirmed at least for the association Cygnus OB2 by Wright et al. (2014), who showed that this association showed plenty of substructure in the positions and proper motions (i.e. close stars had similar motions), which suggests that the cluster formed in this way and has not passed through a dense state, which would have wiped out this substructure.

## 5.4 Outlook

The study by Wright et al. (2014) of Cygnus OB2 provides an excellent preview of the type of science that will become possible in the near future due to the launch of the Gaia satellite (<http://sci.esa.int/gaia/>). This satellite was recently (December 19) successfully launched by the European Space Agency (ESA) and has reached its destination at L2 on January 8. Over the next decade it will scan the complete night sky, mapping to high precision the brightness, positions, and proper motions of about 1 billion stars. Many of these stars will belong to known associations or dense stellar groups, allowing their dynamical state to be characterized in great detail. For the brighter and closest stars Gaia will also provide both radial velocities and parallax distances, providing for the first time six-dimensional phase-space information for the closest stellar groups. The unbiased mapping of the whole sky should also allow many new low-density stellar groups (especially moving groups) to be found. This will provide a huge census of the dynamical states of stellar groups in the solar neighbourhood, allowing for example the origins of many associations to be studied in detail by looking for locally correlated velocities and whether the stars can be traced back to a single, dense state (Wright et al. 2014). This science will be further enhanced by the binary systems and variable, young stars that Gaia will be able to detect.

However, Gaia is limited to the visible and so will be mostly sensitive to stellar groups, that have already emerged from their natal molecular cloud. For deeply embedded clusters Gaia will only be able to observe the surface population. Still many questions about star cluster formation and evolution require knowledge of stars at these very young ages. For example, the pre-main sequence stars discussed in chapter 4 and section 5.3 typically show velocity dispersions of about  $1 \text{ km s}^{-1}$ , much larger than the core-to-core velocity dispersion observed for prestellar cores (André et al. 2007; Kirk et al. 2007). This increase in kinetic energy could either come from global collapse, which can only take place if the initial free-fall time is short enough (corresponding to a high enough mass density) to allow the stars to collapse before gas expulsion is capable of removing the gas potential. Alternatively the kinetic energy could come from the evaporation of the initial stellar clumps (Smith et al. 2011b), which could be powered by the decay of unstable, multiple systems formed within a single pre-main sequence core. This would lead to the stars being more spread out throughout the molecular cloud, increasing the effect of gas expulsion, which may lead to an unbound association. This suggests that bound clusters might only form if both the global density is high enough to allow free-fall collapse before the gas is removed (as expected in richer clusters) and the local density is low enough to prevent the velocity dispersion to be pumped up by stellar scattering. These early stages could be probed by near-infrared spectrographs, such as APOGEE from the Sloan Digital Sky Survey (see chapter 4). Covey et al. (2006) attempted to constrain the velocity differences between the gas and extremely young ( $\sim 0.5 \text{ Myr}$ ) class I protostars in several star-forming regions. Unfortunately their upper bound on the velocity dispersion of  $2.5 \text{ km s}^{-1}$  (which I confirmed using a fit including binary orbital motions) was insufficient to determine, whether the stellar velocity dispersion had significantly increased over the first  $\sim 0.5 \text{ Myr}$  of an embedded cluster's lifetime. Alternatively more about the initial state of the stars could be obtained by instruments like ALMA, whose high resolution might suffice to determine

until which spatial scale fragmentation continues. Its high sensitivity is also crucial in characterizing the progenitor molecular clouds of young massive cluster like Westerlund I in other galaxies (e.g. Longmore et al. 2014).





# Bibliography

- Allard, F., Homeier, D., & Freytag, B. 2011, in *Astronomical Society of the Pacific Conference Series*, Vol. 448, 16th Cambridge Workshop on Cool Stars, Stellar Systems, and the Sun, ed. C. Johns-Krull, M. K. Browning, & A. A. West, 91
- Allende Prieto, C. 2007, *AJ*, 134, 1843
- Allison, R. J., Goodwin, S. P., Parker, R. J., Portegies Zwart, S. F., & de Grijs, R. 2010, *MNRAS*, 407, 1098
- Alves, J., Lombardi, M., & Lada, C. J. 2007, *A&A*, 462, L17
- Alves, J. F., Lada, C. J., & Lada, E. A. 2001, *Nature*, 409, 159
- Andersen, M., Zinnecker, H., Moneti, A., et al. 2009, *ApJ*, 707, 1347
- André, P., Belloche, A., Motte, F., & Peretto, N. 2007, *A&A*, 472, 519
- André, P., Di Francesco, J., Ward-Thompson, D., et al. 2013, *ArXiv e-prints*
- André, P., Men'shchikov, A., Bontemps, S., et al. 2010, *A&A*, 518, L102
- Applegate, J. H. 1986, *ApJ*, 301, 132
- Arzoumanian, D., André, P., Didelon, P., et al. 2011, *A&A*, 529, L6
- Arzoumanian, D., André, P., Peretto, N., & Könyves, V. 2013, *A&A*, 553, A119
- Baraffe, I., Vorobyov, E., & Chabrier, G. 2012, *ApJ*, 756, 118
- Bastian, N., Covey, K. R., & Meyer, M. R. 2010, *ARA&A*, 48, 339
- Bastian, N., Saglia, R. P., Goudfrooij, P., et al. 2006, *A&A*, 448, 881
- Bate, M. R., Bonnell, I. A., & Bromm, V. 2003, *MNRAS*, 339, 577

## BIBLIOGRAPHY

---

- Baumgardt, H., Grebel, E. K., & Kroupa, P. 2005, *MNRAS*, 359, L1
- Baumgardt, H. & Kroupa, P. 2007, *MNRAS*, 380, 1589
- Baumgardt, H. & Makino, J. 2003, *MNRAS*, 340, 227
- Bell, C. P. M., Naylor, T., Mayne, N. J., Jeffries, R. D., & Littlefair, S. P. 2012, *MNRAS*, 424, 3178
- Bell, C. P. M., Naylor, T., Mayne, N. J., Jeffries, R. D., & Littlefair, S. P. 2013, *MNRAS*
- Bernstein, R., Sheckman, S. A., Gunnels, S. M., Mochnecki, S., & Athey, A. E. 2003, in Presented at the Society of Photo-Optical Instrumentation Engineers (SPIE) Conference, Vol. 4841, Society of Photo-Optical Instrumentation Engineers (SPIE) Conference Series, ed. M. Iye & A. F. M. Moorwood, 1694–1704
- Binney, J. & Tremaine, S. 2008, *Galactic Dynamics: Second Edition* (Princeton University Press)
- Blake, C. H., Charbonneau, D., & White, R. J. 2010, *ApJ*, 723, 684
- Blake, C. H., Charbonneau, D., White, R. J., Marley, M. S., & Saumon, D. 2007, *ApJ*, 666, 1198
- Blecha, A., Meylan, G., North, P., & Royer, F. 2004, *A&A*, 419, 533
- Bonatto, C., Bica, E., & Santos, Jr., J. F. C. 2005, *A&A*, 433, 917
- Bonnell, I. A. & Bate, M. R. 2006, *MNRAS*, 370, 488
- Bonnell, I. A., Smith, R. J., Clark, P. C., & Bate, M. R. 2011, *MNRAS*, 410, 2339
- Bosch, G., Terlevich, E., & Terlevich, R. 2009, in *IAU Symposium*, Vol. 256, IAU Symposium, ed. J. T. van Loon & J. M. Oliveira, 317–322
- Brandner, W., Clark, J. S., Stolte, A., et al. 2008, *A&A*, 478, 137
- Breddels, M. A. & Helmi, A. 2013, *ArXiv e-prints*
- Breger, M. 1986, *ApJ*, 309, 311
- Breger, M. 1987, *ApJ*, 319, 754
- Burgasser, A. J., Reid, I. N., Siegler, N., et al. 2007, *Protostars and Planets V*, 427
- Caffau, E., Ludwig, H.-G., Steffen, M., Freytag, B., & Bonifacio, P. 2011, *Sol. Phys.*, 268, 255
- Cambrésy, L., Petropoulou, V., Kontizas, M., & Kontizas, E. 2006, *A&A*, 445, 999
- Cartwright, A. & Whitworth, A. P. 2004, *MNRAS*, 348, 589
- Cartwright, A. & Whitworth, A. P. 2009, *MNRAS*, 392, 341

- Chabrier, G. 2003, *PASP*, 115, 763
- Chabrier, G. 2005, in *Astrophysics and Space Science Library*, Vol. 327, *The Initial Mass Function 50 Years Later*, ed. E. Corbelli, F. Palla, & H. Zinnecker, 41
- Chen, H.-C. & Ko, C.-M. 2009, *ApJ*, 698, 1659
- Chini, R., Hoffmeister, V. H., Nasserri, A., Stahl, O., & Zinnecker, H. 2012, *MNRAS*, 424, 1925
- Clark, J. S., Negueruela, I., Crowther, P. A., & Goodwin, S. P. 2005, *A&A*, 434, 949
- Clark, J. S., Ritchie, B. W., & Negueruela, I. 2010, *A&A*, 514, A87+
- Clark, J. S., Ritchie, B. W., Negueruela, I., et al. 2011, *A&A*, 531, A28+
- Clarkson, W. I., Ghez, A. M., Morris, M. R., et al. 2012, *ApJ*, 751, 132
- Converse, J. M. & Stahler, S. W. 2011, *MNRAS*, 410, 2787
- Cottaar, M. & Hénauld-Brunet, V. 2014, *A&A*, 562, A20
- Cottaar, M., Meyer, M. R., Andersen, M., & Espinoza, P. 2012a, *A&A*, 539, A5
- Cottaar, M., Meyer, M. R., & Parker, R. J. 2012b, *A&A*, 547, A35
- Covey, K. R., Greene, T. P., Doppmann, G. W., & Lada, C. J. 2006, *AJ*, 131, 512
- Crapsi, A., Caselli, P., Walmsley, M. C., & Tafalla, M. 2007, *A&A*, 470, 221
- Crowther, P. A., Hadfield, L. J., Clark, J. S., Negueruela, I., & Vacca, W. D. 2006, *MNRAS*, 372, 1407
- Crowther, P. A., Schnurr, O., Hirschi, R., et al. 2010, *MNRAS*, 408, 731
- Crutcher, R. M. 2012, *ARA&A*, 50, 29
- Crutcher, R. M., Wandelt, B., Heiles, C., Falgarone, E., & Troland, T. H. 2010, *ApJ*, 725, 466
- Da Rio, N. & Robberto, M. 2012, *AJ*, 144, 176
- Da Rio, N., Robberto, M., Hillenbrand, L. A., Henning, T., & Stassun, K. G. 2012, *ApJ*, 748, 14
- Dale, J. E., Ercolano, B., & Bonnell, I. A. 2012, *MNRAS*, 424, 377
- Dale, J. E., Ercolano, B., & Bonnell, I. A. 2013, *MNRAS*, 430, 234
- Davies, B., de La Fuente, D., Najarro, F., et al. 2012, *MNRAS*, 419, 1860
- Davis, D. S., Richer, H. B., Anderson, J., et al. 2008, *AJ*, 135, 2155
- de Jager, C. 1998, *A&A Rev.*, 8, 145

## BIBLIOGRAPHY

---

- de Koter, A., Heap, S. R., & Hubeny, I. 1998, *ApJ*, 509, 879
- Dobashi, K. 2011, *PASJ*, 63, 1
- Dobbs, C. L., Burkert, A., & Pringle, J. E. 2011, *MNRAS*, 413, 2935
- Dobbs, C. L., Krumholz, M. R., Ballesteros-Paredes, J., et al. 2013, *ArXiv e-prints*
- Dotter, A., Chaboyer, B., Jevremović, D., et al. 2008, *ApJS*, 178, 89
- Dubath, P., Reipurth, B., & Mayor, M. 1996, *A&A*, 308, 107
- Duchêne, G. & Kraus, A. 2013, *ARA&A*, 51, 269
- Dunham, M. M., Stutz, A. M., Allen, L. E., et al. 2014, *ArXiv e-prints*
- Dunham, M. M. & Vorobyov, E. I. 2012, *ApJ*, 747, 52
- Eisenstein, D. J., Weinberg, D. H., Agol, E., et al. 2011, *AJ*, 142, 72
- Eldridge, J. J., Izzard, R. G., & Tout, C. A. 2008, *MNRAS*, 384, 1109
- Elmegreen, B. G. 1983, *MNRAS*, 203, 1011
- Elson, R. A. W., Fall, S. M., & Freeman, K. C. 1987, *ApJ*, 323, 54
- Enoch, M. L., Evans, II, N. J., Sargent, A. I., & Glenn, J. 2009, *ApJ*, 692, 973
- Evans, C. J., Taylor, W. D., Hénault-Brunet, V., et al. 2011, *A&A*, 530, A108
- Evans, II, N. J., Dunham, M. M., Jørgensen, J. K., et al. 2009, *ApJS*, 181, 321
- Feiden, G. A. & Chaboyer, B. 2012, *ApJ*, 757, 42
- Fűrész, G., Hartmann, L. W., Megeath, S. T., Szentgyorgyi, A. H., & Hamden, E. T. 2008, *ApJ*, 676, 1109
- Fűrész, G., Hartmann, L. W., Szentgyorgyi, A. H., et al. 2006, *ApJ*, 648, 1090
- Fleck, J., Boily, C. M., Lançon, A., & Deiters, S. 2006, *MNRAS*, 369, 1392
- Foreman-Mackey, D., Hogg, D. W., Lang, D., & Goodman, J. 2013, *PASP*, 125, 306
- Garmany, C. D., Conti, P. S., & Massey, P. 1980, *ApJ*, 242, 1063
- Geller, A. M. & Mathieu, R. D. 2011, *Nature*, 478, 356
- Geller, A. M., Mathieu, R. D., Braden, E. K., et al. 2010, *AJ*, 139, 1383
- Geller, A. M., Mathieu, R. D., Harris, H. C., & McClure, R. D. 2008, *AJ*, 135, 2264
- Geller, A. M., Mathieu, R. D., Harris, H. C., & McClure, R. D. 2009, *AJ*, 137, 3743
- Gennaro, M., Brandner, W., Stolte, A., & Henning, T. 2011, *MNRAS*, 412, 2469

- Gieles, M., Baumgardt, H., Heggie, D. C., & Lamers, H. J. G. L. M. 2010a, MNRAS, 408, L16
- Gieles, M., Heggie, D. C., & Zhao, H. 2011, MNRAS, 413, 2509
- Gieles, M. & Portegies Zwart, S. F. 2011, MNRAS, 410, L6
- Gieles, M., Portegies Zwart, S. F., Baumgardt, H., et al. 2006, MNRAS, 371, 793
- Gieles, M., Sana, H., & Portegies Zwart, S. F. 2010b, MNRAS, 402, 1750
- Gilmore, G., Randich, S., Asplund, M., et al. 2012, The Messenger, 147, 25
- Goodman, J. & Weare, J. 2010, Communications in Applied Mathematics and Computational Science, 5, 65
- Goodwin, S. P. 2009, Ap&SS, 324, 259
- Goodwin, S. P. 2010, Royal Society of London Philosophical Transactions Series A, 368, 851
- Goodwin, S. P. & Bastian, N. 2006, MNRAS, 373, 752
- Goodwin, S. P. & Whitworth, A. P. 2004, A&A, 413, 929
- Gray, D. F. 1992, The observation and analysis of stellar photospheres.
- Gunn, J. E. & Griffin, R. F. 1979, AJ, 84, 752
- Hanson, M. M., Kudritzki, R.-P., Kenworthy, M. A., Puls, J., & Tokunaga, A. T. 2005, ApJS, 161, 154
- Hartmann, L. 2001, AJ, 121, 1030
- Heggie, D. C. 2001, in Astronomical Society of the Pacific Conference Series, Vol. 228, Dynamics of Star Clusters and the Milky Way, ed. S. Deiters, B. Fuchs, A. Just, R. Spurzem, & R. Wielen, 29
- Heggie, D. C., Trenti, M., & Hut, P. 2006, MNRAS, 368, 677
- Hénault-Brunet, V., Evans, C. J., Sana, H., et al. 2012a, A&A, 546, A73
- Hénault-Brunet, V., Gieles, M., Evans, C. J., et al. 2012b, A&A, 545, L1
- Herbst, W. 2008, Star Formation in IC 348, ed. B. Reipurth, in Handbook of Star Forming Regions, Volume I: The Northern Sky (ASP), 372
- Heyer, M. H. & Brunt, C. M. 2004, ApJ, 615, L45
- Heyl, J. 2008, MNRAS, 390, 622
- Hillenbrand, L. A. 1997, AJ, 113, 1733
- Hillenbrand, L. A. & White, R. J. 2004, ApJ, 604, 741

## BIBLIOGRAPHY

---

- Hills, J. G. 1975, *AJ*, 80, 809
- Hills, J. G. 1980, *ApJ*, 235, 986
- Holtzman, J. A., Faber, S. M., Shaya, E. J., et al. 1992, *AJ*, 103, 691
- Hsu, W.-H., Hartmann, L., Allen, L., et al. 2012, *ApJ*, 752, 59
- Husser, T.-O., Wende-von Berg, S., Dreizler, S., et al. 2013, *A&A*, 553, A6
- Indulekha, K. 2013, *Journal of Astrophysics and Astronomy*, 34, 207
- Inutsuka, S.-I. & Miyama, S. M. 1997, *ApJ*, 480, 681
- Janson, M., Hormuth, F., Bergfors, C., et al. 2012, *ApJ*, 754, 44
- Jeffries, R. D., Jackson, R. J., Cottaar, M., et al. 2014, *A&A*, 563, A94
- Jeffries, R. D., Naylor, T., Walter, F. M., Pozzo, M. P., & Devey, C. R. 2009, *MNRAS*, 393, 538
- Joergens, V. 2006, *A&A*, 448, 655
- Joergens, V. & Guenther, E. 2001, *A&A*, 379, L9
- Jørgensen, J. K., Harvey, P. M., Evans, II, N. J., et al. 2006, *ApJ*, 645, 1246
- Kim, E., Einsel, C., Lee, H. M., Spurzem, R., & Lee, M. G. 2002, *MNRAS*, 334, 310
- Kiminki, D. C. & Kobulnicky, H. A. 2012, *ApJ*, 751, 4
- King, I. R. 1965, *AJ*, 70, 376
- King, R. R., Goodwin, S. P., Parker, R. J., & Patience, J. 2012a, *MNRAS*, 427, 2636
- King, R. R., Parker, R. J., Patience, J., & Goodwin, S. P. 2012b, *MNRAS*, 2421
- Kirk, H., Johnstone, D., & Tafalla, M. 2007, *ApJ*, 668, 1042
- Klassen, M., Pudritz, R. E., & Peters, T. 2012, *MNRAS*, 2443
- Kleyna, J., Wilkinson, M. I., Evans, N. W., Gilmore, G., & Frayn, C. 2002, *MNRAS*, 330, 792
- Kobulnicky, H. A. & Fryer, C. L. 2007, *ApJ*, 670, 747
- Kothes, R. & Dougherty, S. M. 2007, *A&A*, 468, 993
- Kouwenhoven, M. B. N. & de Grijs, R. 2008, *A&A*, 480, 103
- Kouwenhoven, M. B. N. & de Grijs, R. 2009, *Ap&SS*, 324, 171
- Kroshko, D. 2007, *OpenOpt: Free scientific-engineering software for mathematical modeling and optimization*

- Kroupa, P. 2001, MNRAS, 322, 231
- Kruijssen, J. M. D., Maschberger, T., Moeckel, N., et al. 2012, MNRAS, 419, 841
- Krumholz, M. R. & Thompson, T. A. 2012, ApJ, 760, 155
- Lada, C. J. 2006, ApJ, 640, L63
- Lada, C. J. & Lada, E. A. 2003, ARA&A, 41, 57
- Lada, C. J., Margulis, M., & Dearborn, D. 1984, ApJ, 285, 141
- Lamers, H. J. G. L. M., Baumgardt, H., & Gieles, M. 2013, MNRAS, 433, 1378
- Lamers, H. J. G. L. M., Gieles, M., Bastian, N., et al. 2005, A&A, 441, 117
- Larson, R. B. 1969, MNRAS, 145, 271
- Larson, R. B. 1981, MNRAS, 194, 809
- Larson, R. B. 2005, MNRAS, 359, 211
- Leisawitz, D., Bash, F. N., & Thaddeus, P. 1989, ApJS, 70, 731
- Lobel, A., Israelian, G., de Jager, C., et al. 1998, A&A, 330, 659
- Longmore, S. N., Kruijssen, J. M. D., Bastian, N., et al. 2014, ArXiv e-prints
- Lopez, L. A., Krumholz, M. R., Bolatto, A. D., Prochaska, J. X., & Ramirez-Ruiz, E. 2011, ApJ, 731, 91
- Lopez Martí, B., Jimenez Esteban, F., Bayo, A., et al. 2013, A&A, 551, A46
- Luhman, K. L. 1999, ApJ, 525, 466
- Luhman, K. L. 2008, Chamaeleon, ed. B. Reipurth, Handbook of Star Forming Regions, Volume II (ASP), 169
- Luhman, K. L., Lada, C. J., Hartmann, L., et al. 2005, ApJ, 631, L69
- Luhman, K. L., Rieke, G. H., Lada, C. J., & Lada, E. A. 1998, ApJ, 508, 347
- Luhman, K. L., Stauffer, J. R., Muench, A. A., et al. 2003, ApJ, 593, 1093
- Lynden-Bell, D. 1967, MNRAS, 136, 101
- Lynden-Bell, D. & Eggleton, P. P. 1980, MNRAS, 191, 483
- Mackey, A. D. & Gilmore, G. F. 2003, MNRAS, 338, 85
- Maíz-Apellániz, J. 2001, ApJ, 563, 151
- Mann, A. W., Gaidos, E., & Ansdell, M. 2013, ApJ, 779, 188
- Marigo, P., Girardi, L., Bressan, A., et al. 2008, A&A, 482, 883



## BIBLIOGRAPHY

---

- Marks, M., Kroupa, P., & Oh, S. 2011, *MNRAS*, 417, 1684
- Martinez, G. D., Minor, Q. E., Bullock, J., et al. 2011, *ApJ*, 738, 55
- Maschberger, T. 2013, *MNRAS*, 429, 1725
- Mason, B. D., Hartkopf, W. I., Gies, D. R., Henry, T. J., & Helsel, J. W. 2009, *AJ*, 137, 3358
- Masunaga, H. & Inutsuka, S.-i. 2000, *ApJ*, 531, 350
- Masunaga, H., Miyama, S. M., & Inutsuka, S.-I. 1998, *ApJ*, 495, 346
- Mathieu, R. D. 1983, *ApJ*, 267, L97
- McConnachie, A. W. & Côté, P. 2010, *ApJ*, 722, L209
- McLaughlin, D. E. & van der Marel, R. P. 2005, *ApJS*, 161, 304
- McMillan, S., Vesperini, E., & Portegies Zwart, S. 2008, in *IAU Symposium*, Vol. 246, IAU Symposium, ed. E. Vesperini, M. Giersz, & A. Sills, 41–45
- Mengel, S., Lehnert, M. D., Thatte, N., & Genzel, R. 2002, *A&A*, 383, 137
- Mengel, S. & Tacconi-Garman, L. E. 2007, *A&A*, 466, 151
- Mengel, S. & Tacconi-Garman, L. E. 2009, *Ap&SS*, 324, 321
- Men'shchikov, A., André, P., Didelon, P., et al. 2010, *A&A*, 518, L103
- Mermilliod, J.-C., Mayor, M., & Udry, S. 2009, *A&A*, 498, 949
- Michie, R. W. & Bodenheimer, P. H. 1963, *MNRAS*, 126, 269
- Mizuno, A., Hayakawa, T., Yamaguchi, N., et al. 1998, *ApJ*, 507, L83
- Moeckel, N. & Bate, M. R. 2010, *MNRAS*, 404, 721
- Moeckel, N., Holland, C., Clarke, C. J., & Bonnell, I. A. 2012, *MNRAS*, 425, 450
- Morales-Calderón, M., Stauffer, J. R., Stassun, K. G., et al. 2012, *ApJ*, 753, 149
- Muench, A. A., Lada, C. J., Luhman, K. L., Muzerolle, J., & Young, E. 2007, *AJ*, 134, 411
- Muench, A. A., Lada, E. A., Lada, C. J., et al. 2003, *AJ*, 125, 2029
- Myers, A., Klein, R., Krumholz, M., & McKee, C. 2014, *ArXiv e-prints*
- Negueruela, I., Clark, J. S., & Ritchie, B. W. 2010, *A&A*, 516, A78+
- Odenkirchen, M., Grebel, E. K., Dehnen, W., Rix, H.-W., & Cudworth, K. M. 2002, *AJ*, 124, 1497
- Offner, S. S. R., Klein, R. I., McKee, C. F., & Krumholz, M. R. 2009, *ApJ*, 703, 131

- Ostriker, E. C. 1999, *ApJ*, 513, 252
- Parker, R. J. & Goodwin, S. P. 2009, *MNRAS*, 397, 1041
- Parker, R. J. & Goodwin, S. P. 2012, *MNRAS*, 424, 272
- Parker, R. J., Maschberger, T., & Alves de Oliveira, C. 2012, *MNRAS*, 426, 3079
- Parker, R. J. & Quanz, S. P. 2011, *MNRAS*, 1760
- Parker, R. J. & Reggiani, M. M. 2013, *MNRAS*, 432, 2378
- Parker, R. J., Wright, N. J., Goodwin, S. P., & Meyer, M. R. 2014, *MNRAS*, 438, 620
- Pelupessy, F. I. & Portegies Zwart, S. 2012, *MNRAS*, 420, 1503
- Peters, T., Klessen, R. S., Mac Low, M.-M., & Banerjee, R. 2010, *ApJ*, 725, 134
- Pineda, J. E., Goodman, A. A., Arce, H. G., et al. 2010, *ApJ*, 712, L116
- Platais, I., Kozhurina-Platais, V., Mathieu, R. D., Girard, T. M., & van Altena, W. F. 2003, *AJ*, 126, 2922
- Polychroni, D., Schisano, E., Elia, D., et al. 2013, *ApJ*, 777, L33
- Portegies Zwart, S. F., McMillan, S. L. W., & Gieles, M. 2010, *ARA&A*, 48, 431
- Prato, L. 2007, *ApJ*, 657, 338
- Preibisch, T., Stanke, T., & Zinnecker, H. 2003, *A&A*, 409, 147
- Preibisch, T. & Zinnecker, H. 2001, *AJ*, 122, 866
- Price, D. J. & Bate, M. R. 2009, *MNRAS*, 398, 33
- Proszkow, E.-M., Adams, F. C., Hartmann, L. W., & Tobin, J. J. 2009, *ApJ*, 697, 1020
- Pryor, C. & Meylan, G. 1993, in *Astronomical Society of the Pacific Conference Series*, Vol. 50, *Structure and Dynamics of Globular Clusters*, ed. S. G. Djorgovski & G. Meylan, 357
- Raghavan, D., McAlister, H. A., Henry, T. J., et al. 2010, *ApJS*, 190, 1
- Rebull, L. M., Stapelfeldt, K. R., Evans, II, N. J., et al. 2007, *ApJS*, 171, 447
- Reggiani, M. & Meyer, M. R. 2013, *A&A*, 553, A124
- Reggiani, M., Robberto, M., Da Rio, N., et al. 2011, *A&A*, 534, A83
- Reggiani, M. M. & Meyer, M. R. 2011, *ApJ*, 738, 60
- Reipurth, B. & Clarke, C. 2001, *AJ*, 122, 432
- Rieke, G. H. & Lebofsky, M. J. 1985, *ApJ*, 288, 618

## BIBLIOGRAPHY

---

- Ripepi, V., Molinaro, R., Marconi, M., et al. 2014, *MNRAS*, 437, 906
- Ritchie, B. W., Clark, J. S., Negueruela, I., & Crowther, P. A. 2009a, *A&A*, 507, 1585
- Ritchie, B. W., Clark, J. S., Negueruela, I., & Langer, N. 2010, *A&A*, 520, A48+
- Ritchie, B. W., Clark, J. S., Negueruela, I., & Najarro, F. 2009b, *A&A*, 507, 1597
- Robin, A. C., Reyl e, C., Derri ere, S., & Picaud, S. 2003, *A&A*, 409, 523
- Rochau, B., Brandner, W., Stolte, A., et al. 2010, *ApJ*, 716, L90
- Sabbi, E., Lennon, D. J., Gieles, M., et al. 2012, *ApJ*, 754, L37
- Sana, H., de Koter, A., de Mink, S. E., et al. 2013, *A&A*, 550, A107
- Sana, H., de Mink, S. E., de Koter, A., et al. 2012, *Science*, 337, 444
- Sana, H. & Evans, C. J. 2011, in *IAU Symposium*, Vol. 272, *IAU Symposium*, ed. C. Neiner, G. Wade, G. Meynet, & G. Peters, 474–485
- Sana, H., James, G., & Gosset, E. 2011, *MNRAS*, 416, 817
- Sarajedini, A., von Hippel, T., Kozhurina-Platais, V., & Demarque, P. 1999, *AJ*, 118, 2894
- Schmeja, S., Kumar, M. S. N., & Ferreira, B. 2008, *MNRAS*, 389, 1209
- Scholz, R.-D., Brunzendorf, J., Ivanov, G., et al. 1999, *A&AS*, 137, 305
- Smith, R., Fellhauer, M., Goodwin, S., & Assmann, P. 2011a, *MNRAS*, 414, 3036
- Smith, R., Slater, R., Fellhauer, M., Goodwin, S., & Assmann, P. 2011b, *MNRAS*, 416, 383
- Soderblom, D. R., Laskar, T., Valenti, J. A., Stauffer, J. R., & Rebull, L. M. 2009, *AJ*, 138, 1292
- Soderblom, D. R., Stauffer, J. R., Hudon, J. D., & Jones, B. F. 1993, *ApJS*, 85, 315
- Sollima, A., Nipoti, C., Mastrobuono Battisti, A., Montuori, M., & Capuzzo-Dolcetta, R. 2012, *ApJ*, 744, 196
- Stap, F. A., Sana, H., & de Koter, A. 2011, *Journal of Physics Conference Series*, 328, 012025
- Sterzik, M. F. & Durisen, R. H. 1995, *A&A*, 304, L9
- Sterzik, M. F. & Durisen, R. H. 2003, *A&A*, 400, 1031
- Sylos Labini, F. 2012, *MNRAS*, 423, 1610
- Teixeira, P. S., Lada, C. J., Young, E. T., et al. 2006, *ApJ*, 636, L45
- Terrien, R. C., Mahadevan, S., Deshpande, R., et al. 2014, *ApJ*, 782, 61

- Tobin, J. J., Hartmann, L., Furesz, G., Mateo, M., & Megeath, S. T. 2009, *ApJ*, 697, 1103
- Torres, G., Ruíz-Rodríguez, D., Badenas, M., et al. 2013, *ApJ*, 773, 40
- Trenti, M., Ardi, E., Mineshige, S., & Hut, P. 2007, *MNRAS*, 374, 857
- Trenti, M. & van der Marel, R. 2013, *MNRAS*, 435, 3272
- Tutukov, A. V. 1978, *A&A*, 70, 57
- Udry, S., Mayor, M., Maurice, E., et al. 1999, in *Astronomical Society of the Pacific Conference Series, Vol. 185, IAU Colloq. 170: Precise Stellar Radial Velocities*, ed. J. B. Hearnshaw & C. D. Scarfe, 383
- Umbreit, S., Burkert, A., Henning, T., Mikkola, S., & Spurzem, R. 2005, *ApJ*, 623, 940
- van de Ven, G., van den Bosch, R. C. E., Verolme, E. K., & de Zeeuw, P. T. 2006, *A&A*, 445, 513
- van Kempen, T. A., van Dishoeck, E. F., Salter, D. M., et al. 2009, *A&A*, 498, 167
- von Hippel, T. & Sarajedini, A. 1998, *AJ*, 116, 1789
- Watkins, L. L., van de Ven, G., den Brok, M., & van den Bosch, R. C. E. 2013, *MNRAS*, 436, 2598
- Westerlund, B. E. 1987, *A&AS*, 70, 311
- Wright, N. J., Parker, R. J., Goodwin, S. P., & Drake, J. J. 2014, *MNRAS*, 438, 639
- Zinnecker, H. & Yorke, H. W. 2007, *ARA&A*, 45, 481

## BIBLIOGRAPHY

---

# Curriculum vitæ

## Contact information

Michiel Cottaar  
Departement Physik  
Institut für Astronomie  
ETH Zürich, HIT J41.1  
Wolfgang-Pauli-Str. 27  
CH-8093 Zürich  
Schweiz/Switzerland

*Phone:* +41 (0)44 633 7520  
*E-mail:* [mcottaar@phys.ethz.ch](mailto:mcottaar@phys.ethz.ch)  
*Web:* [www.astro.ethz.ch/people/mcottaar](http://www.astro.ethz.ch/people/mcottaar)

## Personal information

*Date of Birth:* January 14th, 1987  
*Place of Birth:* Uden, the Netherlands  
*Citizenship:* Dutch  
*Languages:* Fluent in Dutch and English, conversational in German

## Experience

Ph.D. candidate, ETH Zürich 2010-2014  
*Title:* Dynamical evolution of young stellar clusters  
*Advisor:* Prof. Dr. Michael R. Meyer

Internship, University of Oslo 2009-2010  
*Topic:* Tracking of spicules in the solar atmosphere  
*Advisor:* Mats Carlsson

MSc in astrophysics, Utrecht University 2007-2009  
*Title:* A Model of Coronal Streamers with Underlying Flux Ropes  
*Advisor:* Prof. Dr. Christoph U. Keller & Dr. Yuhong Fan  
*Award:* Best master thesis of the Utrecht University (2009/2010)

BSc in physics, Utrecht University 2004-2007

## Teaching experience

*Astrophysics I:* taught exercise classes Autumn 2010  
*Astrophysics I:* taught exercise classes Autumn 2011  
*Advanced practicum:* supervised experiment “Harmonic analysis” Spring 2011  
*Astrophysics I:* taught exercise classes Autumn 2012  
*Advanced practicum:* supervised experiment “Harmonic analysis” Spring 2012  
*Advanced practicum:* supervised experiment “Harmonic analysis” Autumn 2013